

MICROFLUIDIC INVESTIGATION OF TRACER DYE DIFFUSION
IN ALUMINA NANOFUIDS

A Dissertation

by

SERDAR OZTURK

Submitted to the Office of Graduate Studies of
Texas A&M University
in partial fulfillment of the requirements for the degree of

DOCTOR OF PHILOSOPHY

Approved by:

Chair of Committee,	Victor M. Ugaz
Committee Members,	Yassin A. Hassan
	Mahmoud El-Halwagi
	Yue Kuo
Head of Department,	M. Nazmul Karim

December 2012

Major Subject: Chemical Engineering

Copyright 2012 Serdar Ozturk

ABSTRACT

Nanofluids, a new class of fluids engineered by suspending nanometer-sized particles in a host liquid, are offered as a new strategy in order to improve heat and mass transfer efficiency. My research was motivated by previous exciting studies on enhanced mass diffusion and the possibility of tailoring mass transport by direct manipulation of molecular diffusion. Therefore, a microfluidic approach capable of directly probing tracer diffusion between nanoparticle-laden fluid streams was developed. Under conditions matching previously reported studies, strong complexation interactions between the dye and nanoparticles at the interface between fluid streams was observed. When the tracer dye and surfactant were carefully chosen to minimize the collective effects of the interactions, no significant change in tracer dye diffusivity was observed in the presence of nanoparticles.

Next, adapting tracer dyes for studies involving colloidal nanomaterials was explored. Addition of these charged tracers poses a myriad of challenges because of their propensity to disrupt the delicate balance among physicochemical interactions governing suspension stability. Here it was shown how important it is to select the compatible combinations of dye, nanoparticle, and stabilizing surfactant to overcome these limitations in low volume fraction (< 1 vol%) aqueous suspensions of Al_2O_3 nanoparticles. A microfluidic system was applied as a stability probe that unexpectedly revealed how rapid aggregation could be readily triggered in the presence of local

chemical gradients. Suspension stability was also assessed in conjunction with coordinated measurements of zeta potential, steady shear viscosity and bulk thermal conductivity.

These studies also guided our efforts to prepare new refrigerant formulations containing dispersed nanomaterials, including graphene nanosheets, carbon nanotubes and metal oxide and nitride. The influence of key parameters such as particle type, size and volume fraction on the suspension's thermal conductivity was investigated using a standard protocol. Our findings showed that thermal conductivity values of carbon nanotube and graphene nanosheet suspensions were higher than TiO₂ nanoparticles, despite some nanoparticles with large particle sizes provided noticeable thermal conductivity enhancements. Significantly, the graphene containing suspensions uniquely matched the thermal conductivity enhancements attained in nanotube suspensions without accompanying viscosity, thus making them an attractive new coolant for demanding applications such as electronics and reactor cooling.

DEDICATION

To my beloved wife, Hulya;
my parents, and
my sisters and their families

ACKNOWLEDGEMENTS

I would like to thank and express my deep gratitude to Dr. Victor M. Ugaz for giving me an opportunity to work in this project and also for his invaluable supervision, guidance and enthusiasm rendered at all stages of my research. I am also grateful to my advisory committee members, Dr. Yassin A. Hassan, Dr. Mahmoud El-Halwagi, and Dr. Yue Kuo for their time and recommendations.

Thanks also go to my friends and colleagues for making my time at Texas A&M University a great experience. I also want to extend my gratitude to State of Texas Norman Hackerman Advanced Research Program for providing funding to this research.

I would like to express my sincere sense of gratitude to the department faculty and staff, particularly to Dr. Mahmoud El-Halwagi for his advice, encouragement, and support. Special thanks also go to my past and present group members and colleagues; Jen Huang, Faisal, Yu-Wen and Inho for their discussions, friendship and help.

Finally, it is a pleasure to thank my family and my friends for their help, appreciations, and understandings throughout this study. I also would like to express my deepest gratitude and love to my spouse, Hulya for her patience, sacrifice, unflagging optimism, and support.

NOMENCLATURE

DI	Deionized
SDS	Sodium dodecyl sulphate
THW	Transient hot wire
MWCNT	Multi wall carbon nanotube
GNS	Graphene nanosheet
HFE	Hydrofluoroether
Φ	Volume fraction
ρ	Density
μ	Viscosity
k	Thermal conductivity (W/m K)
D_{th}	Thermal diffusivity (m^2/s)
D	Mass diffusivity (m^2/s)
Nu	Nusselt number
wt%	Weight percentage
vol%	Volume percentage
t_{agg}	Aggregation timescale
t_{res}	Residence time in the microchannel
TEM	Transmission electron microscopy
SEM	Scanning electron microscopy

TABLE OF CONTENTS

	Page
ABSTRACT	ii
DEDICATION	iv
ACKNOWLEDGEMENTS	v
NOMENCLATURE.....	vi
TABLE OF CONTENTS	vii
LIST OF FIGURES.....	x
LIST OF TABLES	xx
1. INTRODUCTION.....	1
2. RESEARCH REVIEW	7
2.1 Introduction	7
2.2 Investigation of Mass Transfer in Nanofluids.....	9
2.3 Heat Transfer Studies in Nanofluids	15
2.4 Rheological Behaviour of Nanofluids.....	24
2.5 Nanorefrigerants.....	28
3. EXPERIMENTAL METHODS	30
3.1 Introduction	30
3.2 Nanofluids Preparation and Characterization	30
3.3 Microdevice Design and Assembly.....	46
3.4 Flow Visualization and Data Analysis	53
3.5 Thermal Conductivity Measurements	56
3.6 Viscosity Measurements	61
4. INTERFACIAL COMPLEXATION EXPLAINS ANOMALOUS DIFFUSION IN NANOFLLUIDS.....	62
4.1 Introduction	62

	Page
4.2 Microfluidic Approach.....	63
4.3 Fluorescein Diffusion in Alumina Nanoparticle Suspensions	66
4.4 Evaluation of Alternative Dye/Surfactant Combination	73
4.5 Experimental Pitfalls and Challenges Need to Be Avoided.....	78
5. A SIMPLE MICROFLUIDIC PROBE OF NANOPARTICLE SUSPENSION STABILITY.....	80
5.1 Introduction	80
5.2 Microfluidic Stability Probe.....	81
5.3 Bulk Stability Characterization	86
5.4 Final Remarks	94
6. GRAPHENE-ENHANCED NANOREFRIGERANTS	100
6.1 Introduction	100
6.2 Colloidal Stability of Nanorefrigerant.....	102
6.3 Measurements of Thermal Conductivity in Nanorefrigerants.....	106
6.4 Rheological Characteristics of MWCNT and GNS Suspensions.....	110
6.5 Final Remarks	116
7. PHYSICAL AND THERMAL CHARACTERIZATION OF COMMERCIAL REFRIGERANTS WITH NANOFILLERS.....	120
7.1 Introduction	120
7.2 Surfactant-mediated Particle Dispersion Approach	121
7.3 Nanoparticle Effects on Thermal Conductivity of Refrigerant.....	124
7.4 Rheological Behavior of Refrigerant Based Nanoparticle Suspensions	137
7.5 Final Remarks	142
8. CONCLUSIONS AND FUTURE WORK	143
8.1 Conclusions	143
8.2 Future Work	146
REFERENCES.....	150
APPENDIX A	163
APPENDIX B	165
APPENDIX C	171
APPENDIX D	176

	Page
APPENDIX E.....	178
APPENDIX F	183

LIST OF FIGURES

	Page
Figure 1. Mass diffusion enhancement in a Al ₂ O ₃ nanofluid. ³¹ “Reprinted with the permission from Krishnamurthy, S.; Bhattacharya, P.; Phelan, P. E.; Prasher, R. S. Nano Letters 2006, 6, (3), 419-423. Copyright 2006 American Chemical Society.”	9
Figure 2. Temperature effect on diffusion coefficient of rhodamine B in low volume fractions of Cu nanofluids. ³⁴ “Reprinted with the permission from Fang, X.; Xuan, Y.; Li, Q. Appl Phys Lett 2009, 95, (20), 203108. Copyright 2009 American Institute of Physics.”	10
Figure 3. The ratio of measured diffusion coefficients of rhodamine 6G in alumina suspensions (D_{nf}) to the one measured in water (D_w) as a function of volume fraction. ³⁵ The data plotted is the average of five experiments and the error bars indicate the one standard deviation taken on them “Reprinted with the permission from Veilleux, J.; Coulombe, S. J Appl Phys 2010, 108, (10), 104316. Copyright 2010 American Institute of Physics.”	12
Figure 4. Comparison of experimental results of the thermal conductivity enhancement with nanofluids. ²⁶ “Reprinted from Applied Thermal Engineering, 28, (17-18), Murshed, S.; Leong, K.; Yang, C., Thermophysical and electrokinetic properties of nanofluids-A critical review, 2109-2125, 2008, with the permission from Elsevier.”	16
Figure 5. Heat transfer coefficient versus Reynolds number. ²⁸ “Reprinted with the permission from Pak and Cho, 1998”	22
Figure 6. Improvement on heat transfer coefficient of nucleate pool boiling due to the presence of alumina nanoparticles. ²⁹ “Reprinted from Journal of Nanoparticle Research, 7, (2), 2005, 265-274, Experimental investigation into the pool boiling heat transfer of aqueous based - alumina nanofluids, Wen, D., Ding, Y., Figure 7, with kind permission from Springer Science and Business Media.”	23
Figure 7. Viscosity of TiO ₂ nanofluids as a function of shear rate. ³⁰ “Reprinted with the permission from Wen and Ding, © 2006 IEEE.”	25

	Page
Figure 8. Photographs of the used devices. (a) The digital stirring hot plate (Model Cimarec SP131325; Barnstead Thermolyne Corp., Dubuque, IA), (b) The ultrasonic cleaner (Model 3510DTH; Branson Ultrasonics Corp., Danbury, CT), (c) A probe sonicator (Vibracell VCX 750; Sonics & Materials Inc., Newtown, CT).....	32
Figure 9. Photographs of suspensions (a) Al ₂ O ₃ (1 vol%, Nanoamor Inc.), Tween 80, H ₂ O, (b) Al ₂ O ₃ (1 vol%, Nanoamor Inc.), SDS, H ₂ O, (c) The suspension prepared from Al ₂ O ₃ (1 vol%, NEI Inc.), H ₂ O is still stable after more than 1 week in the stationary state without sedimentation.	35
Figure 10. TEM photographs of evaporatively dried aqueous alumina suspension (bars, 100 and 20 nm).	38
Figure 11. Physical properties of HFE 7500 (3M™ Novec™ 7500 Engineered Fluid). (a) Thermal conductivity versus temperature. (b) Kinematic viscosity versus temperature. ¹¹² “Reprinted with the permission from 3M Electronics Markets Materials, 2010.”	41
Figure 12. Schematic view of Y shaped PDMS channel production from a rigid mold or master.	47
Figure 13. (a) PDMS microfluidic channel produced by using soft lithography. The length of the horizontal channel is 27 mm and its cross sectional dimensions are 500×50 μm. (b) Syringe pump and polyethylene tubings connected to the channel.	48
Figure 14. Gel formation from SEBS.....	49
Figure 15. Fabrication of masters using printed circuit technology.....	51
Figure 16. The finalizing steps in production of thermoplastic elastomer channel.....	52
Figure 17. Top view imaging using Zeiss LSM 5 Pascal confocal microscope.....	53
Figure 18. KD2 Pro thermal property analyzer (Decagon Devices, Inc., Pullman, WA).....	56

- Figure 19. A standardized thermal conductivity measurement protocol for nanorefrigerants. The apparatus employs commercially available components to create a standard platform that can be easily assembled in any laboratory. Shown are (1) KD2-Pro thermal conductivity meter, (2) glass jar with septum in cap, (3) circulating water bath, (4) support stand, (5) clamps, (6) nanofluid sample, (7) KS-1 probe needle, and (8) bath temperature controller. Drawing is not to scale..... 60
- Figure 20. Microfluidic approach for measuring tracer diffusion in nanoparticle suspensions. Parallel fluid streams are introduced into a microchannel under laminar flow conditions. Lateral diffusion of the tracer dye in stream I is characterized by recording the growth of the fluorescence intensity profile width ($w_i \approx \sigma_i$) from the centerline (CL) into stream II. Measurements acquired along the microchannel midplane (i.e., halfway between the floor and ceiling) at multiple downstream locations from the inlet (x_i) are then converted to units of time, yielding a linear increase in w^2 whose slope is proportional to the diffusion coefficient. 64
- Figure 21. In the approach used by KBPP,³¹ a drop of tracer dye is introduced into a quiescent pool (4 mm dia., 2 mm tall) containing a nanoparticle suspension. The radial spreading of dye fluorescence (r_i) is recorded by acquiring images at multiple points in time (t_i), yielding a linear increase in $\langle(\Delta r)^2\rangle$ whose slope is proportional to the diffusion coefficient..... 65
- Figure 22. The KBPP experiment conditions are mimicked by introducing co-flowing streams consisting of an aqueous fluorescein solution (stream I) and an aqueous Al_2O_3 nanoparticle suspension (stream II) into a microchannel at a flow rate of 0.05 ml/min. Fluorescence images are shown at the inlet and locations 12 and 24 mm downstream (scale bar 250 μm). Complexation between the dye and nanoparticles becomes vividly evident by formation of an intensely fluorescent plume at the interface between streams, accompanied by a depletion region of reduced fluorescence in the immediately adjacent dye. The fluorescent plume becomes prominent with increasing alumina concentration to 1 vol%. All nanoparticle suspensions contained 5.35 mg/ml Tween-80 (tracer dye solutions contained no surfactant). 67

	Page
Figure 23. The fluorescent plume becomes more prominent with decreasing flow rate, corresponding to increasing fluid residence time within the microchannel (0.5 vol% Al ₂ O ₃ , all other experiment conditions identical to Figure 22). All nanoparticle suspensions contained 5.35 mg/ml Tween-80 (tracer dye solutions contained no surfactant).....	68
Figure 24. (a) The fluorescent plumes disappear when identical fluid compositions are used in streams I and II with the only exception being addition of the tracer dye in stream I. But lateral spreading of fluorescence becomes inhibited when surfactant and nanoparticles are added. The composition of each stream is given above and below each image, and the symbols correspond to those plotted in the graph (0.5 wt% Al ₂ O ₃ , 0.05 ml/min flow rate, images acquired 24 mm downstream from the inlet). (b) The inhibited lateral transport causes significant deviation from the expected linear increase in the square of the fluorescent zone width as a function of time, making it impossible to extract meaningful measurements of the tracer dye diffusivity in the presence of surfactant and nanoparticles. Diffusion coefficients measured in the dye solution alone (filled blue squares, dashed line shows linear regression fit to these data) agree with literature values and are not affected by addition of methanol. All nanoparticle suspensions contained 5.35 mg/ml Tween-80. A fluorescein concentration of 0.33 mg/ml was used in all experiments shown, microchannel sidewalls are highlighted by a white line.	69
Figure 25. Phenytoin diffusion immunoassay (DIA). The image on the top is a bright field one with antibody specific for phenytoin in the left side flow stream and a 10 % blood solution spiked labeled antigen and treated with iophenoxate in the right side flow stream. Corresponding fluorescence image at the same location was also shown. ¹³⁷ “Reprinted with the permission from Macmillian Publishers Ltd: Nature Biotechnology, Hatch, A.; Kamholz, A.; Hawkins, K.; Munson, M.; Schilling, E.; Weigl, B.; Yager, P., 19, (5), 461-465, Copyright 2001.” ...	71
Figure 26. Interfacial fluorescent plumes arise as a consequence of complexation between the tracer dye and suspended nanoparticles. Under conditions analogous to those employed in the KBPP experiments (Figures 22 and 23) dye-nanoparticle complexes are formed more rapidly than the rate of lateral dye diffusion, resulting in formation of an interfacial fluorescent plume accompanied by an adjacent depletion zone of reduced fluorescence.....	72

- Figure 27. Fluorescein diffusion images taken at multiple points in time in (a) pure water and (b) 0.5 vol % alumina nanofluid. You can see Figure 2 and 3 in reference 31 for all images taken.³¹ “Reprinted with the permission from Krishnamurthy, S.; Bhattacharya, P.; Phelan, P. E.; Prasher, R. S. Nano Letters 2006, 6, (3), 419-423. Copyright 2006 American Chemical Society.” 73
- Figure 28. When nanoparticles are present in both streams, dye diffusion is inhibited at low concentrations where there are an excess of nanoparticle adsorption sites (left). Increasing the tracer dye concentration to a level exceeding that of the available adsorption sites allows lateral diffusion to progress (and be measured) even in the presence of complexation interactions (right)..... 74
- Figure 29. Tracer diffusion measurements obtained under conditions designed to account for dye-nanoparticle interactions. (a) Fluorescence images obtained using a combination of an anionic surfactant (SDS) and anionic dye (Rose Bengal) selected to enable higher dye concentrations to be used while minimizing dye-surfactant interactions (the composition of both streams is identical, except that stream I contains dye). Lateral spreading of the tracer dye is evident beyond the interfacial zone (0.5 wt% Al₂O₃, 0.05 ml/min flow rate, scale bar 250 μm, microchannel sidewalls are highlighted by a white line). (b) The observed lateral spreading follows a trend whereby the square of the zone width increases linearly with time, enabling diffusion coefficients to be quantified (dashed line shows linear regression fit to Rose Bengal data (filled blue squares)). No appreciable change in diffusivity values is observed with addition of surfactant or nanoparticles. 75
- Figure 30. The effects of dye-nanoparticle interactions become evident when lateral spreading is measured as a function of dye concentration in a 0.5 wt% Al₂O₃ suspension (other conditions identical to Figure 29). The increase in the square of the fluorescent zone width deviates from the initially linear increasing trend at all, but the highest dye concentration (dashed line shows linear regression fit to 5 mg/ml data (filled blue squares)). 77

- Figure 31. Exploiting interfacial destabilization in a microchannel to assess nanoparticle suspension stability. (a) Localized aggregation can occur when co-flowing streams containing an aqueous tracer solution (Stream I) and a SDS-stabilized alumina suspension (Stream II) are simultaneously injected into a microchannel, depositing zones of dense nanoparticle agglomerates along the interface between them. The aggregation patterns display morphologies ranging from well-defined lines to unstable globules beyond a downstream distance x^* . (b) Pronounced interfacial aggregation occurs in the case of rhodamine 6G, despite the fact that the suspension appears highly stable in bulk (see Figure 34). Interfacial aggregation does not occur in the case of Rose Bengal under comparable conditions. A 1 vol% alumina suspension is shown. Rhodamine 6G and Rose Bengal concentrations were 0.5 and 5 mg/ml, respectively; the SDS concentration was 15 mg/ml, the flow rate was 0.05 ml/min. Scale bars, 500 μm 82
- Figure 32. (a) SEM image showing line of nanoparticle aggregates deposited on the microchannel floor at the interface between co-flowing streams. (b) EDX analysis of the aggregation zone. The highest peak corresponds to Al. 83
- Figure 33. The position and morphology of interfacial aggregation is tunable by adjusting the suspension composition and flow rate. (a) Effect of rhodamine 6G concentration (1 vol% alumina, 15 mg/ml SDS, 0.05 ml/min). (b) Effect of surfactant concentration (1 vol% alumina, 0.5 mg/ml rhodamine 6G, 0.05 ml/min). (c) Effect of nanoparticle concentration under conditions where a stable interfacial aggregation zone is produced (120 mg/ml SDS, 0.5 mg/ml rhodamine 6G, 0.05 ml/min). (d) Effect of flow rate (0.5 mg/ml rhodamine 6G). (e) Aggregation data from (d) display a similar trend when plotted in terms of a characteristic timescale associated with the onset of an unstable aggregation pattern t_{agg} normalized by the residence time t_{res} as a function of surfactant concentration and flow rate, where the SDS concentrations in the 15 – 30 mg/ml range represent conditions where x^* could be reproducibly measured (dashed line indicates linear regression fit). Scale bars, 500 μm 85

- Figure 34. Tracer-laden suspensions appear highly stable in bulk despite being readily susceptible to aggregation in the microchannel-based test. (a) Aqueous 1 vol% Al_2O_3 suspensions containing no added tracer or surfactant are highly stable against sedimentation. Adding a tracer destabilizes the suspensions, but the effect is counteracted by the surfactant SDS. (b) Rhodamine 6G (0.5 mg/ml). (c) Rose Bengal (5 mg/ml). The SDS concentration in (b) and (c) was 15 mg/ml. 89
- Figure 35. Steady shear viscosity measurements also indicate no strong signatures of bulk aggregation. Measurements were obtained over a shear rate sweep from 500 to 10 s^{-1} after first ramping up from 10 to 500 s^{-1} to generate a reproducible initial condition. Data are plotted in terms of the suspension viscosity relative to that of water (μ/μ_0). (a) In the absence of tracer, viscosity enhancement at low shear rates is observed, suggesting complexation between the nanoparticles and surfactant. (b) A somewhat sharper enhancement in low shear rate viscosity is evident upon addition of rhodamine 6G. (c) Viscosity values more closely mirror the dye-free data in (a) for suspensions containing Rose Bengal. The SDS concentration was 15 mg/ml in all cases. Rhodamine 6G and Rose Bengal concentrations were 0.5 and 5 mg/ml, respectively. 92
- Figure 36. Thermal conductivity measurements also indicate high bulk stability. The SDS concentration was 15 mg/ml in both tracer laden suspensions. Rhodamine 6G and Rose Bengal concentrations were 0.5 and 5 mg/ml, respectively. Data are expressed relative to the particle-free case (k/k_0), and plotted with error bars representing the mean \pm s.d. of 3 independent measurements. 93
- Figure 37. Photographs showing results of a titration experiment whereby a 7 mL aliquot of aqueous rhodamine 6G (0.5 mg/ml) solution was added to 7 mL of a series of 1 vol% Al_2O_3 suspensions with increasing SDS concentration. In all cases, sedimentation at the bottom of the container became evident within a few minutes after adding the tracer. ... 97
- Figure 38. Surfactant-mediated stabilization of nanomaterials in a fluorinated refrigerant host liquid. Compatible chemical groups are presented to the surrounding fluid upon adsorption to (a) TiO_2 nanoparticles, as well as bundles containing (b) carbon nanotubes and (c) graphene nanosheets. Insets show TEM images of nanomaterials employed in our studies (scale bars are 50 nm, 400 nm, and 500 nm in (a), (b), and (c), respectively). 105

- Figure 39. MWCNT-based nanorefrigerants display enhanced thermal conductivity. (a) Thermal conductivity measurements of suspensions containing MWCNTs obtained from two different commercial vendors indicate a ~15% enhancement at a loading of 1 vol % at 12°C (Sample 1: Cheap Tubes, Inc.; Sample 2: Helix Material Solutions, Inc.). (b) Temperature dependence of thermal conductivity in refrigerant suspensions containing MWCNTs (Sample 2: Cheap Tubes, Inc.) Data are expressed relative to the particle-free case k/k_0 . All refrigerant solutions contained 1 vol% Krytox 157 FSL. 108
- Figure 40. Graphene-based nanorefrigerants display enhanced thermal conductivity. Thermal conductivity measurements of suspensions containing GNSs obtained from two different commercial vendors (Sample 1: Skyspring Nanomaterials, Inc.; Sample 2: Cheap Tubes, Inc.; data are expressed relative to the pure refrigerant (particle- and surfactant-free) k/k_0) at 12°C. All refrigerant solutions contained 1 vol% Krytox 157 FSL. 109
- Figure 41. Minimal thermal conductivity enhancements are observed in nanoparticle-based refrigerant suspensions. Thermal conductivity measurements of dispersions containing TiO₂ nanoparticles display little change from those of the particle-free host refrigerant. Data are expressed relative to the pure refrigerant (particle- and surfactant-free) k/k_0 , all measurements were performed at 12 °C. 110
- Figure 42. (a) Steady shear viscosity measurements show a dramatic increase at low shear rates (results are plotted relative to the pure refrigerant (particle- and surfactant-free) η/η_0 ; Table 5). All the experiments were carried out at a constant temperature of 12°C. (b) Temperature dependence of steady shear viscosity in a 1 vol% MWCNT dispersion. Data shown are for nanotubes obtained from Cheap Tubes, Inc. and expressed relative to the pure refrigerant (particle- and surfactant-free) (η/η_0) over a shear rate sweep from 500 to 10 s⁻¹ after first ramping up from 10 to 500 s⁻¹ to generate a reproducible initial condition. All refrigerant solutions contained 1 vol% Krytox 157 FSL. 112
- Figure 43. Only a minimal increase in steady shear viscosity is observed (data shown are for Sample 2 obtained over a shear rate sweep from 500 to 10 s⁻¹ after first ramping up from 10 to 500 s⁻¹ to generate a reproducible initial condition, results are plotted relative to the pure refrigerant (particle- and surfactant-free) η/η_0 ; Table 5). All measurements were performed at 12 °C. 113

- Figure 44. Nanosuspension viscosity and long term stability at GNS loadings above 1 vol%. (a) Steady shear viscosity continues to increase at higher GNS loadings, but the enhancements are much more modest than in MWCNT dispersions (experiment conditions are identical to those in Figure 43). (b) Photographs showing GNS suspension stability as a function of particle loading after 7 days of incubation at room temperature. Loadings of 1 vol% and below (left) display excellent long term stability while significant sedimentation occurs at higher concentrations (arrows), becoming evident after as little as 48 h. Materials were obtained from Cheap Tubes, Inc. 115
- Figure 45. Chemical structures of (a) HFE 7500, (b) Krytox 157 FSL (n~14-17), (c) Stabilization process of nanoparticles. 121
- Figure 46. Concentration dependence of thermal conductivity enhancements in refrigerant suspensions containing various nanoparticles (data are expressed relative to the pure refrigerant (particle- and surfactant-free) k/k_0). The Krytox 157 FSL concentration was 1 vol % in all refrigerant suspensions. 125
- Figure 47. (a) TEM image and the corresponding electron diffraction pattern of Al_2O_3 nanoparticles used to formulate the suspensions. (b) Temperature dependence of thermal conductivity enhancements in refrigerant suspensions containing Al_2O_3 nanoparticles (data are expressed relative to the particle-free case k/k_0). (c) Steady shear viscosity measurements show a little increase at low shear rates (data shown are obtained over a shear rate sweep from 500 to 10 s^{-1} after first ramping up from 10 to 500 s^{-1} to generate a reproducible initial condition, results are plotted relative to the particle-free case (η/η_0). Experiments were carried out at constant temperatures (2°C, 12°C and 22°C). All refrigerant solutions contained 1 vol% Krytox 157 FSL. 127
- Figure 48. (a) TEM image and the corresponding electron diffraction pattern of dry AlN nanoparticles. (b) Small change in thermal conductivity enhancements at high temperatures. (c) Steady shear viscosity measurements of refrigerant suspensions containing AlN nanoparticles (data are expressed relative to the particle-free case, (η/η_0)). The experiment conditions are the same as that in Al_2O_3 measurements. 128

- Figure 49. (a) TEM image and the corresponding electron diffraction pattern of dry ZnO nanoparticles. (b) Thermal conductivity of suspensions only show appreciable enhancement at high temperatures. (c) The similar viscosity enhancement trend is observed in steady shear measurements. The experiment conditions are the same as that in Al₂O₃ measurements. 129
- Figure 50. (a) TEM image and the corresponding electron diffraction pattern of dry CuO nanoparticle. (b) Thermal conductivity enhancements in CuO refrigerant suspensions are low as well. (c) The increase in steady shear viscosity measurements at low shear rates is still observed. The experiment conditions are the same as that in Al₂O₃ measurements. 130
- Figure 51. (a) TEM image and the corresponding electron diffraction pattern of dry TiO₂ nanoparticles. (b) The refrigerant suspensions of TiO₂ displayed less than 5% enhancements in thermal conductivity. (c) The remarkable viscosity increase in steady shear viscosity is easily noticed again at low shear rates. The experiment conditions are the same as that in Al₂O₃ measurements. 131

LIST OF TABLES

		Page
Table 1.	Specifications of tested nanofluid.	33
Table 2.	The tracer dye structure and concentrations.	36
Table 3.	Summary of materials used in nanorefrigerant preparation.	43
Table 4.	Typical physical properties of HFE 7500 used in DLS and zeta potential measurements.	45
Table 5.	Bulk characterization of Al ₂ O ₃ nanoparticle suspensions (complete datasets are provided in APPENDIX B).	87
Table 6.	Effect of added surfactant on refrigerant steady-shear viscosity. Data are shown as a function of shear rate (averaged over an ensemble of 5-10 experiments at each temperature), and as an average over all shear rates at each temperature.	103
Table 7.	Effect of added surfactant on refrigerant thermal conductivity. Data shown are average values over the entire ensemble of experiments reported (see main text for details).	107
Table 8.	Summary of thermal characterization studies involving refrigerant-based nanofluids.	118
Table 9.	Bulk characterization of nanoparticle suspensions (complete datasets are provided in APPENDIX D).	123
Table 10.	Summary of thermal characterization studies involving nanoparticles.	133
Table 11.	Theoretical models used for predicting thermal conductivity of nanorefrigerants.	136
Table 12.	Summary of rheological studies involving nanoparticle suspensions.	139
Table 13.	Theoretical models used for predicting viscosity variation.	141

1. INTRODUCTION

Novel properties of colloidal nanomaterials have led them to become more prominent in a variety of areas such as ceramics, drug delivery systems, inks, paints, coatings, cosmetics, foods and even heat transfer applications.¹⁻⁵ An innovative approach has been needed in order to enhance heat transfer to meet the cooling challenge in the systems instead of using conventional ways (increase surface area or flow velocity) with limited capacity. Poor thermal characteristics that greatly limit the heat exchange efficiency of traditional heat transfer fluids in comparison to solid materials has led researchers to expect an increase in thermal conductivities of fluids with particle addition. However, suspensions prepared from micro or millimeter size particles suffered from many drawbacks (sedimentation, fouling and clogging in systems, high pressure drop etc.).⁶⁻⁸ In order to minimize these problems, the suspensions prepared from the particles at nano size (nanofluids) were first suggested as an alternative fluid by Choi and coworkers in Argonne National Laboratory.⁹ Nanofluids can be defined as a special class of colloidal suspensions containing ultrafine (10-100 nm) metal or nonmetallic nanoparticles (Al_2O_3 , TiO_2 , CuO) in a base fluid at low volume fractions (< 5 vol%).

Nanofluids have been observed to have great potential in improving heat transport performance compared to conventional heat transfer fluids, which is a prominent factor making them compelling candidates in thermal management

applications.¹⁰⁻¹² For example, effective thermal conductivity of ethylene glycol increased by up to 26% with dispersion of 5 vol% alumina¹³ and 40% with the 0.3 vol % copper nanoparticles.¹⁰ Utilizing unique properties of nanoparticles, these fluids have been being proposed in many exciting studies for different applications including the heat spreader for CPU in a notebook, improving heat transfer performance of cooling engine oil in a real four wheel-drive transmission system, and even for oily soil remover.¹⁴⁻¹⁷

Numerous studies have since characterized the effects of particles (type, shape, size and volume fraction), and bulk fluid (composition, pH, temperature, stabilizing additives) on thermophysical properties of these fluids.¹⁸⁻²⁵ Experimental investigations related to nanofluids in literature mostly focus on thermal conductivity, convective and pool boiling heat transfer and rheological behavior. Thermal conductivity of nanoparticle laden fluids increased as a function of nanoparticle concentration.^{24, 26, 27} Pak and Cho reported that convective heat transfer coefficient under turbulent conditions increased with increasing volume concentration of Al₂O₃ and TiO₂ nanoparticles in the flowing medium of a circular tube.²⁸ In another study done by Wen and Ding with a cylindrical boiling vessel, alumina nanofluid enhanced the boiling heat transfer significantly (~40%).²⁹ On the other hand, the addition of small amounts of TiO₂ nanoparticles into water enhanced the viscosity and rheological behavior of fluid changed from Newtonian to Pseudoplastic (shear thinning) fluid.³⁰

Until the exciting study about dramatic improvement in mass diffusion (i.e., as described in the paper by Krishnamurthy, Bhattacharya, Phelan, and Prasher;³¹ hereafter

referred to as KBPP), most of the work in literature has focused on the surprising enhancement of thermal properties of nanofluids instead of probing their applicability on mass transfer practices. They reported a 14-fold increase in fluorescein diffusivity when the dye was dispersed in a 0.5 vol% aqueous alumina suspension. In their experiments, when an identical drop of the dye solution was placed into a nanoparticle suspension, its outward diffusion produced a much different irregularly shaped pattern characterized by intensely fluorescent, thread-like regions superimposed over a nebulous background cloud of much lower intensity (see Figures 2b and 3 in reference 31). They did not examine the interactions among the dye, surfactant and nanoparticle. Inherent imprecision in introducing a tracer dye into the quiescent nanoparticle suspension using the drop-based method can magnify the problems in determination of diffusion coefficient. It is well known, for example, that the process by which a droplet merges with a quiescent pool of fluid rapidly establishes a complex flow field distinguished by vortex rings along the drop perimeter (an effect that would be enhanced by the mismatch in surface tension imposed by surfactant present in the nanoparticle suspension but absent in the tracer dye droplet).^{32, 33} After the surprising diffusion enhancement reported by KBPP³¹, Fang et al.³⁴ reported that the diffusion coefficient of rhodamine B in 0.5 vol% Cu-water nanofluids was measured as $31.8 \times 10^{-6} \text{ cm}^2/\text{s}$, which was 10.71 times bigger than that in deionized water ($2.97 \times 10^{-6} \text{ cm}^2/\text{s}$) at 15°C. Veilleux and Coulombe studied the diffusion of rhodamine 6G in aqueous alumina suspensions up to 2 vol%.³⁵ The enhancement reached up to an order of magnitude at this concentration. In contrast to these findings, Samouhos et al. could not observe significant change in diffusion of

allura dye in water or in 0.5, 0.7 and 1 wt% alumina nanofluid in the experiments done with Taylor dispersion set-up.³⁶ Gerardi et al. also reported that the self diffusion coefficient of water molecules in the alumina nanofluid decreased as the nanoparticle concentration increased.³⁷

As it is seen from the previous results, existing studies about the effects of nanoparticles on mass transfer are not sufficient. In addition, definitive conclusions are not being drawn due to uncertainty in integrity of the applied methods and the mechanisms leading to this enhancement. Therefore, the understanding of mass transfer enhancement with nanofluids is an urgent need for practical applications of these fluids in related areas. In this study, mass transfer in nanofluids is investigated by directly probing tracer diffusion during flow through a microfluidic network.³⁸ The characteristic laminar flow field within the microchannel environment allows tracer dye diffusion to be precisely measured in a straightforward way by co-injecting two miscible fluid streams so that they flow side-by-side down its length.³⁹ Lateral species transport (i.e., by diffusion perpendicular to the flow direction) can then be characterized by examining the rate at which the zone of interfacial contact between the two fluids grows with distance downstream from the inlet. The KBPP experiment conditions are first mimicked, and the fluorescein diffusion in alumina nanofluids is examined. After observing the interactions among the suspension components, this issue is addressed by employing an alternative dye-surfactant combination in order to obtain accurate diffusivity measurements.

It is important to understand these effects because heat and mass transfer studies often involve introducing passive tracers into the fluid that enable the resulting flow field

to be visualized and quantitatively mapped.⁴⁰⁻⁴² Micron-sized seed particles serve as tracers in well-established methods such as particle image velocimetry (PIV)⁴³ and particle tracking velocimetry (PTV)⁴⁴, but the addition of secondary particles to a colloidal suspension makes it challenging to clearly isolate effects associated with the suspended nanomaterials from those due to the seeding. Tracer dyes offer a potential to overcome these limitations by serving as *in-situ* probes of velocity (e.g., molecular tagging velocimetry (MTV)) and temperature (by recording the temperature-dependent fluorescence intensity or decay).⁴⁵⁻⁴⁷ They have also proven instrumental in investigations of mass transfer associated with diffusion and mixing.^{38, 48-52} The particle-free nature of these small-molecule tracer dyes therefore makes them attractive candidates to study thermal and mass transport in nanofluids.^{31, 34, 35, 38} Unfortunately, adapting tracer dyes for these flow studies is generally not straightforward due to the interplay among physicochemical interactions between the dye and other components comprising the suspension. For example, dye-nanoparticle adsorption and complexation with stabilizing additives (e.g., surfactants) can easily disrupt colloidal suspensions because their metastable nature renders them extremely susceptible to aggregation and sedimentation in response to small compositional perturbations. Here, the critical need for an improved fundamental understanding of these interaction phenomena that can enable tracer dyes to be employed for flow studies involving colloidal nanomaterials is also addressed. An ensemble of tracer dye and surfactant combinations in low concentrations (< 1 vol%) of Al₂O₃ nanoparticle suspensions is systematically explored by applying complementary characterization methods. These studies reveal how key

parameters such as solubility and relative charge can be selected to yield suspensions whose bulk properties are unaltered by addition of the charged tracer. Moreover, a new microfluidic approach that enables these interactions to be locally probed in the presence of steep chemical gradients (e.g., mimicking experiments where dye is directly injected into a nanofluid sample) is presented, leading to a surprising find, which shows that even suspensions appearing stable in bulk can be readily disrupted.

Finally, guided by these new insights from mass transfer and stability probe studies, a surfactant-mediated dispersal method is introduced in order to attain stable nanorefrigerants. As mentioned previously, suspending nano-sized solid particles in the coolants can change transport properties, flow features and enhance thermal performance. Refrigerant based nanofluids are therefore highly in demand and can be a good alternative for improving the performance of cooling and refrigeration applications. To the best of our knowledge, there has been little research about thermal properties of these innovative “nano-refrigerants”.⁵³⁻⁵⁵ Hence the suspensions of graphene nanosheets (GNS), multi-wall carbon nanotubes (MWCNTs) and nanoparticles (TiO₂, Al₂O₃, ZnO, CuO, and AlN) are prepared with a commercial hydrofluoroether (HFE 7500) host refrigerant. Then the effect of parameters on the thermal conductivity of the refrigerant is examined by using a standard protocol during measurements, and their applicability in the alternative refrigerant systems is discussed by considering the viscosity variation.

2. RESEARCH REVIEW

2.1 Introduction

It is well known that thermal conductivity of liquids is much less than that of solids. For example, thermal conductivity of water is around 0.6 W/mK, but carbon nanotubes can exhibit thermal conductivities around ~2000-3000 W/mK.⁵⁶ Heat conduction in liquids occurs through the interactions between vibrating molecules in a temperature gradient but in solids with different excitations such as with free electrons in metals and with phonons in insulators and some semiconductors. Most materials with greater electrical conductivity also show greater thermal conductivity, which strongly depends on the chemical structure of material.

High performance cooling is strongly in demand for many industrial technologies. There have been numerous efforts to handle continual increase in heat dissipation, including redesigning heat exchange equipment. The limitation in thermal conductivity of typical heat transfer fluids also necessitates the development of energy efficient cooling fluids. The idea of using nanoparticle dispersions as a method for augmenting thermal conductivity was first postulated by Choi and coworkers in Argonne National Laboratory⁹ although some early tries with millimeter and micrometer sized particles had resulted in sedimentation and clogging. They prepared multiple types of metal and metal oxide nanoparticle suspensions from chosen base fluids and observed anomalous enhancements in thermal conductivity.^{10, 27 57}

Nanofluids are formed by dispersing ultrafine particles (average crystallite size below 100 nm) at low concentrations into heat transfer liquids. However, they are not simple solid suspensions in liquids. They need to be even, stable and durable. The most frequently used nanoparticle materials are oxides (Al_2O_3 , TiO_2 and CuO), nitride ceramics (AlN), metals (Cu , Au and Al) and carbon nanotubes (Multi-wall and Single-wall). Traditional heat transfer liquids such as water, ethylene glycol and oil have been used as base fluids by most researchers. Two techniques have been used to produce nanofluids: the single-step and the two-step method. The single-step method involves simultaneous nanoparticle (especially metals) synthesis and dispersal into base fluid such as Cu dispersion in ethylene glycol. On the other hand, more extensively applied two-step method starts with the production of particles by physical methods (inert gas condensation or mechanical grinding) or chemical methods (chemical vapor deposition, chemical precipitation, etc.) and proceeds with dispersion step by changing surface properties of particles (stabilizer addition, ultrasonic agitation or pH adjustment).⁹ Metal oxide such as Al_2O_3 nanofluids are prepared according to this recipe because they are easy to disperse due to their surface hydrophilicity and chemical stability.

Although nanofluid technology is a relatively new field, there is a fast growing trend in applications of these fluids. Transportation, electronics cooling, space, defense, biomedicine, and nuclear system cooling are primary areas of this research. In the past a few years, many experimental investigations revealed that nanofluids can offer many benefits such as improved stability⁵⁸, enhanced heat and mass transfer^{26, 31, 59}, reduced clogging and pumping power⁶⁰, redesigned and miniaturized heat transfer systems.

2.2 Investigation of Mass Transfer in Nanofluids

The Diffusion Based Studies

Studies related to the effects of nanofluids on mass transport only recently have been undertaken. Krishnamurthy et al. reported higher diffusivity values of fluorescein with nanofluid usage.³¹ In their experiments with a drop-based set-up, tracer dye diffusion was first observed in pure water and then in aqueous suspensions of alumina nanoparticles. The enhancement in dye diffusivity was up to 14-fold, which was interpreted as a result of the velocity disturbance field created by the motion of nanoparticles.

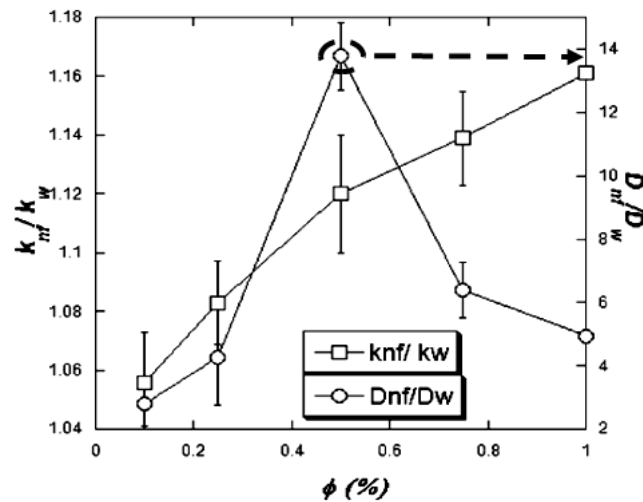


Figure 1. Mass diffusion enhancement in a Al_2O_3 nanofluid.³¹ “Reprinted with the permission from Krishnamurthy, S.; Bhattacharya, P.; Phelan, P. E.; Prasher, R. S. Nano Letters 2006, 6, (3), 419-423. Copyright 2006 American Chemical Society.”

There is a peak at a concentration of 0.5 vol% in diffusivity enhancement plot, showing more than an order of magnitude increase in diffusion coefficient of fluorescein

in alumina suspension with respect to pure water (Figure 1). Krishnamurthy et al. could not clearly explain the reason for this peak enhancement, but they proposed that a decrease in particle-to-particle separation due to increased particle concentration caused aggregation and inhibited convection motion in the colloidal system. The microscopy images with insufficient resolution and magnification also diminished the accuracy and reliability of the interpreted anomalous enhancement.

In another study, Fang et al.³⁴ also reported an anomalous increase in diffusion coefficient of rhodamine B in the presence of copper nanoparticles (Figure 2). This enhanced diffusion of tracer dye was attributed to microconvective heat and mass transfer induced by stochastic Brownian motion of suspended copper nanoparticles.

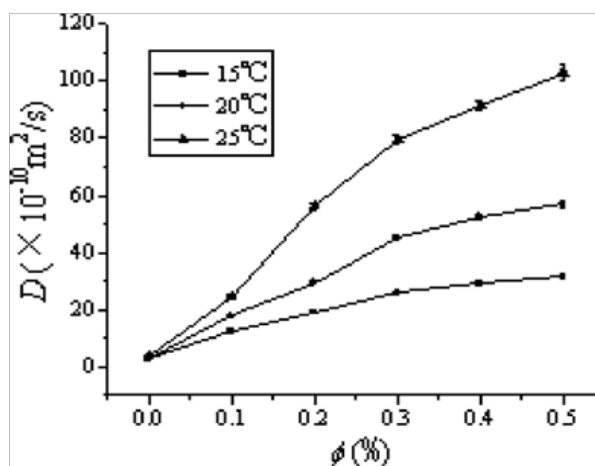


Figure 2. Temperature effect on diffusion coefficient of rhodamine B in low volume fractions of Cu nanofluids.³⁴ “Reprinted with the permission from Fang, X.; Xuan, Y.; Li, Q. Appl Phys Lett 2009, 95, (20), 203108. Copyright 2009 American Institute of Physics.”

Temperature appeared as an effective parameter on this enhancement. For example, diffusivity of rhodamine B became 26 times bigger than that in deionized

water when fluid temperature was raised from 15°C to 25°C. Due to obvious similarity in the experimental set up used by Krishnamurthy et al, the undesirable nanoparticle concentration gradient might have disturbed the dye diffusion process in the channel. Xuan also mentioned the analogy between heat and mass transfer processes in his theoretical work and proposed the micro motion and fluid disturbance due to irregular Brownian motion of suspended nanoparticles as main reasons for enhanced mass transfer in nanofluids.⁶¹

Although these exciting results showed that suspended nanoparticles augment mass diffusion enhancement, Samouhos et al. observed same binary diffusion coefficient of allura dye within 50%, with an average error of 20% or less for all measurements done with surfactants (SDS and Pluronic) and/or alumina nanoparticle added aqueous solutions in comparison to the diffusivity value ($4.2 \times 10^{-6} \text{ cm}^2/\text{s}$) found in water using Taylor dispersion set-up.³⁶ However they also reported fourfold increase in oxygenation rate with 0.01 wt% ferrofluid-carbon nanotube (FFCNT) composite and two fold increase with 0.5 vol% alumina and pointed out that mechanism leading to enhanced multi-phase transport depends on particle size (the critical particle dimension 50 nm or below) and number density. This work was then followed by many other studies including the works of Gerardi et al. and Turanov and Tolmachev. Gerardi and coworkers used nuclear magnetic resonance (NMR) microscopy to measure self diffusion coefficient of water molecules in an alumina nanofluid.³⁷ The interactions between nanoparticle and water molecules, and geometric effect (nanoparticles as a physical obstruct for water diffusion) were put forward as reasons for the observed

decrease in diffusivity with respect to alumina content. Similarly, Turanov and Tolmachev reported no anomalous change in thermal conductivity and water self diffusion coefficient (SDC) in quasi-monodisperse silica nanofluids.⁶²

In a recent work, Veilleux and Coulombe investigated mass diffusion of rhodamine 6G in aqueous alumina suspensions up to 4 vol% inside a millichannel geometry by means of total internal reflection fluorescence (TIRF) microscopy.³⁵ They observed diffusivity of rhodamine 6G reached up to an order of magnitude for the 2 vol% suspension which is different from the volume percentage of alumina suspension (0.5 vol%) at which peak value of fluorescein dye diffusion enhancement had been reported (Figure 3).³¹

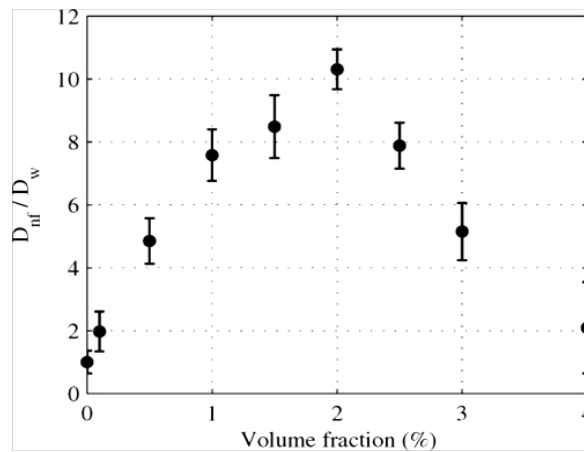


Figure 3. The ratio of measured diffusion coefficients of rhodamine 6G in alumina suspensions (D_{nf}) to the one measured in water (D_w) as a function of volume fraction.³⁵ The data plotted is the average of five experiments and the error bars indicate the one standard deviation taken on them “Reprinted with the permission from Veilleux, J.; Coulombe, S. *J Appl Phys* 2010, 108, (10), 104316. Copyright 2010 American Institute of Physics.”

The underlying reason for this unexpected peak value was unclear again, but they postulated that the interactions among the particles at high volume fractions decreases the contribution of nanoparticles Brownian motion to mass diffusion of tracer dye. The Brownian motion induced microscale dispersion model also predicted an enhancement over an order of magnitude (~ 30). Strictly speaking, the chemical composition of suspensions needs to be known in order to draw correct conclusions about their heat or mass transfer applications. In these experimental results reported by authors, the stabilizer of water based colloidal system was not clearly defined. The existence of a possible polymer stabilizer, which was obvious from the visual appearance of these commercial suspensions purchased from Nanostructured & Amorphous Materials, Inc. (Houston, TX), could alter the certain direction of the results due to possible interaction effects between surfactant and dye.

Interphase Mass Transport Studies

The considerable amount of research on nanofluids has also gone into other mass transport areas including gas-liquid mass transfer. Olle et al. noticed that aqueous dispersions of Fe_3O_4 (< 1 vol%) improved oxygen mass transfer into water up to 600% in an agitated, sparged reactor.⁶³ Both the mass transfer coefficient (k_L) and the gas-liquid interfacial area contributed to total enhancement. Especially interfacial area calculated from experimental measure of the absorption rate is responsible from greater fraction (80% or more) of total oxygen transfer enhancement. Zhu and co-workers emphasized the effects of surface characteristics of 250 nm-MCM41 nanoparticles on CO-water mass transfer enhancement.⁶⁴ For example, when too many hydrophobic

groups like methyl or aminopropyl grafted to nanoparticle surface, the enhancement diminished due to instability. In the experiments, the highest CO-water mass transfer enhancement of 1.9 times that of particle free fluid was obtained with mercaptopropyl or mercaptoundecyl groups grafted nanoparticle surface.

The effect of alumina, copper and copper oxide nanoparticles on the bubble absorption performance of ammonia vapors in a $\text{NH}_3/\text{H}_2\text{O}$ solution was experimentally studied by Kim et al.⁶⁵ The enhanced absorption rate with addition of nanoparticles was explained by the grazing effect, which is the movement of particles in the liquid media towards the film layer of concentration boundary to adsorb the gas and desorption of the gas into bulk nanoparticle laden liquid. Copper nanoparticles with more than threefold increase in absorption ratio gave the most effective performance. The superior enhancing effect of the surfactant (2-ethyl-1-hexanol) on the absorption rate of $\text{NH}_3/\text{H}_2\text{O}$, in comparison to added CuO and Al_2O_3 nanoparticles, was also reported in another work done by the same authors.⁶⁶ Addition of 2-ethyl-1-hexanol at optimum concentration of 700 ppm caused significant enhancement (4.8 times) in the absorption rate with respect to surfactant free fluid. The surfactant added nanofluid usage was recommended for best absorption performance results. Lee and coworkers again compared absorption rates with addition of 2-ethyl-1-hexanol and arabic gum in the falling film absorption experiments done with alumina nanoparticle laden $\text{H}_2\text{O}/\text{LiBr}$ fluid.⁶⁷ Moreover, they observed better absorption enhancing performance of carbon nanotubes with respect to iron nanoparticles for the same fluid system.⁶⁸ Lee et al. also found that carbon nanotubes with high aspect ratios (25 nm in diameter and 10 μm in length) gave lower

absorption performance than the alumina particles (25 nm in diameter) on pool type absorption studies.⁶⁹

The research studies related to the applications of nanofluids in mass transfer areas have produced the controversial results on the reported enhancements. Furthermore, there are many uncertainties in the magnitudes of the effects of the colloidal system components. Consequently, the research community has not been able to reach a solid consensus on the possible mechanisms behind the reported results. Further comprehensive studies are still needed to understand the true effect of nanoparticles on mass transfer enhancement.

2.3 Heat Transfer Studies in Nanofluids

Thermal Conductivity Studies

Experimental research on nanofluids has implied superior thermal performance of these engineered nanoparticle suspensions with respect to conventional heat transfer fluids.^{10, 13, 15, 20, 22-24, 27} Thermal conductivity is the most important parameter responsible for enhancement in heat transfer. There are multiple techniques applied to measure thermal conductivity in nanofluids; transient hot wire, steady state temperature oscillation and 3w-wire techniques.^{13, 18, 70, 71} Although each method has specific drawbacks when used for nanofluids, the transient hot wire technique is a simple, accurate and reliable technique because the measurement is very fast, thereby eliminating the error generated by liquid natural convection.²⁷ A portable thermal property analyzer based on this technique was used in the thermal conductivity

measurements of this study (see Experimental Methods). Figure 4 prepared by Murshed et al. shows the enhancing effect of suspended nanoparticle concentration on the thermal conductivities of studied fluids.²⁶ Thermal conductivities of nanofluids increase as a function of type, size and concentration of particles.

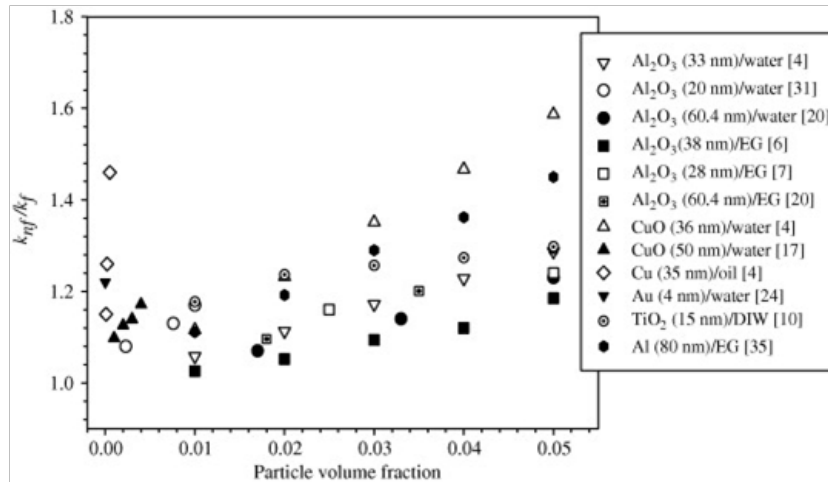


Figure 4. Comparison of experimental results of the thermal conductivity enhancement with nanofluids.²⁶ “Reprinted from Applied Thermal Engineering, 28, (17-18), Murshed, S.; Leong, K.; Yang, C., Thermophysical and electrokinetic properties of nanofluids-A critical review, 2109-2125, 2008, with the permission from Elsevier.”

Some key parameters including base liquid type, particle concentration, shape and size, temperature, stabilizer and acidity of solution influenced the thermal conductivity enhancement of nanofluids.^{19, 21, 25, 72} Particle type effect can easily be seen in the measurements done with aluminum and alumina nanofluids.^{19, 72} Nanofluids prepared from higher thermal conductive aluminum nanoparticle ($k=237$ W/mK)⁷² exhibited higher ($> 15\%$) thermal conductivities than the nanofluids prepared from lower thermal conductive alumina nanoparticle ($k=30$ W/mK)⁷³ for the same loading of

particles (5 vol%) in ethylene glycol.¹⁹ Lee et al. reported a little higher thermal conductivity enhancement (23%) in 4 vol% copper oxide laden ethylene glycol suspensions in comparison to 18% enhancement with aqueous copper oxide suspensions.²⁷

In another study done by Chon et al., thermal conductivity values of aqueous alumina suspensions at 1 vol% increased with increasing nanofluid temperature from 21°C to 71°C and with decreasing nanoparticle size from 47 nm to 11 nm.²¹ Lee and coworkers reported that when the pH of a copper oxide suspension was decreased from 6 to 3, effective thermal conductivity enhancement increased from 7% to 12%, which was attributed to surface charge state of particles in colloidal system.⁷⁴ Assael et al. investigated thermal conductivity enhancement of multi-wall carbon nanotubes (5 nm in diameter).⁷⁵ According to their measurements done with 0.6 vol% carbon nanotubes, the observed enhancement was lower for the suspensions prepared with hexadecyltrimethyl ammonium bromide (CTAB) than the ones with Nanospense AQ. Surprisingly, although the same homogenization time period was applied to both suspensions, suspensions with CTAB showed better stability performance.

To resolve the inconsistencies in reported thermal conductivity data, Buongiorno et al. did a benchmark study with various researchers around the world using the identical nanoparticle suspensions.⁷⁶ Four different types of set comprised of metal and metal oxides samples were sent to all the participants in order to compare thermal conductivity data obtained by different experimental techniques. It can be summarized that, although thermal conductivity of suspensions increased with increasing particle

loading and/or decreasing base liquid thermal conductivity, no anomalous enhancement was reported in the experimental data.

The relatively scattered data from numerous experimental studies prompted controversies about theoretical works predicting thermal conductivities of suspensions. The first method developed over a century ago was Maxwell's equation (1)⁷⁷ where effective thermal conductivity represented by

$$\frac{k_{eff}}{k_f} = \frac{k_p + 2k_f + 2(k_p - k_f)\phi}{k_p + 2k_f - 2(k_p - k_f)\phi} \quad (1)$$

where k_{eff} is the effective thermal conductivity of suspension, k_p is the thermal conductivity of the particle, k_f is the thermal conductivity of fluid and ϕ is the volume fraction of particles. Maxwell's classical theory prediction was in good agreement with experimental data taken by Buongiorno et al.⁷⁶ This model is especially good for large particles at low volume fractions. Hamilton and Crosser⁷⁸ modified it by applying shape factor and introduced an expression

$$\frac{k_{eff}}{k_f} = \frac{k_p + k_f(n-1) + (k_p - k_f)(n-1)\phi}{k_p + k_f(n-1) - (k_p - k_f)\phi} \quad (2)$$

where n is the empirical shape factor, defined as $n = 3/\varphi$. The particle sphericity, φ , is the ratio of the surface area of a sphere to the surface area of the particle, and its value for sphere and cylinder is equal to 1 and 0.5 respectively. The experimental results taken by Lee et al. on with alumina laden suspensions was supported by Hamilton and Crosser model predictions.²⁷ However, these models only considered volume fraction of particles

and thermal conductivities of particle and liquid not the effects of particle size, aggregation of particles or Brownian motion of the particles.

After the failure of the classical models, new theoretical studies were conducted.⁷⁹ For example, Koo and Kleinstreuer developed a modification to Maxwell model considering the effects of particle volume fraction and size, physical properties of liquid and particle, and temperature.^{80, 81}

$$\frac{k_{eff}}{k_f} = \frac{k_p + 2k_f + 2(k_p - k_f)\phi}{k_p + 2k_f - 2(k_p - k_f)\phi} + 5 \times 10^4 \beta \rho_f C_f \phi \sqrt{\frac{k_B T}{\rho_p D} \frac{f(T, \phi)}{k_f}} \quad (3)$$

where ρ_f and C_f are the density and heat capacity of the fluid, ρ_p is the particle density, k_B is the Boltzmann constant (1.381×10^{-23} J/K), D is the particle diameter, T is the temperature, f is a function of volume fraction, temperature is defined as $f(T, \phi) = (0.4705 - 6.04\phi)T + 1722.3\phi - 134.63$ and β is empirically determined parameter and $\beta = [0.0137(100\phi)^{-0.8229}, \phi < 0.01 \text{ and } 0.0011(100\phi)^{-0.7272} \phi > 0.01]$.

Another empirical model considering the temperature was proposed by Li and Peterson for aqueous alumina suspensions.²⁵

$$\frac{k_{eff}}{k_f} = 0.764481464\phi + 0.018688867T + 0.537852825 \quad (4)$$

Several mechanisms have been claimed for description of enhancement in thermal conductivity of nanofluids.^{17, 82, 83} The nanoparticles move randomly in a solution and even collide due to Brownian motion thereby helping heat transport one particle to another which can be expected to increase thermal conductivity. In the interfacial liquid layering mechanism, local ordering of liquid molecules which acts as a

thermal bridge between particle and bulk liquid could be expected to lead to higher thermal conductivity. But, this static mechanism could not explain the strong temperature dependence of the conductivities. Another possible scenario was ballistic phonon transport in which ballistic phonons initiated in one particle could move in near liquid and reach another particle causing unusually high thermal conductivity enhancement. There is still debate among the studies, but nanoparticle clustering is widely speculated as the responsible mechanism.^{17, 84, 85} It was proposed that the clustering of particles might lead to form percolating networks which could create paths of lower thermal resistance and enhance thermal conductivity significantly. On the other hand, Eastman et al. also noted that clustering might create large particle free regions in liquid particularly at low volume fractions of nanoparticles.¹⁷ By considering these mechanisms, many theoretical models (particle-liquid interfacial layer,⁸⁶ average polarization theory,⁸⁷ Brownian motion and aggregation,^{83, 88} clustering and polarization of nanoparticles⁸⁴) have been proposed for predicting the thermal conductivities of nanofluids.

There are still no available satisfactory theoretical models to predict anomalous thermal conductivity of nanofluids. It may require that instead of one pure mechanism, using a more comprehensive model with combined effect of other mechanisms can give better agreement with experimental results. Therefore, further theoretical and experimental investigations need to be done in order to understand the physical phenomena behind unexpected superior thermal performance of nanofluids.

Investigation of Flow and Heat Transfer Characteristics

Suspending highly-thermal conductive and nano-sized solid particles at sufficient volume fractions in the heat transfer fluids can change transport properties, flow features and enhance thermal performance. For example, the Nusselt number $[hL/k]$, which takes into account the fluid thermal conductivity, represents heat transfer resistance of flowing fluid. Therefore, if thermal conductivity of a heat transfer fluid is increased by adding nanomaterials, the emerging thermally low resistant suspension can be offered as an alternative coolant for improving the performance of heat transfer applications. However, the net benefit of nanofluid as a heat transfer fluid can only be evaluated by considering other factors such as changes in density, viscosity and specific heat.

The effects of nanofluids on heat transfer have been investigated at different fluid conditions; laminar flow, turbulent flow and pool boiling. Ding et al. suspended multiwall carbon nanotubes in water and measured convective heat transfer coefficient under laminar flow. At a given carbon nanotube concentration (0.5 wt%), max enhancement was more than 350% when the Reynolds number was equal to 800 and axial distance was 110 times diameter ($x/D=110$).⁸⁹ Besides the increase in thermal conductivity, the authors proposed particle rearrangement, high aspect ratio of carbon nanotubes (>100), shear induced thermal conduction enhancement and reduction of thermal boundary layer thickness as reasons for large enhancement in convective heat transfer coefficient. Pak and Cho studied the convective heat transfer in a circular tube using Al_2O_3 and TiO_2 suspensions as the flowing medium under turbulent conditions.²⁸ They reported that the convective heat transfer coefficient increased with increasing

Reynolds number and volume concentration of particles (Figure 5). The results of the experimental study done by Xuan and Li with Cu/H₂O system also confirmed the enhancing effect of nanoparticles on the convective heat transfer coefficient even without extra penalty of pump power.⁹⁰

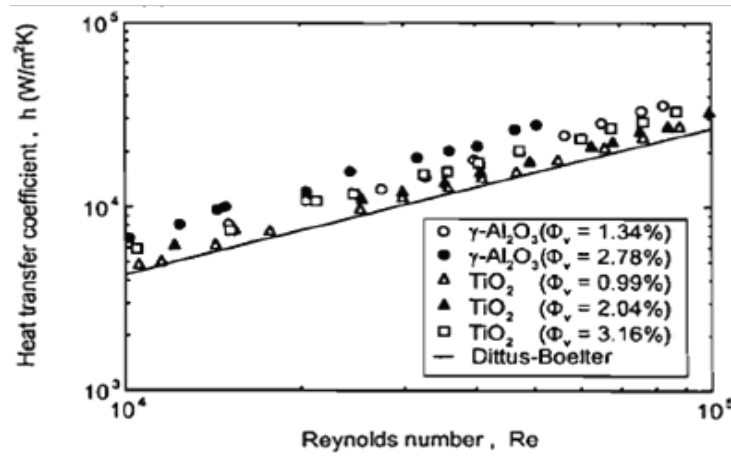


Figure 5. Heat transfer coefficient versus Reynolds number.²⁸ “Reprinted with the permission from Pak and Cho, 1998”

The available experimental results from the applications of nanofluids on natural convective and boiling heat transfer are limited. Putra et al. observed heat transfer deterioration in the natural convection experiments done with Al₂O₃ and CuO suspensions.⁹¹ This paradoxical behavior depended on particle type, density and concentration as well as aspect ratio of the horizontal cylinder in which nanofluids were placed. Wen and Ding also reported systematical decrease (up to 30%) in natural convective heat transfer coefficient in the presence of stable aqueous-based TiO₂.³⁰

In another experimental setup, alumina nanofluid enhanced the boiling heat transfer significantly (~40% at 1.25 wt%) in the experiments done by Wen and Ding with cylindrical boiling vessel (Figure 6).²⁹

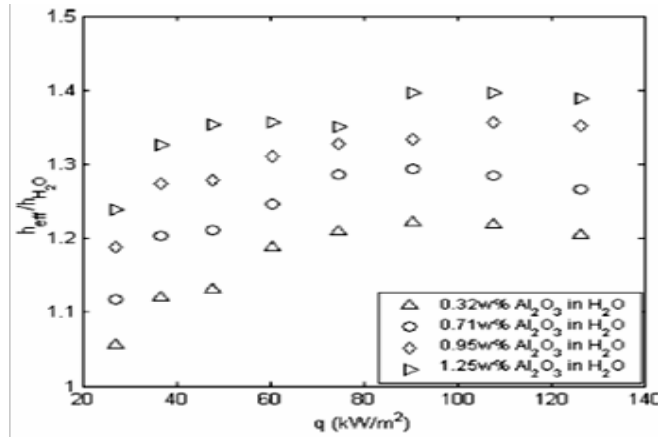


Figure 6. Improvement on heat transfer coefficient of nucleate pool boiling due to the presence of alumina nanoparticles.²⁹ “Reprinted from Journal of Nanoparticle Research, 7, (2), 2005, 265-274, Experimental investigation into the pool boiling heat transfer of aqueous based -alumina nanofluids, Wen, D., Ding, Y., Figure 7, with kind permission from Springer Science and Business Media.”

Das et al. also carried out an experimental study on boiling heat transfer using aqueous alumina suspensions on a smooth cylindrical surface with a diameter of 20 nm.¹² However, they observed deterioration effect of alumina nanoparticles (38 nm) on pool boiling performance, and it was attributed to smoothness of surface caused by trapped particles in rough surface. Trisaksri and Wongwises got similar results with TiO₂/R141b refrigerant based nanofluids systems.⁹²

Most of these conflicting results also lack the explanation of physical phenomena behind the observed change. Further detailed experimental work is still required in these areas to understand the reasons of the heat transfer characteristics.

2.4 Rheological Behaviour of Nanofluids

Rheological properties of nanofluids should be investigated carefully in order to determine required pumping power. The amount and type of the particle, and fluid temperature have been reported to be effective on observed viscosity values of nanofluids. Therefore an undesirable increase in pressure drop that is directly proportional to pumping power needs to be considered in any relevant application. Moreover, recent studies have also pointed out the relationship between the rheological and thermal behavior.

There are also some discrepancies in the reported behavior of nanofluids. Pak and Cho measured the viscosities of aqueous alumina (13 nm) and titania (27 nm) suspensions up to 10 vol% using Brookfield rotating viscometer. According to their results, both nanofluids showed Newtonian behavior and viscosity of alumina suspensions was much higher than titania ones.²⁸ The switch from Newtonian to Shear thinning was also detected at higher particle volume fraction. Putra et al. also conducted viscosity measurements of alumina nanofluids (1-4 vol%) using disc type rotating rheometer.⁹¹ The viscosity values found to be constant against shear rate were higher than the pure water and inversely proportional to temperature. Heris et al. observed Newtonian behavior for aqueous CuO and Al₂O₃ suspensions (0.2-3 vol%) as well.⁹³ They indicated large particle size of copper oxide nanoparticles (50-60 nm) with respect

to alumina nanoparticles (20 nm) as a reason for higher viscosity values of these suspensions.

As it is seen from Figure 7 prepared by Wen and Ding, TiO₂ suspensions behavior changed from Newtonian to shear thinning fluid with an increase in nanoparticle concentration.³⁰ This might be a corroborant for better fluid flow performance in the channels because higher shear rate at the wall result in low viscosity there.

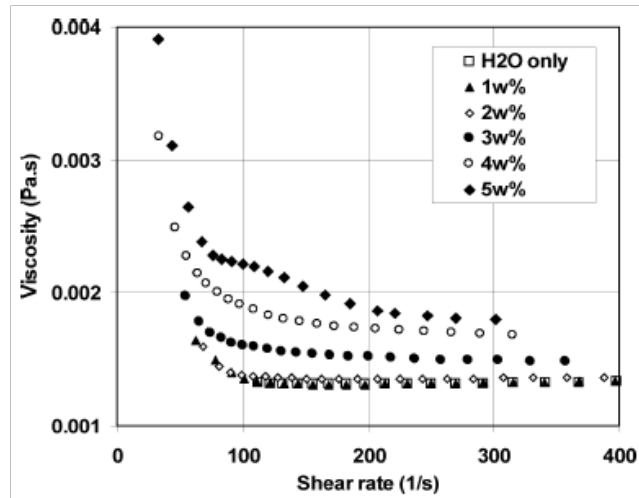


Figure 7. Viscosity of TiO₂ nanofluids as a function of shear rate.³⁰ “Reprinted with the permission from Wen and Ding, © 2006 IEEE.”

Similar results were given by Kwak and Kim.⁷¹ When the concentration of CuO particles in ethylene glycol was increased, Newtonian behavior of solution changed to shear thinning one. Chen et al. observed increasing effect of temperature on the shear thinning behavior of titanate nanotubes (100 nm long and 10 nm in diameter).⁹⁴ Aqueous carbon nanotube suspensions also exhibited more dramatic shear thinning behavior than

the spherical nanoparticles.⁸⁹ Davis and coworkers even reported local maximum and minimum viscosity values of single wall carbon nanotubes at different concentrations in superacids (sulfuric acid with various level of excess SO₃) due to change in phase behavior of tubes from Brownian rod to spaghetti-like self-assembled supermolecular strands of mobile, solvated tubes.⁹⁵

The viscosity of liquid suspensions has also been predicted since Einstein.⁹⁶ Einstein model (5) for evaluating the effective viscosity of suspensions of non-interacting small rigid spherical particles can be expressed as

$$\frac{\mu_{eff}}{\mu_f} = 1 + 2.5\phi \quad (5)$$

where μ_{eff} is the effective viscosity of mixture, μ_f is the viscosity of fluid, and ϕ is the volume fraction of particles. This equation is valid for dilute suspension systems with non-interacting particles where ϕ should be less than 3 vol%. In the measurements done by Prasher et al., viscosity of Al₂O₃/Propylene glycol (PG) was much higher than the value predicted by Einstein's model.⁹⁷ They proposed nanoparticle aggregation as a reason for this unexpected increase. They also reported that if increase in viscosity with nanoparticle addition relative to the increase in thermal conductivity is less than four, using nanofluid is advantageous.

There have been other models offered for predictions of suspensions' viscosities. Brinkman⁹⁸ modified Einstein's model and obtained

$$\frac{\mu_{eff}}{\mu_f} = \frac{1}{(1-\phi)^{2.5}} \quad (6)$$

Another model applicable to higher particle concentrations up to 10 vol% proposed by Batchelor⁹⁹ (Equation 7) has considered the effect of Brownian motion of the particles on the bulk stress.

$$\frac{\mu_{eff}}{\mu_f} = 1 + 2.5\phi + 6.2\phi^2 \quad (7)$$

Maiga et al. proposed nanoparticle specific equations using a least-square curve fitting method to experimental data¹⁰⁰

$$\frac{\mu_{eff}}{\mu_f} = 1 + 7.3\phi + 123\phi^2 \quad \text{for water-}\gamma\text{Al}_2\text{O}_3 \quad (8)$$

$$\frac{\mu_{eff}}{\mu_f} = 1 - 0.19\phi + 306\phi^2 \quad \text{for ethylene glycol-}\gamma\text{Al}_2\text{O}_3 \quad (9)$$

Tseng and Lin found an exponential relation between μ_{eff}/μ_f and volume fraction of anatase titanium dioxide (TiO₂) nanoparticles in water and laid emphasis on

$$\frac{\mu_{eff}}{\mu_f} = 13.47e^{35.98\phi} \quad (10)$$

particle aggregation due to strong attraction as ϕ increased.¹⁰¹

The reported experimental data on viscosity of nanofluids are still higher than the available theoretical predictions. No firm conclusions can be drawn due to the differences in rheological behavior of studied nanofluids which depends on particle

properties (type, concentration, shape and size), base liquid type, particle-particle (aggregation) and particle-liquid interactions.

2.5 Nanorefrigerants

Most investigations have focused on idealized aqueous-based suspensions, with relatively little attention devoted to more realistic formulations based on commercial refrigerants. The refrigerant suspensions (nanorefrigerants), prepared from highly-thermal conductive and nano-sized solid particles at sufficient volume fractions, are a new research avenue in this scope. A thermally low resistant refrigerant with optimized transport and flow properties could be an innovative coolant for improving the performance of cooling and refrigeration systems. Although anomalous thermal conductivity enhancements were reported in the literature with water and ethylene glycol based suspensions,^{12, 102, 103} thermal properties of the real refrigerant-based suspensions have not been examined well.

Moreover, clear trends in the studies where refrigerants employed are difficult to distinguish owing to large disparities in the reported results. Jiang et. al. investigated thermal conductivity of carbon nanotube dispersions in R113 refrigerant, observing a two fold enhancement in thermal conductivity.¹⁰⁴ Jwo et al. reported up to 5% enhancement in thermal conductivity with alumina nanoparticle loading to the lubricant of R134a refrigeration system.¹⁰⁵ Naphon et al. presented a heat pipe efficiency increases up to 1.4 for 0.1% titanium nanoparticle concentration in the refrigerant (R11).¹⁰⁶ Bi et. al. reported an energy savings of over 20% in Al₂O₃ and TiO₂ nanoparticle-based suspensions in HFC134a refrigerant with mineral oil added as a lubricant as well.⁵⁴

On the other hand, the studies on boiling heat transfer characteristics of nanorefrigerants have generated controversy due to inconsistent findings from the experimental tests. For example, Park and Jung observed decreased fouling and enhancements on nucleate boiling heat transfer coefficients up to 36.6% with carbon nanotubes laden R123 and R134a refrigerants.¹⁰⁷ Peng et. al. reported enhancements in flow boiling heat transfer coefficients of up to 29.7% with addition of CuO nanoparticles in R113 refrigerant.⁵⁵ Henderson and coworkers observed an over 100% enhancement in heat transfer coefficient when CuO nanoparticles were suspended in a mixture of R-134a and polyolester oil, whereas a decrease in flow boiling heat transfer coefficient was obtained when SiO₂ nanoparticles were employed.⁵³ Trisaksri and Wongwises also reported degradation in pool nucleate boiling heat transfer upon dispersal of TiO₂ nanoparticles in HCFC 141b.⁹²

The formulation of innovative refrigerant with enhanced thermal properties is crucial in the development of advanced cooling systems. The present findings on nanorefrigerants are compelling and further experimental and theoretical research should be undertaken in order to see the effect of composition, nanomaterial properties (size, morphology, concentration) and particle migration and circulation on the measurements.

3. EXPERIMENTAL METHODS

3.1 Introduction

In this section, preparation of nanofluids (water and refrigerant based suspensions), set-ups and systems used for tracer dye diffusion, thermal conductivity and viscosity measurements, as well as methods applied for characterization are described in detail.

3.2 Nanofluids Preparation and Characterization

Tracer Dye Diffusion Experiments

Aqueous suspensions of Al_2O_3 nanoparticles were prepared at final concentrations ranging from 0.25 to 1 vol % by dilution in deionized water from a commercially available 15.4 wt% Al_2O_3 solution (Nanomyte™; NEI Corporation, Somerset, NJ) specially ordered to include no stabilizing surfactant. According to the manufacturer, the alumina nanoparticles in these suspensions have a spherical morphology with an average primary particle size in the range of 40-50 nm. This formulation was selected because it provided the best tradeoff between stability against sedimentation and the ability to control the composition and amount of surfactant added to stabilize the suspension after addition of fluorescent dye. Suspension stability was particularly important in our microfluidic experiments because total setup and running times of order 1 h were required owing to the low flow rates imposed.

The nanoparticle suspensions were prepared by adding surfactant (Tween-80, Cat. No. P1754; Sigma-Aldrich, St. Louis, MO; or sodium dodecyl sulfate (SDS), Cat. No. BP166; Fisher Scientific, Fair Lawn, NJ) to an appropriate dilution of the as supplied commercial nanofluid. Surfactant concentrations of 5.35 mg/ml and 15 mg/ml were used for Tween-80 and SDS, respectively, and were chosen to be well above each surfactant's critical micelle concentration (0.016 and 2.5 mg/ml for Tween-80 and SDS, respectively). The suspension was then mixed for 5 h using a magnetic stirrer, followed by 5 h of ultrasonic agitation in an ultrasonic cleaner (Model 3510DTH; 100 W, 40 kHz, Branson Ultrasonics Corp., Danbury, CT), and then 30 min of agitation using a 750 W, 20 kHz probe sonicator (Vibracell VCX 750; Sonics & Materials Inc., Newtown, CT) at 100% amplitude to ensure homogeneity and stability (Figure 8a, b and c).

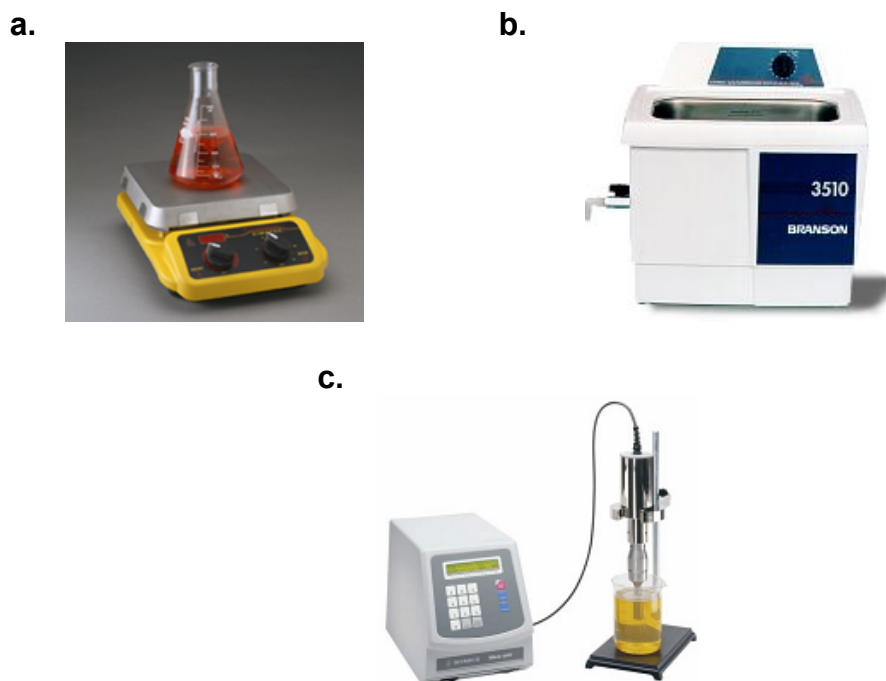


Figure 8. Photographs of the used devices. (a) The digital stirring hot plate (Model Cimarec SP131325; Barnstead Thermolyne Corp., Dubuque, IA), (b) The ultrasonic cleaner (Model 3510DTH; Branson Ultrasonics Corp., Danbury, CT), (c) A probe sonicator (Vibracell VCX 750; Sonics & Materials Inc., Newtown, CT).

Nanoparticle volume percentages were determined from the suspension weight percentages using the equation

$$\phi_v = \frac{1}{\left(\frac{\rho_p}{\rho_f}\right)\left(\frac{100}{\phi_m}\right) + 1} \times 100(\%) \quad (11)$$

where ρ_p and ρ_f are the densities of particle and host liquid respectively, and ϕ_v and ϕ_m are the volume and weight percentage of the suspensions. The properties of alumina and water are listed in Table 1. The weight fraction of chosen volume fraction of suspension was first calculated, and using this weight fraction, the particle amount necessary for

suspension sample was determined. Then necessary amount of fluid was taken from stock commercial aqueous Al₂O₃ solution (15.4 wt%) and diluted to the desired volume percentage with deionized water.

Table 1. Specifications of tested nanofluid.

Phase	Formula	Density (g/cm³)	Thermal Conductivity (W/mK)
Solid	Al ₂ O ₃	3.97	30 ⁷³
Liquid	H ₂ O	~1	0.607 ¹⁰⁸

Two different fluorescent tracer dyes were studied for the diffusion experiments. Solutions used for comparison with the KBPP experiments were prepared by dissolving 330 mg of fluorescein powder (free acid, Cat. No. 46955; Fluka Analytical, Buchs, Switzerland) in 0.5 ml methanol (Cat. No. A412-1, Fisher Scientific, Fair Lawn, NJ) to solubilize the dye, after which, 9.5 ml deionized water was added. This mixture was then diluted in water by a factor of 100 to obtain final concentration of 0.33 mg/ml. The same fluorescein concentration given in Krishnamurthy et al.s' paper³¹ was used in the experiments. Aqueous solutions containing Rose Bengal (sodium salt, Cat. No. R3877; Sigma-Aldrich St. Louis, MO) were prepared by dissolving the powdered dye in water to yield final concentrations ranging from 0.25 – 5 mg/ml. Dye solutions were mixed using a magnetic stirrer for 3 h, followed by 30 min of ultrasonic agitation in a Branson 3510-DTH ultrasonic cleaner, and another 3 h of mixing with a magnetic stirrer. Suspensions containing fluorescent tracers were prepared by adding an aqueous dye solution during

the final stage of suspension described above (mixing with water). When necessary, sonication and mixing times were doubled to counteract the increased tendency toward sedimentation due to interactions between the dye, surfactant, and nanoparticles.

Suspension Stability Probe Studies

These nanoparticle suspensions were also prepared from 15.4 wt% Al₂O₃ solution (Nanomyte™; NEI Corporation, Somerset, NJ) using the same procedure described above.³⁸ Its superior stability performance made this commercial suspension the best candidate for future experiments done with tracer dyes (Figure 9c). On the other hand, it was found that the sufficient stability using suspensions prepared directly from alumina nanoparticles (90%α, 10%γ, APS 30-40 nm, ρ_p = 3.7 g/cm³) purchased from Nanostructured & Amorphous Materials, Inc., (Houston, TX) was unable to be achieved as evident by sedimentation inside the syringes loaded into the pump during the course of the microfluidic experiments and sedimentation test experiments (Figure 9) although different surfactants (Tween-80 (0.016 mg/ml) and SDS (2.5 mg/ml)) and much longer ultrasonication times (10 h in an ultrasonic cleaner, followed by 2 hrs of agitation using a probe sonicator) were tried. Raghu et al. asserted the difficulty of dispersing these alumina nanoparticles purchased from the same company into water as well.¹⁰⁹ In the course of these experiments, it was observed that SDS was a more effective surfactant with respect to Tween 80 to eliminate particle sedimentation as it is seen in Figure 9a and b. Alumina suspension prepared with Tween 80 loses its stability easily and alumina nanoparticles settle out quickly from solution even in 1 hour, leaving upper fluid more

transparent. Negatively charged SDS molecules were electrostatically adsorbed on positively charged alumina surface. Tween 80 is a nonionic surfactant and most nonionic surfactants do not adsorb significantly on alumina surfaces¹¹⁰ and would not be expected to stabilize these suspensions as efficient as ionic surfactants. Unlike the ionic surfactant case, no electrostatic interactions prevail in these systems.

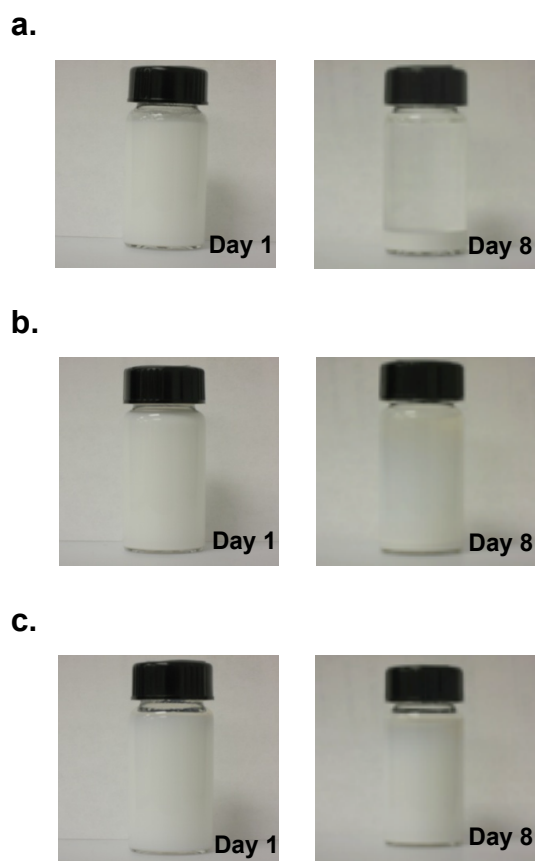
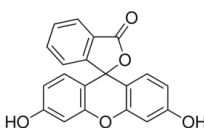
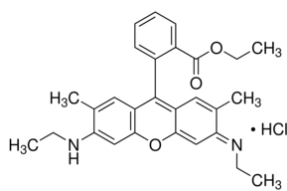
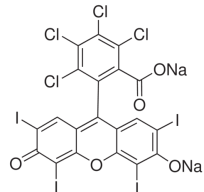


Figure 9. Photographs of suspensions (a) Al_2O_3 (1 vol%, Nanoamor Inc.), Tween 80, H_2O , (b) Al_2O_3 (1 vol%, Nanoamor Inc.), SDS, H_2O , (c) The suspension prepared from Al_2O_3 (1 vol%, NEI Inc.), H_2O is still stable after more than 1 week in the stationary state without sedimentation.

Three fluorescent tracer dyes with different ionic characteristics were employed in this set of experiments (Table 2). The same preparation recipe used in diffusion studies was applied for the solutions with fluorescein dye to obtain a concentration of 0.33 mg/ml. Particle-free aqueous dye solutions of rhodamine 6G (Cat. No. R4127; Sigma-Aldrich, St. Louis, MO) were prepared by dissolving the powdered dye in water to yield a final concentration of 0.5 mg/ml. Methanol (5 vol. %, Fisher A412-1) was also added in aqueous solution to solubilize the dye. Similarly, Rose Bengal dye powder (sodium salt, Cat. No. R3877; Sigma-Aldrich, St. Louis, MO) was dissolved in water to a concentration of 5 mg/ml. All particle-free aqueous dye solutions were mixed using a magnetic stirrer for 3 h, followed by 30 min of ultrasonic agitation in a Branson 3510DTH ultrasonic cleaner, and then another 3 h of mixing with a magnetic stirrer.

Table 2. The tracer dye structure and concentrations.

Dyes:	Charge:	Structure:	Solubility Limit Concentrations [mg/ml]	Studied Concentrations [mg/ml]
Fluorescein	Neutral		0.33	0.33
Rhodamine 6G	Cationic		20	0.5
Rose Bengal	Anionic		100	5

Alumina suspensions were mixed with aqueous fluorescent tracers during magnetic stirring stage. To keep the stability in dye-laden suspensions, sodium dodecyl sulfate (SDS) was added to an appropriate dilution of stock nanofluid solution (15.4 wt%, Nanomyte™; NEI Corporation, Somerset, NJ). Then they were mixed for 5 h using a magnetic stirrer, followed by 5 h of ultrasonic agitation in an ultrasonic cleaner (Model 3510DTH; Branson Ultrasonics Corp., Danbury, CT), and then 30 min of agitation using a probe sonicator (Vibracell VCX 750; Sonics & Materials Inc., Newtown, CT) to ensure homogeneity and stability.³⁸ The pH values of tracer dye containing suspensions were measured using a Chekmite pH-25 meter (Corning Inc., Lowell, MA).

Transmission Electron Microscopy (TEM)

Transmission electron microscopy (TEM) images of Nanomyte™ alumina samples (NEI Corporation, Somerset, NJ) were taken by high resolution analytical TEM instrument; JEOL JEM 2010. The aqueous suspension was deposited on a carbon film TEM grid (Ni mesh) and allowed to dry (evaporation at room conditions) prior to the measurement. Therefore, the particles were not exactly in the colloid behavior, and particularly movements inside the aqueous phase were not characterized. The images were taken in the high vacuum at ~room temperature.

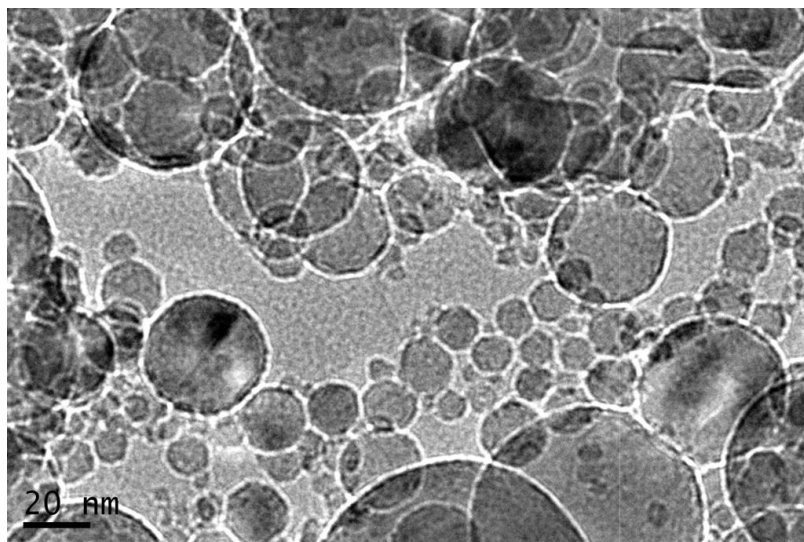
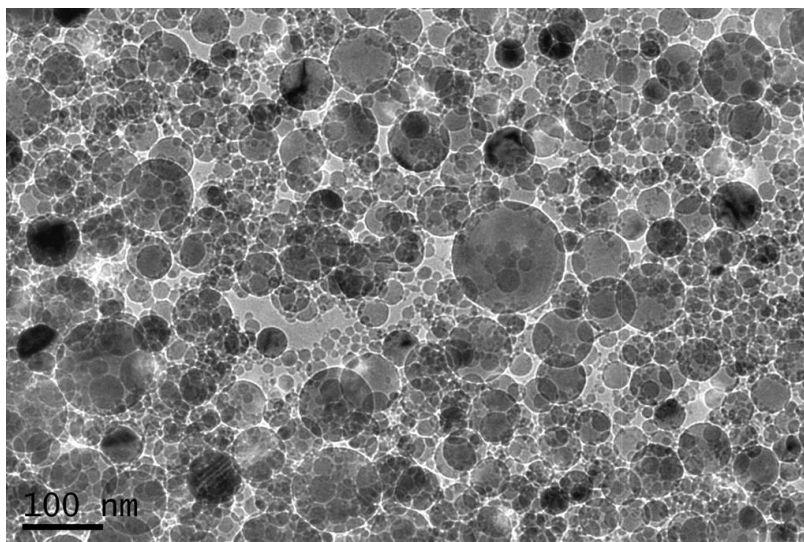


Figure 10. TEM photographs of evaporatively dried aqueous alumina suspension (bars, 100 and 20 nm).

Figure 10 displays a typical TEM image of our alumina nanoparticles used in diffusion and stability probe studies. As it is seen from this micrograph, alumina nanoparticles have a spherical morphology with a particle size in the range of 10-100 nm.

Dynamic Light Scattering (DLS) Measurements

Particle size distributions were characterized by DLS using a ZetaPALS instrument with a BI-9000AT correlator (Brookhaven Instruments Corp.). Samples containing 0.25 vol% alumina nanoparticles were diluted to a concentration of 0.02 vol%. During this process, surfactant (15 or 120 mg/ml) and dye concentrations (0.1, 0.5 or 5 mg/ml) were also diluted by the same amount ($\sim 1/12$). Time-averaged particle size distributions were collected over an analysis period of at least 5 min at room temperature. Six separate measurements were acquired for each freshly prepared solution. The wavelength of the incident laser beam (λ) was 660 nm, and the detector angle (θ) was 90° . The autocorrelation functions were deconvoluted using the built-in, non-negatively constrained, least squares-multiple pass (NNLS) algorithm in order to obtain particle size distribution.

Zeta Potential Measurements

Zeta potential measurements were performed by phase analysis light scattering using a ZetaPALS analyzer (Brookhaven Instruments Corp.). The analyzer was equipped with a 35 mW red diode laser operating at 660 nm. The default settings in the system including dielectric constant, refractive index, and viscosity were assumed to be the same as for water. The Smoluchowski approximation was used as a model for calculations. Samples containing 0.25 vol% alumina nanoparticles were placed in an acrylic cuvette, and 10 measurements were performed at 25 °C. Before testing our solutions, a standard solution (10 wt.%) from Ludox TM-50 colloidal silica suspensions

(Cat. No. 420778, Sigma Aldrich) was also prepared to check the sensitivity of the electrode. Its ionic strength was adjusted with 0.01M KCl solutions. The corresponding zeta potential values were in good range and agreement with the literature.¹¹¹ After confirming the reliability of the probe, zeta potential values of the alumina nanoparticles in 0.25 vol% suspensions were measured.

Preparation of Refrigerant Suspensions

The host fluid consisted of the refrigerant 2-trifluoromethyl-3-ethoxydodecafluorohexane (Novec 7500 Engineered Fluid (I.D. No. 98-0212-2932-85); 3M, St Paul, MN). This formulation displays a boiling point of 128 °C, placing it in the liquid phase under ambient conditions. Data characterizing the refrigerant's temperature dependence of thermal conductivity and viscosity are available from the manufacturer; however this conductivity data are based on a single point measurement using the transient hot wire method, which is then extrapolated based on data from a chemically similar fluid (Figure 11).¹¹²

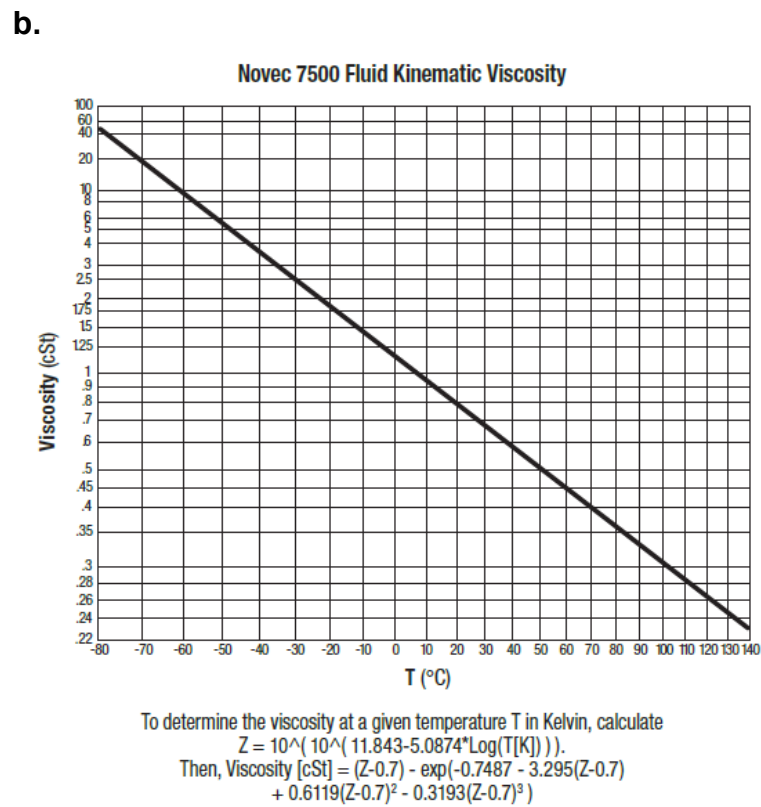
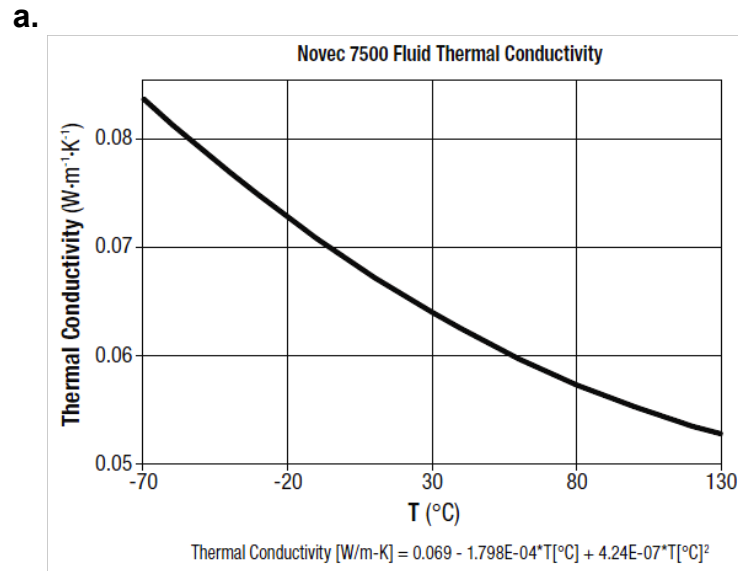


Figure 11. Physical properties of HFE 7500 (3M™ Novec™ 7500 Engineered Fluid). (a) Thermal conductivity versus temperature. (b) Kinematic viscosity versus temperature.¹¹²
 “Reprinted with the permission from 3M Electronics Markets Materials, 2010.”

The graphene nanosheets, multi wall carbon nanotubes, metal oxide and nitride nanoparticles (Al_2O_3 , TiO_2 , ZnO , CuO and AlN) purchased in dry powder form were suspended in the refrigerant (Table 3). Graphene nanosheets were exfoliated from graphite by Cheap Tubes, Inc., (Brattleboro, VT) and Skyspring Nanomaterials, Inc. (Houston, TX). Carbon nanotubes were produced using chemical vapor deposition (CVD) method by Helix Material Solutions, Inc., (Richardson, TX) and Cheap Tubes, Inc., (Brattleboro, VT). Krytox 157 FSL (1 vol%) a low molecular weight (~ 2500 g/mole), monofunctional carboxylic acid-terminated perfluoropolyether ($\rho = 1.9$ g/cm³), supplied by Krytox Performance Lubricants (CAS #60164-51-4, DuPont Chemicals, Deepwater, NJ) was employed as a stabilizer in all suspensions. The nanoparticles from different suppliers such as alumina (90% α , 10% γ Al_2O_3 , APS 30-40 nm) from Nanostructured & Amorphous Materials, Inc., (Houston, TX) and cupric oxide from Sigma Aldrich (Cat. No. 544868) were also tested but found the resulting suspensions' stability to be much lower than the used ones in Table 3.

Table 3. Summary of materials used in nanorefrigerant preparation.

Material	Vendor	Particle size (nm)	Density (g/cm ³) @25 °C	Thermal conductivity (W/m·K) @25 °C
HFE 7500	Novec, 3M Corp. St Paul, MN	–	1.614	0.065 * ¹¹²
Krytox 157 FSL	Krytox Performance Lubricants (CAS #60164-51-4), DuPont Chemicals, Deepwater, NJ	–	1.9	–
Multi-Wall Carbon Nanotubes (MWCNT)	95 wt%** , Cheap Tubes, Inc., Brattleboro, VT	8-15 (length: 10-50 μm)	2.1	~2000 ¹¹³ - 3000 ⁵⁸
Graphene Nanosheets	Helix Material Solutions, Inc., Richardson, TX	10-30 (length: 0.5-40 μm)	1.3	
	Grade 2*** , >97 wt%, Cheap Tubes, Inc., Brattleboro, VT	10 (length: 15 μm)	~0.22	4400-5800 ¹¹⁴
	Skyspring Nanomaterials, Inc. (Cat. No. 0541DX), Houston, TX	5-10 (length: 15 μm)	~0.07	
γ-Al ₂ O ₃	Sigma-Aldrich (Cat. No. 544833), St. Louis, MO	< 50	4	~33 ¹¹⁵
TiO ₂ -Anatase	Sigma-Aldrich (Cat. No. 637254), St. Louis, MO	< 25	3.9	8.37 ¹¹⁶
ZnO	Sigma-Aldrich (Cat. No. 544906), St. Louis, MO	< 100	5.61	54 ¹¹⁷
CuO	NanoArc, Alfa Aesar (Cat. No. 44928), Ward Hill, MA	23-37	~6.4	76.5 ⁵⁸
AlN	Sigma-Aldrich (Cat. No. 593044), St. Louis, MO	< 100	3.26	~319 ¹¹⁸

* Manufacturer values are based on extrapolation of a simple 2-point correlation.

** 233 m²/g surface area, 8-10 nm outside dia., 3-5 nm inside dia., 95 wt% purity, produced by chemical vapor deposition, mixed chirality (data provided by the manufacturer). Electrical conductivity >100 S/cm, Observed layers > 5-15, contains up to 1.5 wt% ash.

*** 100 m²/g surface area, 97 wt% purity, exfoliated from graphite, not oxidized or reduced (data provided by the manufacturer). Observed layers > 30, contains up to 3% silica.

Suspensions at chosen volume concentrations were prepared by combining appropriate amounts of all components (Equation 11) to a final volume of 300 ml, followed by mixing for 5 h using a magnetic stirrer, another 5 h of agitation in an ultrasonic bath (Model 3510DTH, Branson Ultrasonics Corp., Danbury, CT), and a final 30 min of agitation using a probe sonicator (Vibracell VCX 750, Sonics & Materials Inc., Newtown, CT). The surfactant and refrigerant were mixed first (the most chemically miscible components), followed by addition of the nanomaterials. Ice was periodically added to the ultrasonic bath to offset the temperature increase during the 5 h sonication period. It was found that highly stable suspensions could be consistently obtained following this protocol.

Transmission Electron Microscopy (TEM)

The morphology, particle size distribution and crystallinity of the nanomaterials were determined using a Transmission Electron Microscopy (TEM). TEM images of our samples of graphene nanosheet (GNS), multiwall carbon nanotube (MWCNT) and metal oxide and nitride nanoparticles were taken by high-resolution TEM (FEI Tecnai G2 F20ST) equipped with a field emission gun at a working voltage of 200kV. The dilute nanopowder suspensions were prepared with ethanol using ultrasonication (~5 mins). The carbon film coated square mesh copper grids (3 mm, 300 mesh, Pelco) were glow discharged using Pelco easiGlow (Ted Pella Inc., Redding, Ca). Then a small volume of sample was dropped onto a holey carbon film coated grid and allowed to dry overnight by evaporation under ambient conditions. The images were taken in high vacuum (10^{-5} -

10⁻⁶ bar). The electron diffraction patterns for crystal structures were also analyzed and listed as a table in APPENDIX C.

Dynamic Light Scattering (DLS) Measurements

Particle size distributions in nanorefrigerants were also characterized by DLS using a ZetaPALS instrument with a BI-9000AT correlator (Brookhaven Instruments Corp.). The refractive index and dynamic viscosity of refrigerant, and the refractive index of particle were entered into the system software as parameters (Table 4).

Table 4. Typical physical properties of HFE 7500 used in DLS and zeta potential measurements.

Material	Viscosity (cP)	Dielectric Constant	Refractive Index
HFE 7500	1.31*	5.8**	1.298***

* Obtained from our viscosity measurements

** Provided by 3M Catalogue¹¹²

*** Measured by Abbe Refractometer-C10 model

All other experiment conditions are the same with aqueous suspensions measurements. Samples containing 0.25 vol% nanoparticles were diluted to a concentration of 0.02 vol%. During this process, surfactant (1 vol%) was also diluted by the same amount (~ 1/12). Six separate measurements were acquired for each freshly prepared solution.

Zeta Potential Measurements

Zeta potential measurements of nanorefrigerants were performed by phase analysis light scattering using a ZetaPALS analyzer (Brookhaven Instruments Corp.).

The default settings were adjusted again according to our refrigerant properties given in Table 4. The high voltages (50 mV) were applied during the measurements owing to the low dielectric constant of the refrigerant. All other experiment conditions are the same with aqueous suspensions measurements. The concentrations of nanoparticles were diluted to 0.02 vol% solution except CuO and TiO₂ (0.004 vol%). Surfactant concentration in samples was decreased to ~0.1 vol% during the dilution process as well. Samples containing nanoparticles were placed in an acrylic cuvette, and ten measurements, including thirty cycles with three replicates, were performed at 25 °C.

3.3 Microdevice Design and Assembly

Poly(dimethyl siloxane) (PDMS) Microchannels

Microchannels were constructed in poly(dimethyl siloxane) (PDMS) using standard soft lithography methods (Figure 12). Briefly, Y-shaped microchannel patterns (50 µm tall, 500 µm wide, 2.7 cm long from the junction of the two inlets to the downstream outlet) were designed using AutoCAD 2006 software (Autodesk, Inc., San Rafael, CA) and printed on transparency film with a 20,320 dpi (Fineline Imaging, Colorado Springs, CO). Master molds were constructed by spin coating thick photoresist (SU-8 2025; MicroChem Corp., Newton, MA) onto the surface of a silicon wafer at 500 rpm for 10 s with an acceleration of 100 rpm/s followed by 1,460 rpm for 30 s with an acceleration of 300 rpm/s, after which the wafer was baked at 65 °C for 3 min followed by 95 °C for 8 min. The microchannel patterns were then transferred by exposing the wafers to UV light through the transparency film using a mask aligner (Quintel Q-

4000IR; Neutronix-Quintel, Morgan Hill, CA), after which the unexposed photoresist was removed using SU-8 developer solution. This process yielded 50 μm feature heights (corresponding to the depth of the cast microchannels) as determined using a stylus profilometer (Dektak 3; Veeco Instruments, Inc., Plainview, NY).

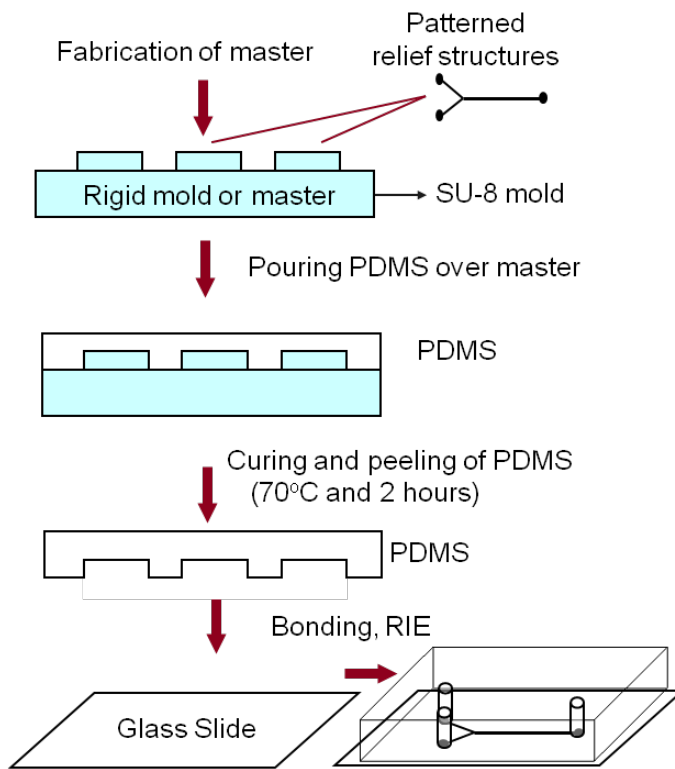


Figure 12. Schematic view of Y shaped PDMS channel production from a rigid mold or master.

The SU-8 master molds were used to cast microchannels in PDMS (SylgardTM 184; Dow Corning Corporation, Midland, MI). The base and crosslinker were mixed in a 10:1 ratio by volume followed by degassing under vacuum for approximately 15 min to remove trapped air bubbles. The mixture was then poured over the master mold and cured at 80 °C for approximately 2 h. The crosslinked PDMS was then peeled away, and access holes were punched at the endpoints (inlets and outlet) of the microchannel using

a sharpened syringe needle (Cat No. 305196; Becton, Dickinson and Company, Franklin Lakes, NJ). The PDMS structures were bonded to 75 x 50 mm, 1 mm thick glass microscope slides (Cat No. 12-550C; Fisher Scientific, Pittsburgh, PA) to produce enclosed microchannels after treating both surfaces in plasma using a reactive ion etcher (Model CS-1701; March Plasma Systems, Concord, CA) for 30 s under the following conditions: O₂ gas flow of 4 sccm, electric power of 25 W, base pressure of 80 mTorr, and temperature of 0 °C.

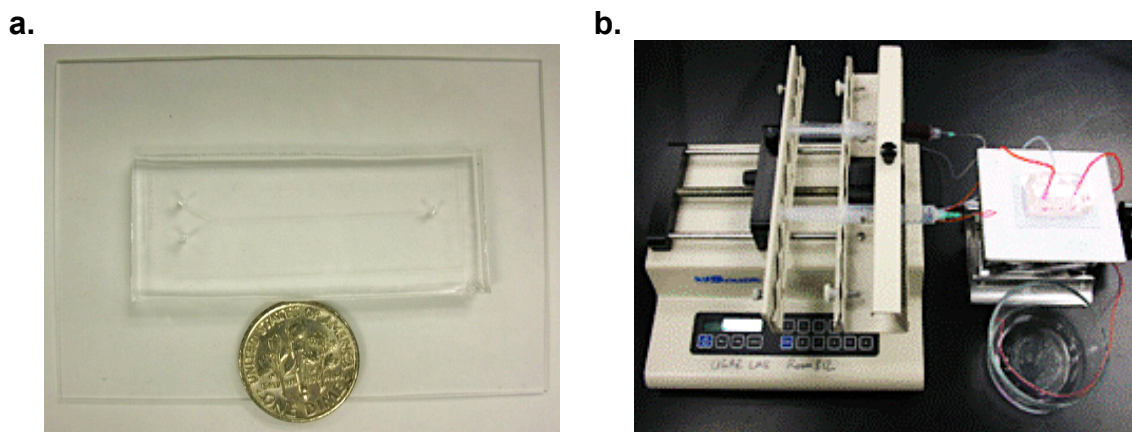


Figure 13. (a) PDMS microfluidic channel produced by using soft lithography. The length of the horizontal channel is 27 mm and its cross sectional dimensions are 500×50 μm. (b) Syringe pump and polyethylene tubings connected to the channel.

Finally, fluidic connections were made by inserting 0.38 mm i.d., 1.09 mm o.d. polyethylene tubing (Intramedic™ (Non-Sterile), Cat. No. 427406; Becton, Dickinson and Company) into the access holes (Figure 13a). Flows at rates ranging from 0.0005 to 0.05 ml/min were generated using a syringe pump (Model KDS-230; kd Scientific Inc., Holliston, MA; or Pico Plus; Harvard Apparatus, Holliston, MA) (Figure 13b).

Thermoplastic Elastomer Microchannels

In stability probe experiments, the microchannels were also prepared from a thermoplastic elastomer substrate by soft lithography.¹¹⁴ The top part of the microchannel was prepared from a mixture of mineral oil (BP2629-1, Fisher Scientific, Hampton, NH) and elastomeric polystyrene-(polyethylene/ polybutylene)-polystyrene (SEBS) triblock copolymer resin (Kraton G1657) in ratio of 2/3. This mixture was placed under vacuum overnight at room temperature and then heated to 180°C under vacuum for 5 h in order to allow mineral oil and resin to intermix uniformly and remove any residual air pockets (Figure 14). By cooling the mixture to room temperature, the slab of elastomer became hardened. Finally, the solid gel was cut into smaller pieces used for microchannels.

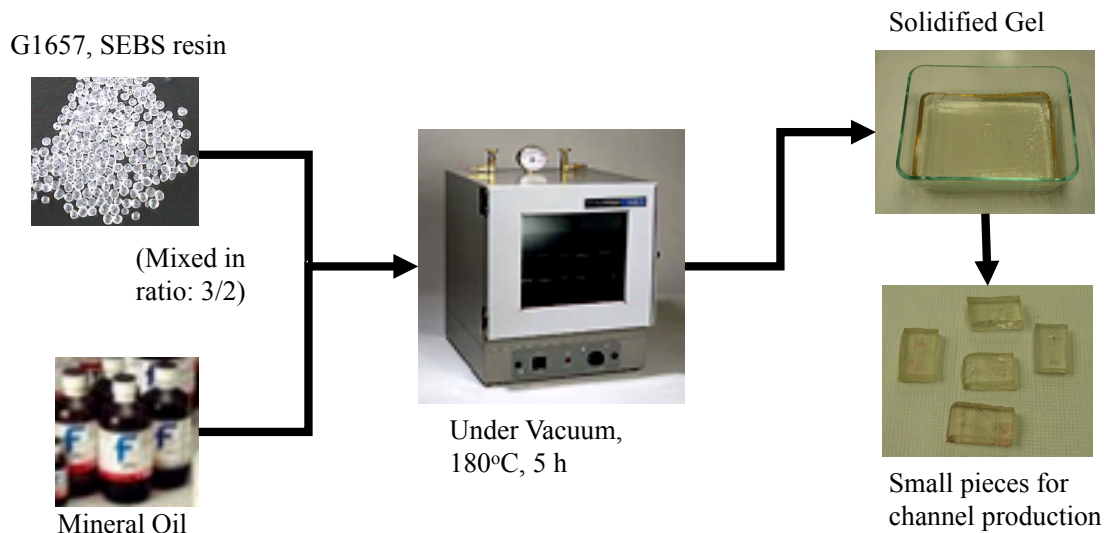


Figure 14. Gel formation from SEBS.

Master molds incorporating the Y shaped design were fabricated using printed circuit boards (Figure 15). Printed circuit boards pre-coated with a positive photoresist on 2-oz copper foil were purchased from Injectorall Electronics Corp., Bohemia, NY. After exposing it to UV illumination through the photomask for 90 s, PC board was immersed into aqueous developer solution prepared by diluting 3.5 ml of a 50% w/w aqueous sodium hydroxide solution (SS254-4, Fisher Scientific; Hampton, NH) with 500 ml of deionized (DI) water. After developing and rinsing, a solution prepared by dissolving 150 g of ammonium peroxydisulfate crystals (A682-3, certified ACS grade; Fisher Scientific; Hampton, NH) in 1 L of DI water was used to etch away the underlying copper foil in the exposed areas at a temperature of ~ 45 °C. After the remaining photoresist was stripped with acetone, the PC board was rinsed once more in DI water.

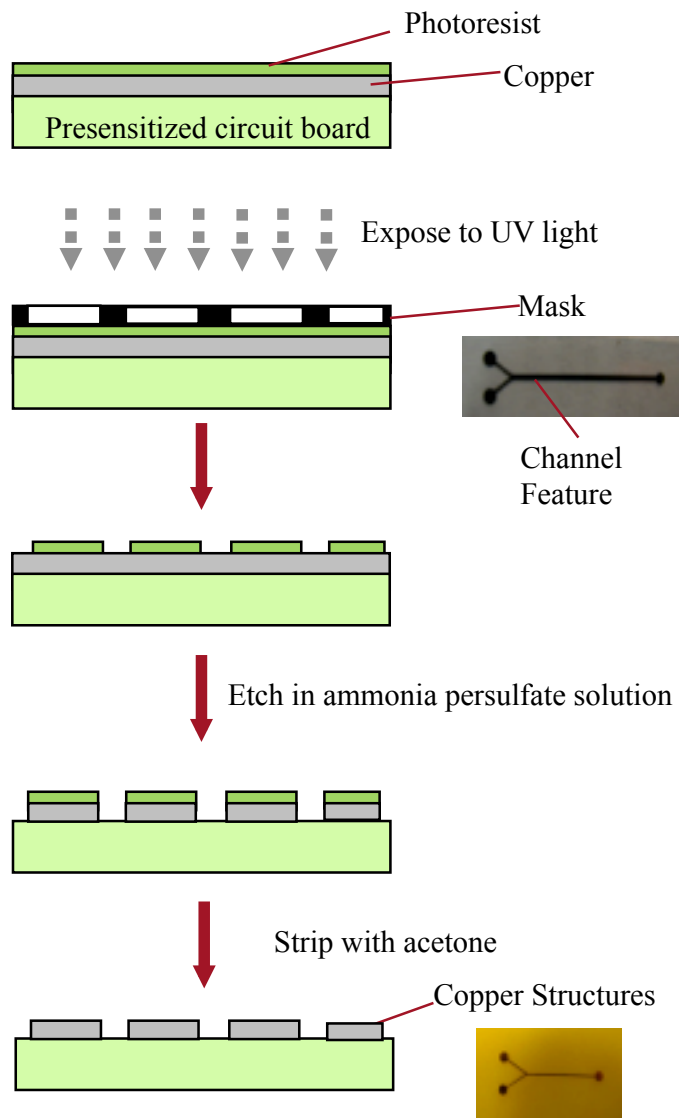


Figure 15. Fabrication of masters using printed circuit technology.

In final stage, the pattern was imprinted by placing a slab of elastomer on top of a master mold that had been preheated to 110 °C on a hot plate (Figure 16). Within seconds, the elastomer begins to soften and can be gently pressed down by hand for several seconds to make uniform contact with the structures on the mold. After cooling and release, the solidified gel precisely replicates the shape of the structures on the master.

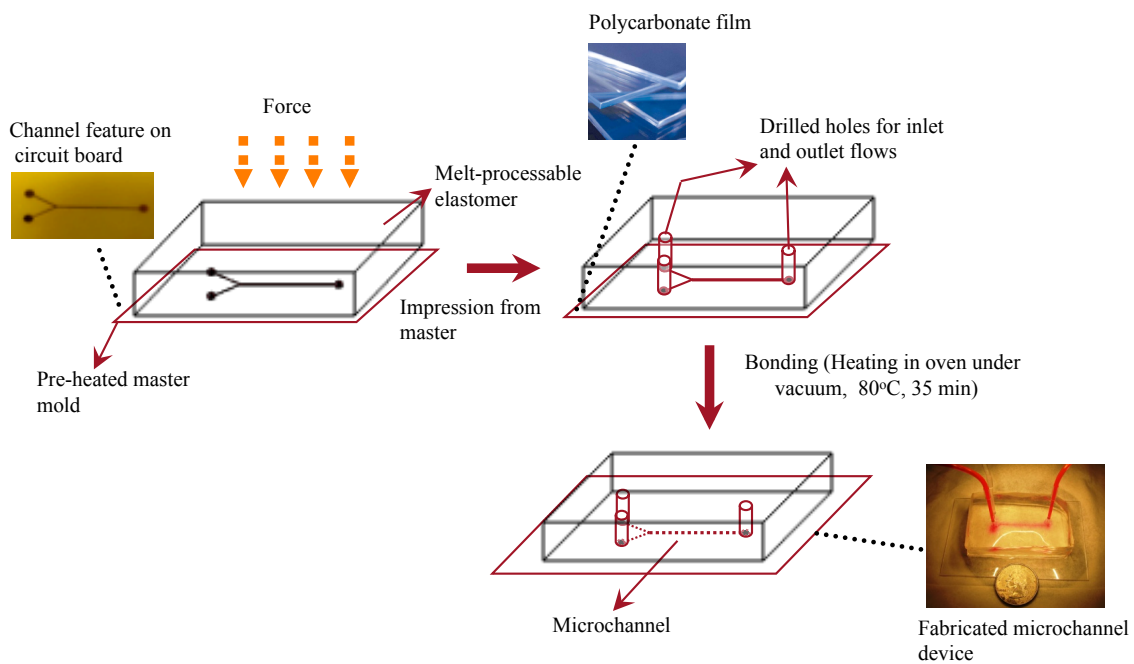


Figure 16. The finalizing steps in production of thermoplastic elastomer channel.

Fluidic access holes were made using a heated needle. Finally, bonding can be achieved with polycarbonate surface (1 mm thick film) by briefly heating the channel material at the bond interface to a temperature just below its softening point using a hot plate or oven (80°C, 35 min). This fabrication approach allows a static or low-pressure microfluidic network to be constructed, but the bond can be removed by peeling off the elastomer microchannel.

3.4 Flow Visualization and Data Analysis

Confocal Microscopy

The confocal fluorescence imaging apparatus employed to visualize tracer diffusion consisted of a confocal scanning microscope (Axiovert 200M MAT equipped with a LSM 5 Pascal confocal module (Carl Zeiss MicroImaging, Inc., Thornwood, NY)) with a Zeiss Plan-Neofluar 10x / 0.3 numerical aperture objective (Figure 17).



Figure 17. Top view imaging using Zeiss LSM 5 Pascal confocal microscope.

Images were recorded at multiple downstream locations from the microchannel inlet and analyzed using Zeiss LSM 5 software (Release 3.2). The laser module consists

of an argon laser (30 mW, 458/488/514 nm) and two helium-neon lasers (1 mW, 543 nm and 5 mW, 633 nm).

a) Dye diffusion experiments

Fluorescein fluorescence was excited using an argon laser with a 488 nm HFT dichroic beam splitter, and monitored using a 505 nm long pass emission filter. On the other hand, HeNe laser with a 543 nm HFT dichroic beam splitter and a 560 nm long pass emission filter was used for Rose Bengal fluorescence. Eight-bit images (512×512 pixels) were collected with a scan speed of 9 (1.6 μs pixel time), scan zoom 1, and a pinhole of ~ 1 Airy unit for optimum depth resolution (66.6 μm pinhole diameter and optical slice thickness $< 10.9 \mu\text{m}$). The specified interval thickness (step width: z distance between the individual xy images) and the number of slices (number of sections: individual xy images) were chosen as 0.05 μm and 1,200, respectively, to provide a 60 μm deep image stack that would fully bracket the 50 μm microchannel height. After data acquisition, the image corresponding to the midplane was selected by manually locating the floor and ceiling of the microchannel within the image stack as reference points. Only a single midplane image was used (i.e., no depth averaging was performed). Our analysis was restricted to the midplane image in order to minimize the influence of sidewall effects on the resulting diffusivity measurements.

The lateral dye spreading distance was measured with respect to the microchannel wall at 4 mm downstream increments over the entire length. These values were then subtracted from the measured centerline distance at the inlet to obtain values

of w at each point. The plotted data are averages of three different measurements obtained at 5 min intervals (error bars represent the standard deviation).

b) Microfluidic stability probe experiments

Interfacial aggregation studies were carried out by imaging parallel co-flowing streams containing dye and suspended nanoparticles, respectively, using the same Confocal Scanning Microscope system interfaced with Canon PowerShot 640 digital camera (4x zoom). During imaging, a halogen lamp (3.8 V) was used as a light source in transmitted light mode with BF filter and condenser aperture was adjusted to 0.6706. Images were recorded at multiple downstream locations from the microchannel inlet and assembled into a composite picture using Adobe Photoshop. The downstream location x^* corresponding to the onset of instability in the aggregation pattern (see the figure on Page 82) was chosen to be the point where the interfacial aggregation line began to exceed $38 \mu\text{m}$ in width.

Scanning Electron Microscopy (SEM)

After disassembly of thermoplastic elastomer channel, the flat polycarbonate film containing the deposited aggregates was dried at room temperature in an enclosed container, coated with a thin gold-palladium layer (500 \AA) using a Hummer II sputter coater (Anatech), and subsequently was observed with a scanning electron microscopy (JEOL JSM-6400) at an accelerating voltage of 15 keV and 15 mm working distance. The JSM-6400 is equipped with a Princeton Gamma-Tech (PGT) EDS System. The chemical composition was evaluated using this high-energy dispersive X-ray spectroscopy.

3.5 Thermal Conductivity Measurements

KD2 Pro Thermal Property Analyzer

Thermal conductivity measurements were performed using a thermal property analyzer (Model KD2 Pro, Decagon Devices, Inc., Pullman, WA). This device is widely and conveniently used in measuring thermal conductivities of liquids, solids and nanofluids.^{76, 89, 119-121} It operates based on the transient hot wire method and is capable of measuring conductivities in the range from 0.02 to 2.00 W/mK with an accuracy of $\pm 5\%$ or 0.01 W/mK over a span of 0 to 50 °C (Figure 18). It consists of sensor needle that contains both a heating element and a thermal resistor and a microprocessor for controlling and conducting the measurements.



Figure 18. KD2 Pro thermal property analyzer (Decagon Devices, Inc., Pullman, WA).

This instrument measures thermal conductivity by applying a parameter-corrected version of the transient temperature model of Carslaw and Jaeger for an

infinite line heat source with constant heat output in a homogeneous, isotropic and infinite medium.¹²² The temperature response during heating can be defined as

$$\Delta T = T - T_0 = \frac{-q}{4\pi k} Ei\left(\frac{-r^2}{4D_{th}t}\right) \quad 0 < t < t_1 \quad (12)$$

where q is the heat dissipated per unit length (W/m), k is the thermal conductivity (W/mK), r is the radial distance from the heat source (m), D_{th} is the thermal diffusivity (m^2/s), t_1 is the heating time (s), and Ei is the exponential integral. The temperature rise after the heat is turned off can be expressed as

$$\Delta T = T - T_0 = \frac{-q}{4\pi k} \left[Ei\left(\frac{-r^2}{4D_{th}t}\right) + Ei\left(\frac{-r^2}{4D_{th}(t-t_1)}\right) \right] \quad t > t_1 \quad (13)$$

Thermal properties of materials are found by fitting the time series temperature data during heating to equation 12 and cooling to equation 13. The solutions for a heated cylindrical source with nonnegligible radius and finite length were given by Kluitenberg et al.¹²³ Both aforementioned models fit the data but give slightly different values for fitting parameters. Through careful calibration of the probe, these differences are taken into account, and simpler Carslaw and Jaeger model can be reliably used. The algorithm for the method is integrated within the instrument itself, thermal conductivity of the sample and correlation coefficient of the measurement are directly displayed on the screen of the instrument.

Water and refrigerant are low viscosity liquids so the read time was set to the minimum allowed time (1 min) for the measurements done with stainless steel KS-1

probe to avoid excessive heating which can cause errors from free convection. Each 90 s measurement cycle consisted of an initial 30 s temperature equilibration stage, followed by 30s of heating and 30 s of cooling. The temperature versus time response during full time (1 min) was recorded at 1 s intervals, and the data was fit by applying equations (12) and (13) to obtain the suspension thermal conductivity. The probe response is calibrated to account for finite length and diameter effects. Our probe was calibrated using glycerin and water standards, and consistently yielded results in good agreement with literature.¹⁰⁸ All the measurements were taken on an optical table, and the isothermal bath was even switched off during the measurements to eliminate vibration effects. The probe (KS-1, 60 mm long by 1.3 mm diameter) was oriented vertically to minimize free convection of the fluids. It is observed that measurements are very sensitive to time needed for probe and solution to come to equilibrium. The experimental description specific to suspension type is given below:

a) Measurements of aqueous suspensions with KD2 Pro

Alumina suspensions were prepared in larger quantities (180 ml) both with and without dye following the procedures described previously. Fluid samples were placed in a glass beaker (5.6 cm i.d. by 8.5 cm length) and immersed in an isothermal bath (*Lauda Model RE106, LAUDA-Brinkmann, LP Delran, NJ*) at 22.3 °C. The free surface of the fluid sample was covered by a layer of light mineral oil (Cat. No. BP2629-1; Fisher Scientific, Fair Lawn, NJ) to reduce surface tension effect on probe contact.

b) Measurements of refrigerant suspensions with KD2 Pro

To avoid evaporation of refrigerant, the suspensions (300 ml) were put in a special glass jar with open-top polypropylene screw caps bonded with Teflon/silicone septa (250 ml, Cat. No. S121-0250, I-Chem, Rockwood, TN). Free convection of the fluids were tried to be minimized by forming a hole in the middle of septa through which thermal meter probe (KS-1) was inserted vertically and centrally into the suspension without touching the side walls of the jar. Hydrofluoroether (HFE) fluids display low surface tensions and contact angles on most surfaces, thereby can be classified as the highly wetting liquids.¹²⁴ There has been no wetting problem reported about the KS-1 probe so far. The detail of wire-liquid interface and its corresponding effect on measured thermal conductivities is beyond of our scope. The sample temperature was controlled by fully immersing each jar in a circulating water bath (*Lauda Model RE106, LAUDA-Brinkmann, Delran, NJ*) and allowed to equilibrate at the measurement temperature for at least 20 min.

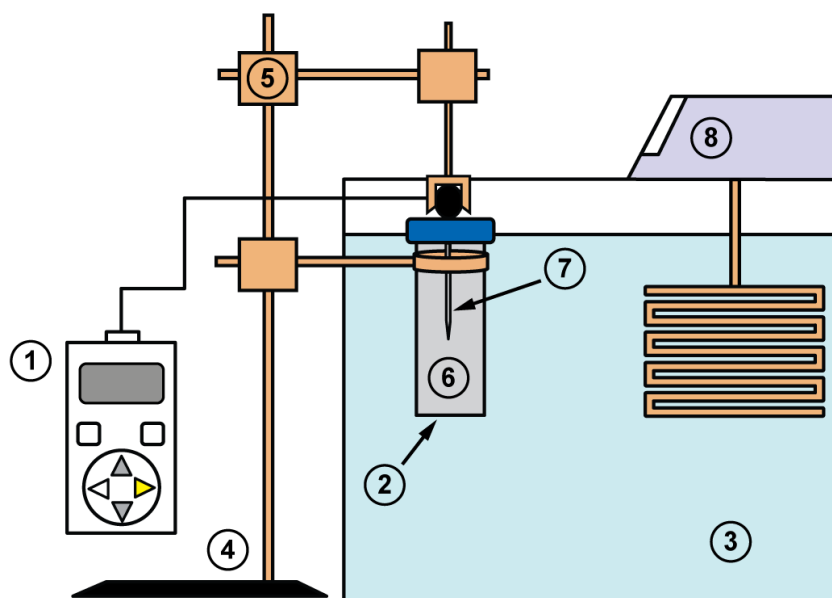


Figure 19. A standardized thermal conductivity measurement protocol for nanorefrigerants. The apparatus employs commercially available components to create a standard platform that can be easily assembled in any laboratory. Shown are (1) KD2-Pro thermal conductivity meter, (2) glass jar with septum in cap, (3) circulating water bath, (4) support stand, (5) clamps, (6) nanofluid sample, (7) KS-1 probe needle, and (8) bath temperature controller. Drawing is not to scale.

Thermal conductivities of refrigerant suspensions were measured at temperatures of 2°C, 12°C and 22°C using the experimental set-up given in Figure 19. The plotted data are averages of three independent measurements (at least 20 min elapsed between each measurement; error bars represent the standard deviation). Adherence to this protocol enabled us to obtain highly reproducible thermal conductivity measurements in refrigerant-based nanosuspensions. Measurement variability was greatly reduced by performing a complete series of experiments in a single session. For example, a typical series of experiments included measurements on control samples of the pure refrigerant and refrigerant-surfactant mixture, in addition to the dispersions of interest. All conductivity data reported here are therefore normalized by the pure refrigerant values

acquired during the same measurement session to minimize systematic variations between experiments performed at different times.

3.6 Viscosity Measurements

The viscosities of the aqueous alumina suspensions (~ 0.5 ml sample volume) were measured over a wide range of shear rate using a Physica MCR 300 Modular Compact Rheometer from Anton Paar (Ashland, VA). The measuring system geometry was a parallel-plate set-up (CP 50-1, diameter: 50 mm, gap width: 0.05 mm, angle: 0.987 (Cat No: 79040, Anton Paar)). After programming the instrument for set temperature and equilibration, samples were subjected to two-cycle shear in which the shear rate was increased from 10 to 500 s⁻¹ and immediately decreased from 500 to 10 s⁻¹ without a pause between up (forward) and down (backward) ramps. All rheological tests were done in triplicate at room temperature (~22°C). The temperature was controlled using a water bath (*Lauda Model RE106, LAUDA-Brinkmann, LP Delran, NJ*) with a circulation pump.

Similarly, the steady shear viscosities of our refrigerant suspensions containing graphene nanosheets, carbon nanotube, and metal oxide and nitride were also measured using the same procedure at specified temperatures (2 °C, 12 °C and 22 °C). A solvent trap was applied during measurements to minimize evaporation. All measurements were repeated at least 3 times.

4. INTERFACIAL COMPLEXATION EXPLAINS ANOMALOUS DIFFUSION IN NANOFLUIDS*

4.1 Introduction

Colloidal nanomaterials become key ingredients in an incredibly diverse array of applications, including paints, ceramics, drug delivery, and food processing.¹²⁵⁻¹²⁸ A particular class of suspensions (so-called *nanofluids*¹²⁹) are currently a focus of considerable attention owing to reports of unusual physical phenomena,^{14, 130} most notably dramatically increased thermal conductivity and critical heat flux relative to the particle-free fluid.^{59, 131-135} In addition to augmented thermal properties, interest in nanofluids has been further excited by reports of equally dramatic enhancements in mass transport. Specifically, a group of researchers has recently described observations of a 14-fold increase in fluorescein diffusivity when the dye was dispersed in a 0.5 vol% aqueous suspension of 20 nm diameter Al₂O₃ nanoparticles.³¹ Great interest was sparked by this result, but conflicting claims regarding whether or not mass diffusion enhancement is promoted in nanofluids have been made.^{34, 36, 37} In an effort to address the critical need for understanding mass transport in nanofluids, a microfluidic system where transverse transport of tracer dye between co-flowing streams is directly

*Reprinted with permission from “Interfacial complexation explains anomalous diffusion in nanofluids” by S. Ozturk, Y.A. Hassan, V.M. Ugaz, 2010. Nano Letters, 10(2), 665-671, Copyright 2010 by American Chemical Society.

monitored is proposed. The diffusion phenomena is first investigated by mimicking the conditions used in KBPP experiments, and then alternative tracer dye-surfactant-nanoparticle systems.

4.2 Microfluidic Approach

Microscale conditions in channel induce laminar flow (very low Reynolds number due to small channel diameter and low flow rate). During diffusion of species between streams, the rate of the growing interface thickness with downstream distance can be described by a 1-D diffusion model $\partial c/\partial t = D \partial^2 c/\partial y^2$, where c is the concentration of the species of interest, D is its diffusion coefficient, t is the diffusion time, and y is the lateral position (Figure 20). If the lateral concentration profile within the interfacial zone is assumed to be Gaussian with variance σ , its effective width can be expressed as 4σ , and its rate of growth in time follows $\sigma^2 = 2Dt$. In many of our experiments, however, the lateral intensity profile can be distorted due to the anomalous fluorescence effects described in the following sections. To circumvent this issue, lateral diffusion of the tracer dye in stream I is characterized by recording the growth of the fluorescence intensity profile width ($w_i \approx \sigma_i$) from the centerline (CL) into stream II in order to obtain a measurement approximately equal to one fourth the width of an equivalent Gaussian zone (Figure 20).

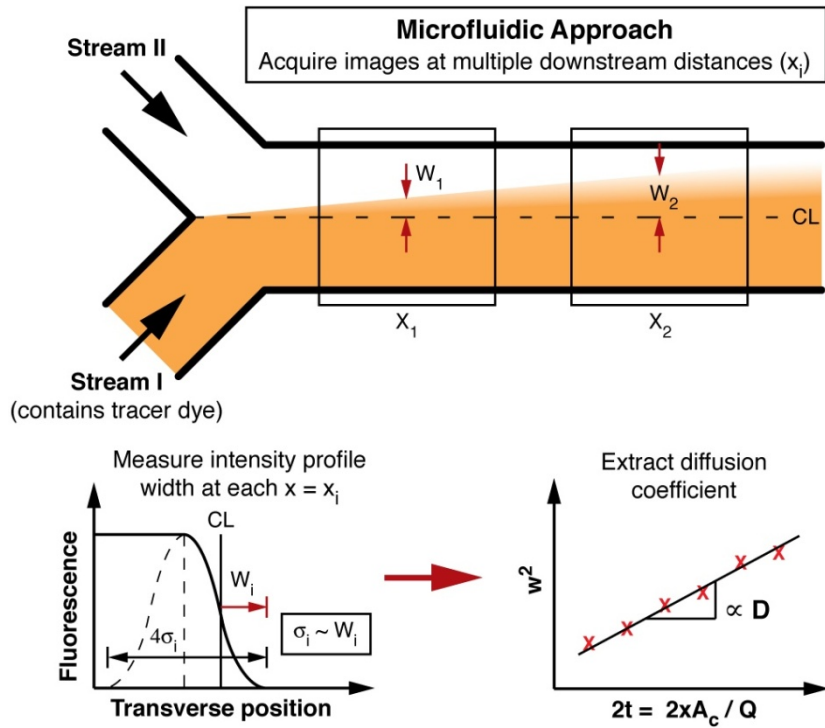


Figure 20. Microfluidic approach for measuring tracer diffusion in nanoparticle suspensions. Parallel fluid streams are introduced into a microchannel under laminar flow conditions. Lateral diffusion of the tracer dye in stream I is characterized by recording the growth of the fluorescence intensity profile width ($w_i \approx \sigma_i$) from the centerline (CL) into stream II. Measurements acquired along the microchannel midplane (i.e., halfway between the floor and ceiling) at multiple downstream locations from the inlet (x_i) are then converted to units of time, yielding a linear increase in w^2 whose slope is proportional to the diffusion coefficient.

A confocal microscope was used to acquire images along the midplane of the microchannel in order to eliminate artifacts due to sidewall effects. Additionally, the diffusion time was expressed in terms of the distance x from the inlet to a downstream measurement point by $t = xA_c/Q$, where A_c is the channel cross-sectional area, and Q is the volumetric flow rate. In this way, measurements of the interfacial zone width acquired at multiple downstream locations can be assembled to construct a plot of w^2

versus $2t = 2xA_C/Q$. These data are expected to follow a linear trend whose slope yields the value of D .

On the other hand, the experiment conditions reported by KBPP was first examined.³¹ In their experiments, a dip pin was used to deposit a small drop of aqueous fluorescein dye solution into a well (4 mm dia., 2 mm tall) containing a quiescent Al_2O_3 nanoparticle solution stabilized with the surfactant Tween-80 (Figure 21).

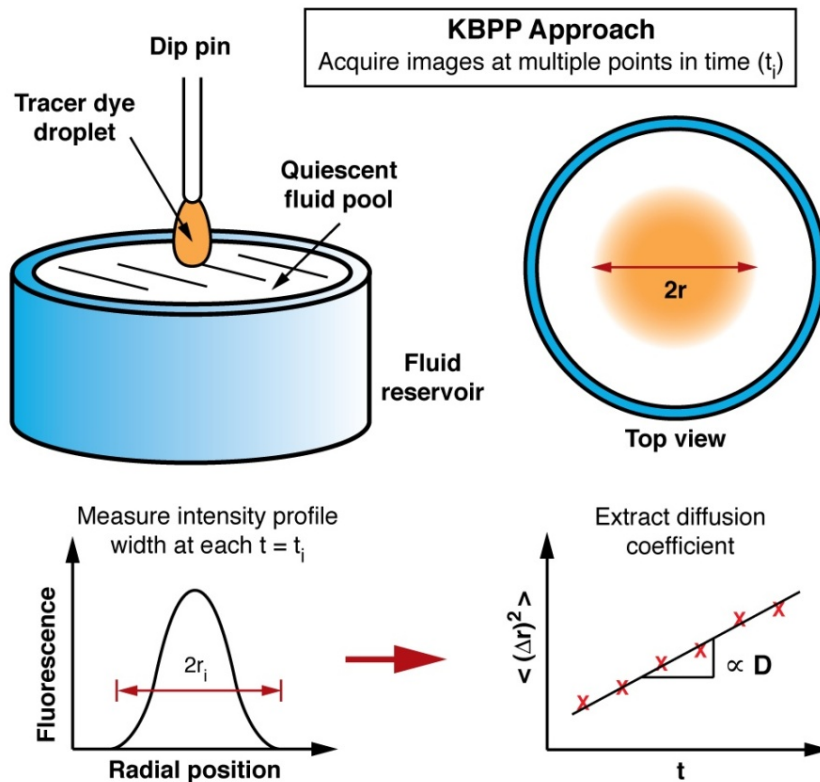


Figure 21. In the approach used by KBPP,³¹ a drop of tracer dye is introduced into a quiescent pool (4 mm dia., 2 mm tall) containing a nanoparticle suspension. The radial spreading of dye fluorescence (r_i) is recorded by acquiring images at multiple points in time (t_i), yielding a linear increase in $\langle (\Delta r)^2 \rangle$ whose slope is proportional to the diffusion coefficient.

The dye fluorescence was then monitored as a function of time as it spread into the surrounding nanoparticle solution, and analysis of the fluorescent zone's growth yielded a measure of tracer diffusivity. The radial spreading of dye fluorescence (r_i) into the surrounding nanoparticle solution is recorded by acquiring images at multiple points in time (t_i), yielding a linear increase in $\langle(\Delta r)^2\rangle$ whose slope is proportional to the diffusion coefficient of tracer dye.

4.3 Fluorescein Diffusion in Alumina Nanoparticle Suspensions

A microfluidic analog of this KBPP experiment system was first devised by co-injecting streams containing the aqueous fluorescein dye solution (stream I) and the nanoparticle suspension (stream II), and subsequently monitoring the transverse spreading of fluorescence between streams. But instead of the anticipated continuous decay in fluorescence from stream I to stream II, spontaneous formation of a highly focused and intensely fluorescent plume at the interface accompanied by an adjacent zone of depleted fluorescence in the dye stream was observed (Figure 22 and 23).

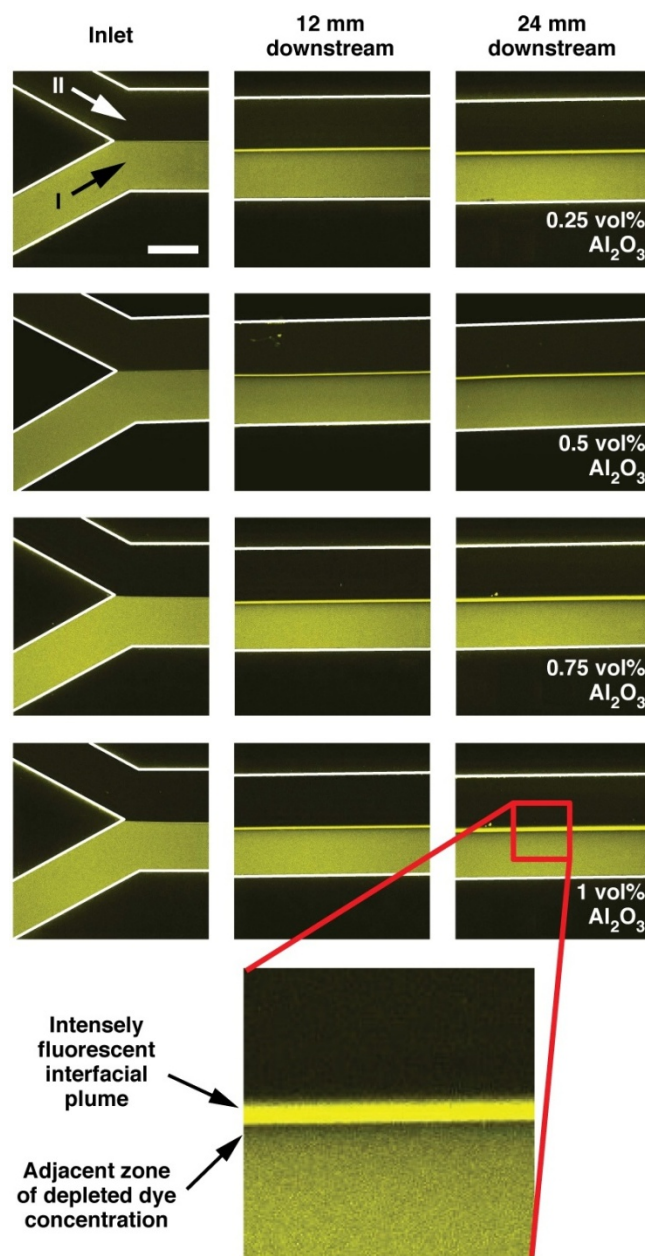


Figure 22. The KBPP experiment conditions are mimicked by introducing co-flowing streams consisting of an aqueous fluorescein solution (stream I) and an aqueous Al_2O_3 nanoparticle suspension (stream II) into a microchannel at a flow rate of 0.05 ml/min. Fluorescence images are shown at the inlet and locations 12 and 24 mm downstream (scale bar 250 μm). Complexation between the dye and nanoparticles becomes vividly evident by formation of an intensely fluorescent plume at the interface between streams, accompanied by a depletion region of reduced fluorescence in the immediately adjacent dye. The fluorescent plume becomes prominent with increasing alumina concentration to 1 vol%. All nanoparticle suspensions contained 5.35 mg/ml Tween-80 (tracer dye solutions contained no surfactant).

The breadth of the anomalous fluorescent zone grew with increasing nanoparticle concentration and with decreasing flow rate (i.e., corresponding to a longer fluid residence time within the microchannel). In order to mimic the KBPP studies as closely as possible, the microfluidic experiments shown in Figure 22 and 23 were performed under conditions where the formulation of the aqueous dye solution was different from that of the nanoparticle suspension (i.e., neither surfactant nor nanoparticles were present in the tracer dye stream).

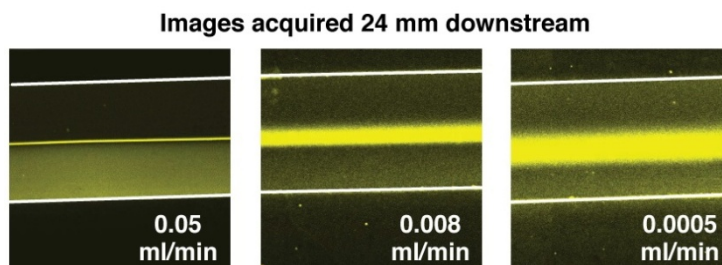


Figure 23. The fluorescent plume becomes more prominent with decreasing flow rate, corresponding to increasing fluid residence time within the microchannel (0.5 vol% Al_2O_3 , all other experiment conditions identical to Figure 22). All nanoparticle suspensions contained 5.35 mg/ml Tween-80 (tracer dye solutions contained no surfactant).

A more rigorous approach, however, would be to ensure that the composition of the tracer solution is identical to that of the adjacent fluid, aside from the presence of the fluorescent dye. This methodology was adopted in a new set of experiments using streams containing subsets of the individual components present in the system (nanoparticles, surfactant, dye, and methanol (added to enhance dye solubility)) to better understand their influence on the diffusion measurements (Figure 24a).

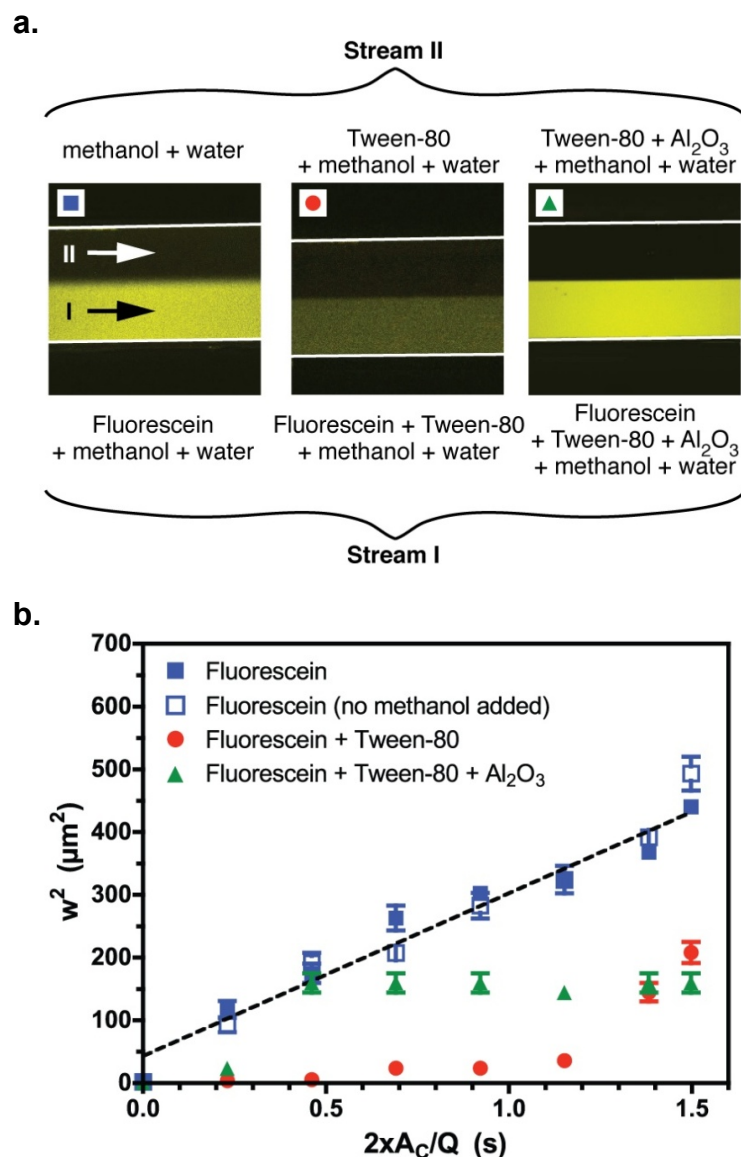


Figure 24. (a) The fluorescent plumes disappear when identical fluid compositions are used in streams I and II with the only exception being addition of the tracer dye in stream I. But lateral spreading of fluorescence becomes inhibited when surfactant and nanoparticles are added. The composition of each stream is given above and below each image, and the symbols correspond to those plotted in the graph (0.5 wt% Al₂O₃, 0.05 ml/min flow rate, images acquired 24 mm downstream from the inlet). (b) The inhibited lateral transport causes significant deviation from the expected linear increase in the square of the fluorescent zone width as a function of time, making it impossible to extract meaningful measurements of the tracer dye diffusivity in the presence of surfactant and nanoparticles. Diffusion coefficients measured in the dye solution alone (filled blue squares, dashed line shows linear regression fit to these data) agree with literature values and are not affected by addition of methanol. All nanoparticle suspensions contained 5.35 mg/ml Tween-80. A fluorescein concentration of 0.33 mg/ml was used in all experiments shown, microchannel sidewalls are highlighted by a white line.

The behavior of the aqueous dye solution alone (i.e., stream I: fluorescein solution, stream II: water) was first examined and found that it displayed the expected monotonic increase in breadth of the interfacial zone with downstream distance (Figure 24b). This validated our experimental approach, yielding a fluorescein diffusivity value ($D = 2.6 \pm 0.14 \times 10^{-6} \text{ cm}^2/\text{s}$) in good agreement with literature.¹³⁶ Addition of the surfactant Tween-80 to both streams dramatically changed the observed diffusion behavior resulting in greatly reduced (almost nonexistent) spreading of tracer dye fluorescence into the adjacent stream, ultimately to an extent that diffusivity measurements could not be extracted (Figure 24b). These observations are consistent with the formation of dye-surfactant complexes that would act to retard fluorescence diffusion owing to the larger hydrodynamic diameter of the complex relative to the dye molecules alone. Addition of nanoparticles to both streams did not produce the fluorescent plumes observed in Figure 22, but spreading of the tracer dye into the adjacent stream continued to be inhibited. This resulted in slow nonlinear growth in the breadth of the tracer dye zone, making it impossible to extract meaningful diffusivity measurements (Figure 24b). None of the data were significantly altered by addition of methanol at any of the compositions studied.

The observations in Figure 22, 23 and 24 suggest that complexation within the interfacial zone is likely to play a key role in governing these anomalous tracer diffusion effects (i.e., fluorescent plumes, impeded dye spreading). This hypothesis is supported by observations of related phenomena in microfluidic-based affinity immunoassays.¹³⁷

Figure 25 displays the images taken during diffusion of sample antigen from right side stream to left side antibody laden stream.

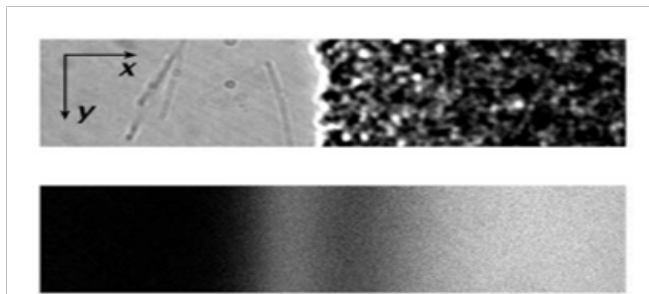


Figure 25. Phenytoin diffusion immunoassay (DIA). The image on the top is a bright field one with antibody specific for phenytoin in the left side flow stream and a 10 % blood solution spiked labeled antigen and treated with iophenoxate in the right side flow stream. Corresponding fluorescence image at the same location was also shown.¹³⁷ “Reprinted with the permission from Macmillian Publishers Ltd: Nature Biotechnology, Hatch, A.; Kamholz, A.; Hawkins, K.; Munson, M.; Schilling, E.; Weigl, B.; Yager, P., 19, (5), 461-465, Copyright 2001.”

Our system differs from the affinity binding situation, however, because the driving force is provided by adsorptive formation of dye-nanoparticle complexes. Since adsorption is generally more favorable than desorption, and since the nanoparticles (and dye-nanoparticle complexes) display a much lower diffusivity than the free tracer dye molecules, these interactions would be likely to induce stronger signatures in our system. The alumina nanoparticles display a pH dependent surface charge that renders them positively charged under the pH \sim 5 conditions of the suspensions studied here, while the fluorescein dye lacks comparable strongly charged groups and would therefore have the ability to readily adsorb onto the alumina surface.¹³⁸ Thus, the fluorescent plumes appear to reflect a situation where the rate of dye adsorption on the nanoparticles exceeds that at which new dye molecules are able to diffuse into the interfacial zone (Figure 26). Since

each nanoparticle contributes multiple adsorption sites and exhibits a greatly reduced diffusivity relative to the small molecule dye alone, a net accumulation of dye-nanoparticle complexes occurs at the interface that ultimately drives formation of a prominent zone with greatly enhanced fluorescence accompanied by an adjacent depletion zone in the dye stream.

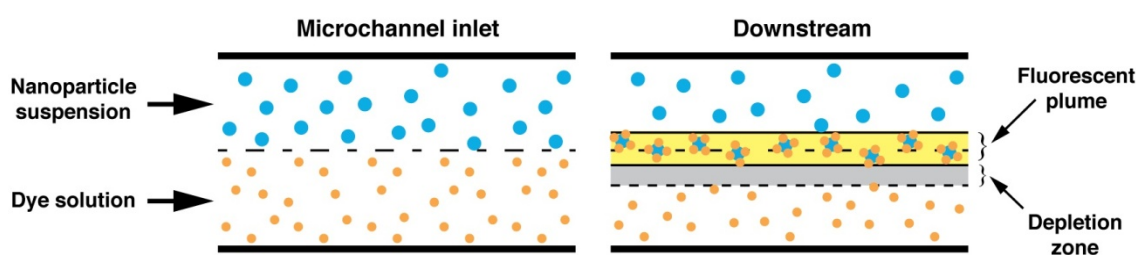


Figure 26. Interfacial fluorescent plumes arise as a consequence of complexation between the tracer dye and suspended nanoparticles. Under conditions analogous to those employed in the KBPP experiments (Figures 22 and 23) dye-nanoparticle complexes are formed more rapidly than the rate of lateral dye diffusion, resulting in formation of an interfacial fluorescent plume accompanied by an adjacent depletion zone of reduced fluorescence.

Our observations also help to explain the most unusual behavior reported in the KBPP diffusion studies.³¹ In their experiments, a drop of dye solution dispensed into pure water maintained a uniform circular profile as it diffused outward, leading to a progressive decay in fluorescence intensity with radial distance (yielding a fluorescein diffusivity value of $7.6 \times 10^{-6} \text{ cm}^2/\text{s}$, somewhat higher than our measurement). But, when an identical drop of the dye solution was placed into a nanoparticle suspension, its outward diffusion produced a much different irregularly shaped pattern characterized by intensely fluorescent thread-like regions superimposed over a nebulous background cloud of much lower intensity (Figure 27).³¹

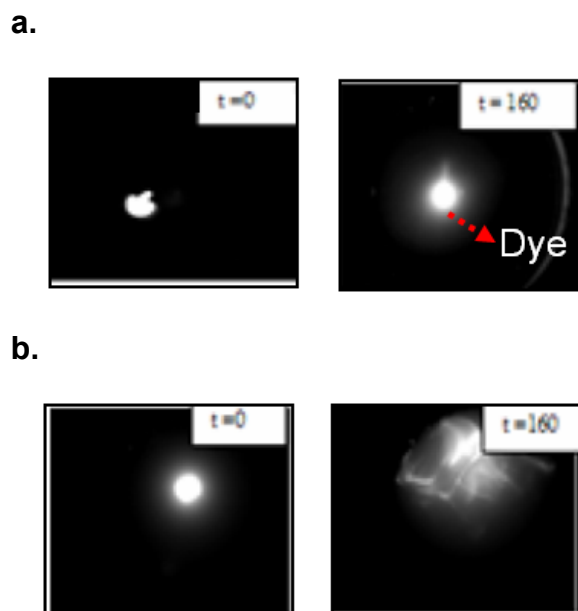


Figure 27. Fluorescein diffusion images taken at multiple points in time in (a) pure water and (b) 0.5 vol % alumina nanofluid. You can see Figure 2 and 3 in reference 31 for all images taken.³¹ “Reprinted with the permission from Krishnamurthy, S.; Bhattacharya, P.; Phelan, P. E.; Prasher, R. S. *Nano Letters* 2006, 6, (3), 419-423. Copyright 2006 American Chemical Society.”

We believe the anomalous thread-like spreading patterns reported by KBPP primarily depict flow-induced deformation of the droplet front—the same zone where highly fluorescent dye-nanoparticle complexes are localized. Since these effects introduce physical processes that are not manifestations of molecular diffusion, it is not surprising that experiments performed in this way may not accurately quantify tracer diffusivity.

4.4 Evaluation of Alternative Dye/Surfactant Combination

Our hypothesis that the anomalous diffusion behavior observed in Figure 22 and 23 reflects a balance between competing kinetics associated with dye diffusion into the interfacial zone and formation of dye-nanoparticle (and dye-surfactant) complexes

implies that accurate diffusivity measurements should be obtainable by further increasing the dye concentration. In other words, if the dye were present at a quantity greatly in excess of the available adsorption sites, it could continue spreading outward into the adjacent nanoparticle stream (Figure 28). This lateral spreading process would then correctly reflect a diffusive transport mechanism even in the presence of complexation interactions. Unfortunately, the poor solubility of fluorescein in water did not permit us to explore higher dye concentrations than the 0.33 mg/ml value used by KBPP because the resulting nanoparticle suspensions became extremely unstable, displaying rapid aggregation upon mixing with the dye.

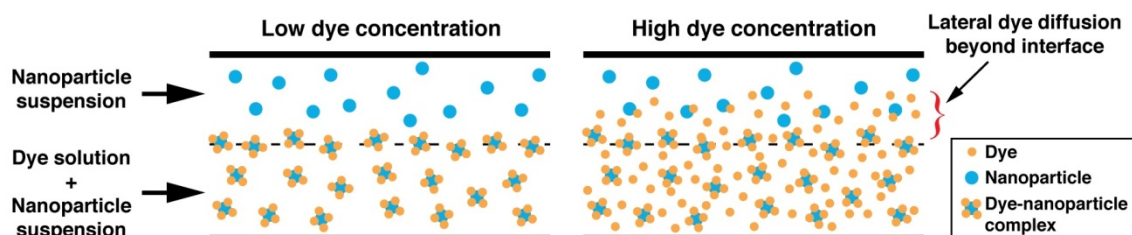


Figure 28. When nanoparticles are present in both streams, dye diffusion is inhibited at low concentrations where there are an excess of nanoparticle adsorption sites (left). Increasing the tracer dye concentration to a level exceeding that of the available adsorption sites allows lateral diffusion to progress (and be measured) even in the presence of complexation interactions (right).

We evaluated a number of alternative dye/surfactant combinations and found that a mixture containing the anionic surfactant sodium dodecyl sulfate (SDS) and the anionic dye Rose Bengal provided improved suspension stability at higher dye concentrations while minimizing complexation interactions.

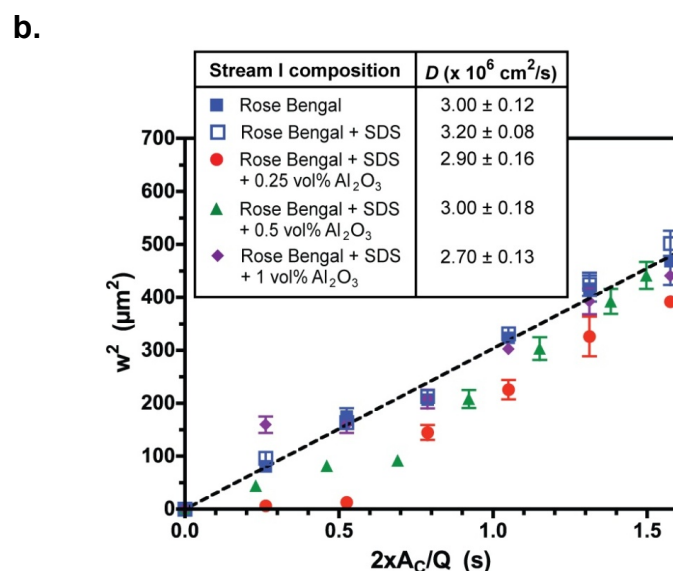
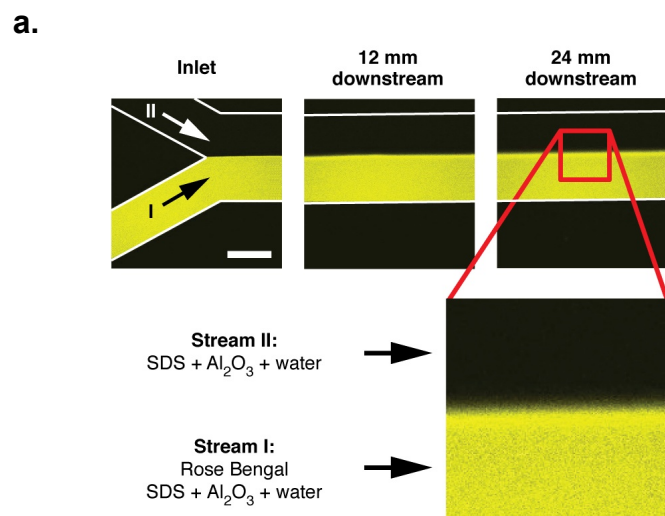


Figure 29. Tracer diffusion measurements obtained under conditions designed to account for dye-nanoparticle interactions. (a) Fluorescence images obtained using a combination of an anionic surfactant (SDS) and anionic dye (Rose Bengal) selected to enable higher dye concentrations to be used while minimizing dye-surfactant interactions (the composition of both streams is identical, except that stream I contains dye). Lateral spreading of the tracer dye is evident beyond the interfacial zone (0.5 wt% Al₂O₃, 0.05 ml/min flow rate, scale bar 250 μm , microchannel sidewalls are highlighted by a white line). (b) The observed lateral spreading follows a trend whereby the square of the zone width increases linearly with time, enabling diffusion coefficients to be quantified (dashed line shows linear regression fit to Rose Bengal data (filled blue squares)). No appreciable change in diffusivity values is observed with addition of surfactant or nanoparticles.

The like charge carried by both the dye and surfactant acts to inhibit complexation between them yielding diffusion behavior closely matching that of the aqueous dye solution alone (see Figure 29b), while the enhanced water solubility of Rose Bengal (as compared with fluorescein¹³⁹) allows much higher dye concentrations to be achieved (up to 5 mg/ml). Lateral spreading of the dye can therefore be observed regardless of whether a fluorescent plume is formed at the interface between streams because a sufficient excess of dye is present to saturate the available nanoparticle adsorption sites (Figure 29a). In contrast to the KBPP experiments, we observed that this spreading process occurs at essentially the same rate over the entire range of nanoparticle concentrations studied (Figure 29b). Furthermore, the resulting diffusivity values closely agree with those measured in the particle-free dye solution and are comparable to literature values (e.g., $4.1 \times 10^{-6} \text{ cm}^2/\text{s}$ ¹⁴⁰). Taken together, these observations point to the conclusion that tracer dye diffusion is virtually unaltered in the presence of suspended nanoparticles. The dye-nanoparticle interaction effects become more clearly evident when the diffusion process is observed under different tracer dye concentrations in a 0.5 vol% Al₂O₃ suspension (Figure 30).

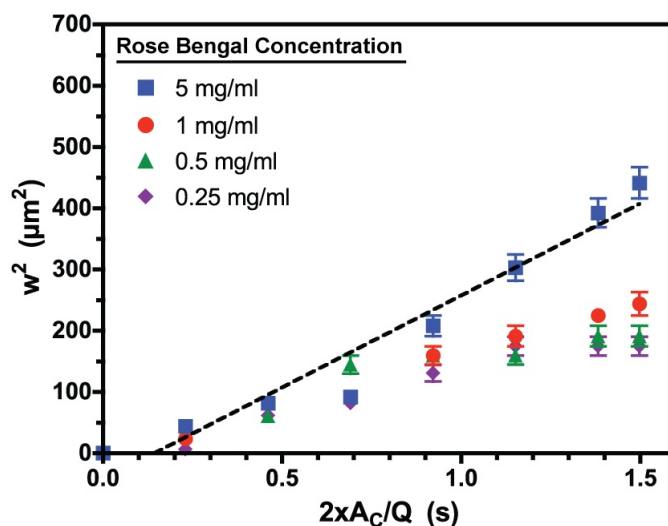


Figure 30. The effects of dye-nanoparticle interactions become evident when lateral spreading is measured as a function of dye concentration in a 0.5 wt% Al_2O_3 suspension (other conditions identical to Figure 29). The increase in the square of the fluorescent zone width deviates from the initially linear increasing trend at all, but the highest dye concentration (dashed line shows linear regression fit to 5 mg/ml data (filled blue squares)).

At low concentrations, the dye initially spreads out into the neighboring stream, but beyond a particular downstream distance the spreading ceases to progress at a measurable rate. This behavior reflects attainment of a saturation condition where the adsorption and diffusion processes reach dynamic equilibrium. Lateral spreading of the dye continues over a greater fraction of the total microchannel length as its concentration is increased, ultimately approaching behavior observed in the particle-free fluid. These data confirm that a Rose Bengal concentration of 5 mg/ml (more than an order of magnitude greater than the fluorescein concentration used by KBPP) is needed to overcome complexation effects that would otherwise interfere with the ability to extract meaningful and accurate measurements of tracer diffusion.

4.5 Experimental Pitfalls and Challenges Need to Be Avoided

While the microfluidic format offers a useful tool to perform tracer diffusion studies, several important factors must be considered when devising experiments to ensure that the results are interpreted correctly. First, the use of confocal microscopy to probe phenomena locally at the microchannel midplane (i.e., halfway between the floor and ceiling) is crucial. Monitoring diffusive transport at this image plane is necessary because the reduced flow velocity in the near-wall region can produce nonuniform tracer concentration profiles due to corresponding differences in residence time near the sidewalls relative to the center of the microchannel. Consequently, if the spreading of dye fluorescence were characterized by simply observing the microchannel from above, it would not be possible to decouple the contribution of these near-wall effects, resulting in overestimation of diffusion coefficients (i.e., the “butterfly effect”).¹⁴¹⁻¹⁴⁴ Second, a high aspect ratio microchannel cross-section is desirable to generate a uniform velocity profile in the vicinity of the centerline¹⁴⁵ where observations of the diffusion process are acquired (an aspect ratio of 10 was employed here; 50 μm tall \times 500 μm wide). Third, surface adsorption under the inherently high surface-to-volume conditions in microchannels may also potentially influence tracer diffusion. In our experiments, these effects are again minimized by using confocal microscopy to localize our observations along the microchannel midplane. Adsorption of SDS at PDMS surfaces has been previously explored,¹⁴⁶⁻¹⁴⁸ but these studies are generally performed in the context of investigating electroosmotic flow phenomena and therefore involve surfactant concentrations much lower than those we employ to stabilize our nanoparticle

suspensions. The tracer dye is also present at high concentration, and even if surface adsorption were significant it would only act to counter the abovementioned butterfly effect. In terms of the nanoparticles, their relatively low diffusivity (with respect to the dye) would likely limit the ability of sidewall adsorption effects to significantly alter particle concentrations at the midplane during the limited residence time within the microchannel. Our X-ray Photoelectron Spectroscopy measurements did not show any adsorption of alumina nanoparticles on the surface of PDMS samples (APPENDIX A). These considerations give us confidence that our results provide a true reflection of tracer diffusion.

5. A SIMPLE MICROFLUIDIC PROBE OF NANOPARTICLE SUSPENSION

STABILITY*

5.1 Introduction

In addition to fundamental studies, it is often of interest to characterize heat and mass transport during flow (e.g., to explore convective heat transfer and boiling phenomena) with application of passive tracers for visualization of flow field.^{40, 149, 150} Particle image velocimetry (PIV) is a whole field non-invasive method to interrogate the 3D velocity field using micron size seed particles. While these tracer-based PIV methods are well-established, their applicability to nanoparticle suspensions is not as straightforward because of potential interactions between the seed particles for PIV and the suspended nanoparticles. One potential way to overcome these problems involves the use of a molecular tagging velocimetry (MTV) approach, whereby spatially distinct zones of a fluorescent dye solution are illuminated with a pulse of light. The displacement of these zones is then recorded with high-speed imaging as the fluorescence decays and used to extract quantitative velocity information in the same way as is done with PIV, except that tracer particles are replaced with the fluorescent zones.⁴⁵

* Reprinted with permission from “A simple microfluidic probe of nanoparticle suspension stability” by S. Ozturk, Y.A. Hassan, V.M. Ugaz, 2012. *Lab on a Chip*, 12, 3467-3473, Copyright 2012 by The Royal Society of Chemistry.

Tracer dyes can also be used to obtain simultaneous non-invasive temperature measurements in the flow by computing the time constant associated with the fluorescence decay curve.^{46, 47} Moreover, dyes are commonly used as tracers to study flow characteristics, diffusion, and in many processes such as micro and macro scale mixing.⁴⁸⁻⁵¹ But application of tracer dyes in nanofluid flow studies needs to be carefully monitored due to possible interactions existing among suspension components. Failure to consider these effects can lead to incorrect interpretations about transport phenomena observed in tracer-based studies, as is evident by conflicting claims regarding whether or not mass diffusion enhancement is promoted in nanofluids.^{31, 34, 35 63 36, 37 38} Here the feasibility and important aspects of dye applications into colloidal systems as a tracer are investigated. The fluorescent dyes (rhodamine 6G (Rh 6G) and Rose Bengal (RB)) were preferred instead of non-fluorescent ones because they are most practical and convenient tracers that can be detected at even very low concentrations. Using a microfluidic approach in understanding the complex interactions in colloidal system components, in tandem with bulk characterization (zeta potential, viscosity, sedimentation behaviour, thermal conductivity etc.) of tracer dye laden alumina nanoparticle suspensions, assists to demystify the complex interactions among the ingredients of the suspensions and understand the aggregation phenomena.

5.2 Microfluidic Stability Probe

The aforementioned challenges motivated us to devise a stability test based on a simple experiment whereby two laminar streams are co-injected into a Y-shaped microchannel (Figure 31a). Under the characteristically laminar flow field within a

microchannel environment, molecular diffusion is the primary driving force for lateral species transport (i.e., perpendicular to the flow direction).^{39, 137, 141-143} First, we consider an aqueous solution containing the positively charged tracer rhodamine 6G (Stream I), and a dilute aqueous Al₂O₃ nanoparticle suspension (40 nm average particle size; NEI Corporation) stabilized with the anionic surfactant sodium dodecyl sulfate (SDS) (Stream II). The suspension immediately becomes unstable upon encountering the laterally diffusing tracer, resulting in deposition of dense nanoparticle aggregates within a narrow zone along the interface between streams.

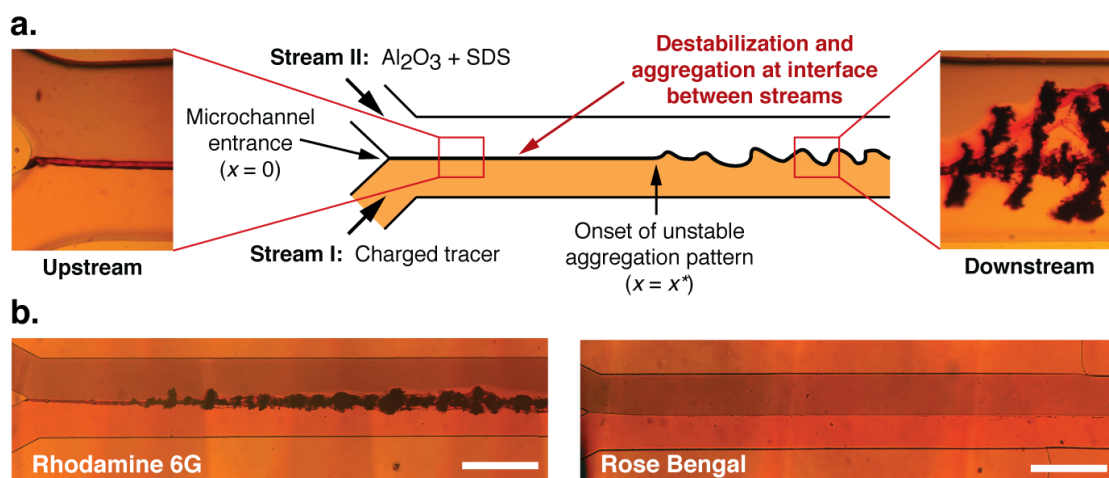


Figure 31. Exploiting interfacial destabilization in a microchannel to assess nanoparticle suspension stability. (a) Localized aggregation can occur when co-flowing streams containing an aqueous tracer solution (Stream I) and a SDS-stabilized alumina suspension (Stream II) are simultaneously injected into a microchannel, depositing zones of dense nanoparticle agglomerates along the interface between them. The aggregation patterns display morphologies ranging from well-defined lines to unstable globules beyond a downstream distance x^* . (b) Pronounced interfacial aggregation occurs in the case of rhodamine 6G, despite the fact that the suspension appears highly stable in bulk (see Figure 34). Interfacial aggregation does not occur in the case of Rose Bengal under comparable conditions. A 1 vol% alumina suspension is shown. Rhodamine 6G and Rose Bengal concentrations were 0.5 and 5 mg/ml, respectively; the SDS concentration was 15 mg/ml, the flow rate was 0.05 ml/min. Scale bars, 500 μ m.

The compositional analysis of SEM data confirms the presence of alumina in the deposited aggregates (Figure 32). The micrographs depict the morphology of the deposited aggregates, and elemental analysis confirms that they are composed of alumina nanoparticles. The width of the deposited pattern is governed by the flow rate and relative composition within each stream, permitting assembly of the resulting aggregates into morphologies ranging from thin lines to disordered globules. In contrast, however, the same tendency toward pronounced destabilization is not observed under comparable conditions when rhodamine 6G was replaced by the negatively charged tracer Rose Bengal (Figure 31b). Instead, no formation or deposition of aggregates is evident along the entire length of the microchannel.

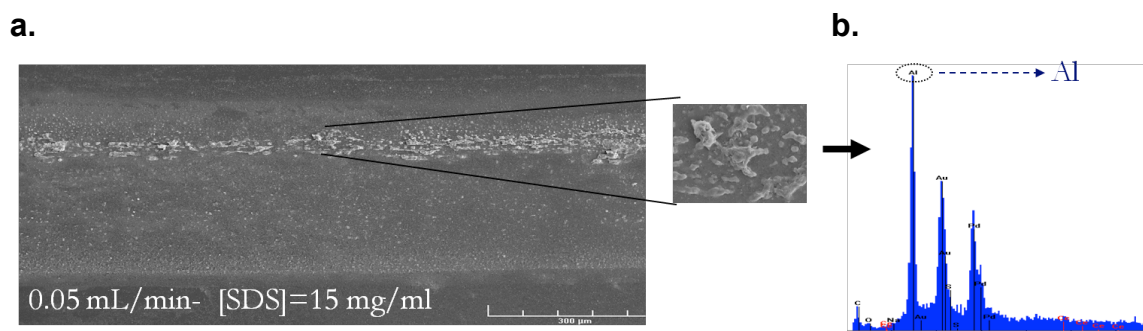


Figure 32. (a) SEM image showing line of nanoparticle aggregates deposited on the microchannel floor at the interface between co-flowing streams. (b) EDX analysis of the aggregation zone. The highest peak corresponds to Al.

The downstream position and lateral extent of interfacial aggregation can be manipulated by adjusting parameters governing interactions among the suspension's components. A dramatic transformation to a disordered globular morphology is triggered by either increasing the dye concentration (Figure 33a) or reducing the surfactant

concentration (Figure 33b), reflecting the accompanying enhancement in aggregation kinetics expected under these conditions. Under conditions where aggregation is confined at the interface between streams (e.g., high surfactant concentration), the thin interfacial contact zone becomes more pronounced with increasing nanoparticle concentration (Figure 33c). Increasing the flow rate delays the onset of a disordered aggregation pattern by reducing the timescale for destabilizing interactions to occur (Figure 33d). Although fundamental interactions among individual components in the suspension are difficult to elucidate from these observations alone, some insight into this interplay can be qualitatively obtained by examining the downstream distance x^* from the microchannel entrance to the location where the interfacial aggregation pattern becomes unstable. A characteristic aggregation timescale $t_{agg} = x^*/U$ can then be defined, where $U = Q/A_C$ is the average flow velocity, Q is the volume flow rate, and A_C is the microchannel's cross-sectional area. This timescale is related to a characteristic frequency of interparticle interactions capable of overcoming a repulsive energy barrier W , expressed as $t_{agg} = (a^2/D)e^{(W/kT)} = (6\pi\eta_s a^3/k_B T)e^{(W/kT)}$, where a is the particle radius, D is its diffusivity, η_s is the solvent viscosity, T is the temperature, and k_B is Boltzmann's constant.¹⁵¹ This scaling is reflected in the fact that these data roughly superimpose on a semi-log scale plot when normalized with respect to the residence time in the microchannel, $t_{res} = L/U$ where L is the length from inlet to outlet (Figure 33e; SDS concentrations at the low end of the extremes shown in the images of Figure 33d were examined because x^* is most reproducibly measured under these conditions).

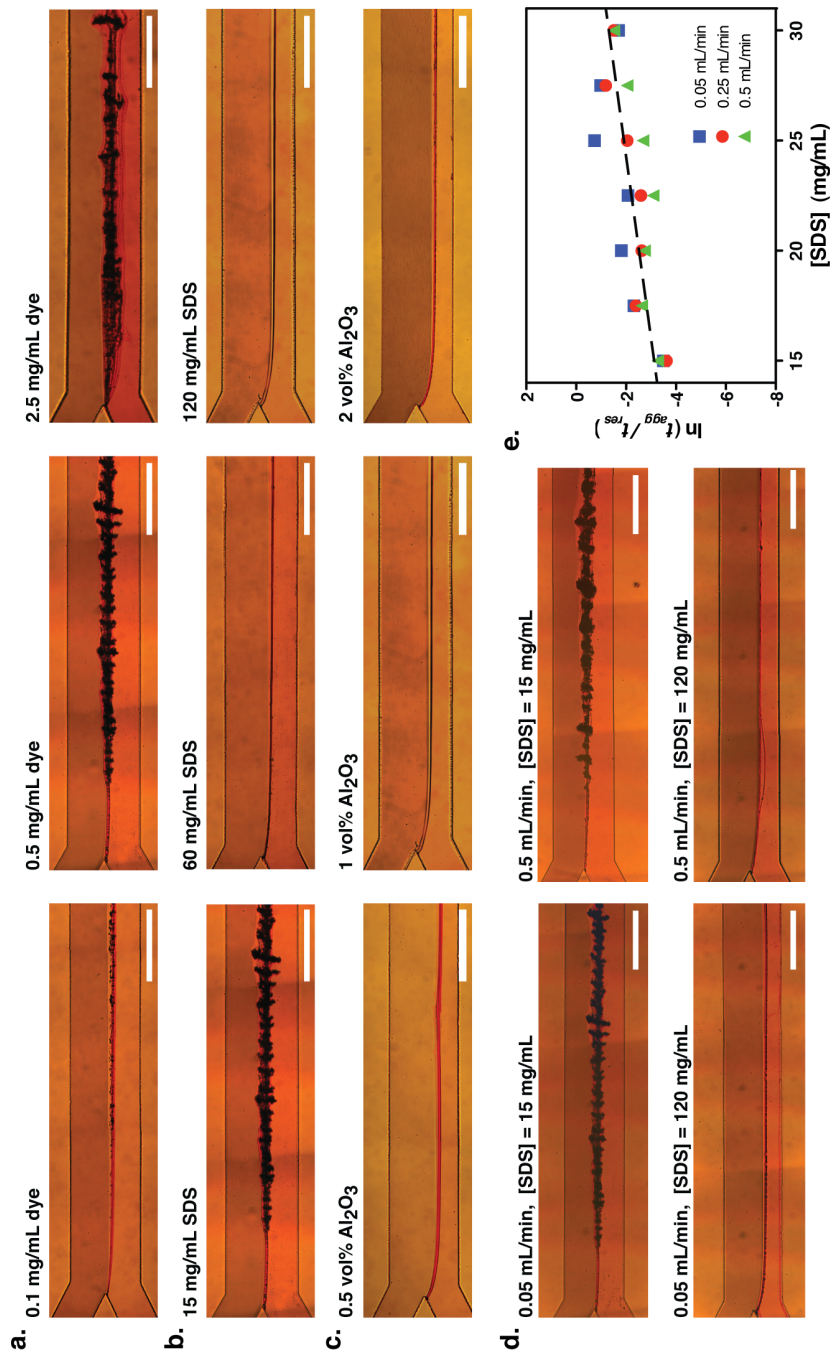


Figure 33. The position and morphology of interfacial aggregation is tunable by adjusting the suspension composition and flow rate. (a) Effect of rhodamine 6G concentration (1 vol% alumina, 15 mg/ml SDS, 0.05 ml/min). (b) Effect of surfactant concentration (1 vol% alumina, 0.5 mg/ml rhodamine 6G, 0.05 ml/min). (c) Effect of nanoparticle concentration under conditions where a stable interfacial aggregation zone is produced (120 mg/ml SDS, 0.5 mg/ml rhodamine 6G, 0.05 ml/min). (d) Effect of flow rate (0.5 mg/ml rhodamine 6G). (e) Aggregation data from (d) display a similar trend when plotted in terms of a characteristic timescale associated with the onset of an unstable aggregation pattern t_{agg}^* normalized by the residence time t_{res} as a function of surfactant concentration and flow rate, where the SDS concentrations in the 15 – 30 mg/ml range represent conditions where x^* could be reproducibly measured (dashed line indicates linear regression fit). Scale bars, 500 μm .

5.3 Bulk Stability Characterization

Visual Sedimentation Tests

The microchannel-based experiments imply that similar trends should be observed in bulk, namely that the rhodamine 6G laden suspension should display a much greater susceptibility to aggregation than Rose Bengal. To test this hypothesis, we measured pH, zeta potential, and particle/aggregate size by dynamic light scattering (DLS) measurements for all combinations of particle, surfactant, and dye involved in our experiments (Table 5). The complete datasets of pH, DLS, and zeta potential measurements are given in APPENDIX B with the literature summary of zeta potential measurements in aqueous alumina solutions. First we examined the base suspension of Al_2O_3 nanoparticles (i.e., without added surfactant or tracer) and confirmed it to be highly stable in bulk, displaying virtually no visible sedimentation over a period of at least one week (Figure 34a) and consistent with the relatively high zeta potential ($\sim +47$ mV; hydroxyl groups on alumina nanoparticles adsorb protons yielding a positive surface charge¹⁵²). But this stability was immediately and dramatically disrupted upon addition of either tracer owing to alumina's pH dependent surface charge,¹⁵² making it necessary to introduce SDS at levels above the CMC to counteract these effects.¹⁵³⁻¹⁵⁵ Addition of SDS significantly decreased the zeta potential to -45 mV, consistent with complexation between nanoparticles and SDS with negatively charged SO^{-3} end groups (polar head groups of the surfactant are adsorbed on the positively charged alumina due to Columbic attractions).

Table 5. Bulk characterization of Al₂O₃ nanoparticle suspensions (complete datasets are provided in APPENDIX B).

Suspension Composition*	pH**	Zeta potential*** (mV)	Particle size**** (nm)
Rh 6G (0.1)	4.81 ± 0.13		
Rh 6G (0.5)	5.11 ± 0.06		
Rose Bengal (5)	5.53 ± 0.03		
Al ₂ O ₃	4.80 ± 0.17	47.41 ± 3.55	163.60 ± 16.22
Al ₂ O ₃ - SDS (15)	7.27 ± 0.22	-44.98 ± 3.71	161.02 ± 6.69
Al ₂ O ₃ - SDS (120)	7.66 ± 0.20	-48.88 ± 7.47	162.13 ± 17.45
Al ₂ O ₃ - SDS (15) - Rh 6G (0.1)	7.96 ± 0.21	-17.68 ± 2.05	176.30 ± 13.63
Al ₂ O ₃ - SDS (15) - Rh 6G (0.5)	7.94 ± 0.31	-14.34 ± 3.23	172.48 ± 10.21
Al ₂ O ₃ - SDS (15) - Rose Bengal (5)	7.25 ± 0.10	-40.00 ± 4.41	161.35 ± 11.34

* Rhodamine 6G and Rose Bengal concentrations were 0.1, 0.5 and 5ml, respectively. SDS concentrations were 15 and 120 mg/ml. These concentrations are specified in parentheses beside each compound.

** Mean ± sd (*n* = 6), 0.25 vol% Al₂O₃ nanoparticles.

*** Mean ± sd (*n* = 10), 0.25 vol% Al₂O₃ nanoparticles.

**** Mean ± sd (*n* = 6), 0.02 vol% Al₂O₃ nanoparticles. Suspensions were initially prepared at 0.25 vol%, then diluted to 0.02 vol% for DLS measurements. The surfactant and dye concentrations were therefore also diluted by the same amount (~ 1/12). At this dilution, rhodamine 6G and Rose Bengal concentrations were ~ 0.0087, 0.043 and 0.43 mg/ml, respectively. The SDS concentrations were ~1.3 and 10.4 mg/ml, respectively at the 15 and 120 mg/ml bulk conditions specified in parentheses beside each compound.

We next considered nanoparticle suspensions containing rhodamine 6G, a cationic tracer with high water solubility (20 mg/ml).¹³⁹ Visually these suspensions also appeared highly stable in bulk (Figure 34b), paradoxically contradicting the tendency

toward aggregation observed in the microchannel experiment (Figure 31). But a closer look at the bulk characterization data show that magnitude of the zeta potential decreases (moves closer to zero), consistent diminished stability. Since supra-CMC SDS concentrations were used in our experiments, we hypothesize that the presence of micellar SDS^{153, 154} (both in free solution and adsorbed on the alumina surface) reduces suspension stability by introducing a trapping mechanism for the cationic dye molecules. When these interactions occur in the vicinity of particle surface, they can lead to bridging between dye molecules and other surfactant or surfactant/nanoparticle complexes. This interpretation is supported in our DLS measurements by a slight but perceptible increase in mean cluster size. However these interactions can evidently be overcome by homogenization (stirring, ultrasonication, etc.), yielding a suspension that appears stable to the eye.

Finally, we examined Rose Bengal, an anionic xanthene dye that is also highly water soluble (100 mg/ml).¹³⁹ Again, the bulk suspension was visually stable (Figure 34c), a somewhat counterintuitive observation in light of the apparent potential for strong interactions between oppositely charged dye and alumina in the pH range of our experiments. Evidently, the presence of anionic SDS interferes with the formation of dye-nanoparticle complexes by repelling like-charged tracer molecules in vicinity of the alumina surface. This interpretation is consistent with bulk characterization data revealing that the zeta potential remains negative and decreases only slightly in magnitude, and by DLS measurements that show virtually no change in mean cluster size upon addition of the dye.

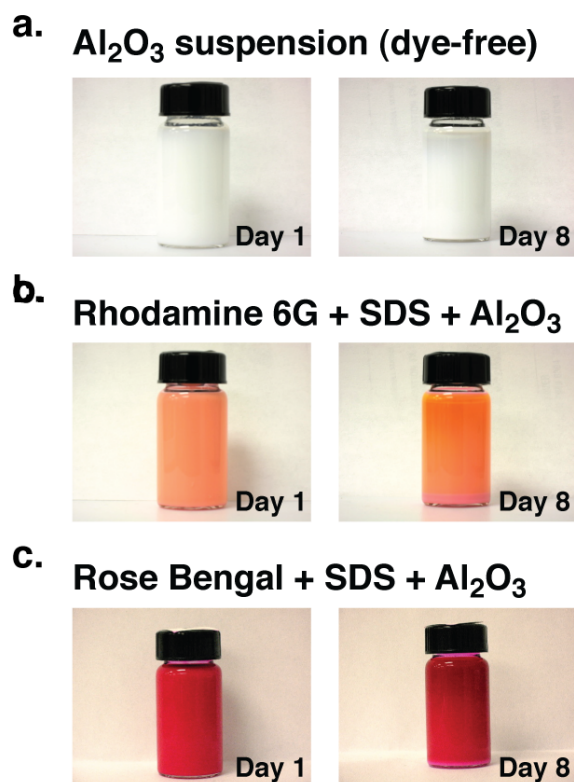


Figure 34. Tracer-laden suspensions appear highly stable in bulk despite being readily susceptible to aggregation in the microchannel-based test. (a) Aqueous 1 vol% Al_2O_3 suspensions containing no added tracer or surfactant are highly stable against sedimentation. Adding a tracer destabilizes the suspensions, but the effect is counteracted by the surfactant SDS. (b) Rhodamine 6G (0.5 mg/ml). (c) Rose Bengal (5 mg/ml). The SDS concentration in (b) and (c) was 15 mg/ml.

In addition to providing a simple yet sensitive measure of suspension stability, our results raise an intriguing question: how can the identical rhodamine 6G laden suspension that appears so highly stable in bulk become destabilized so easily in the presence of a compositional discontinuity? One may naively expect the opposite to be true—that the suspension containing Rose Bengal should be the least stable (and therefore most likely to display aggregation in the microchannel experiment) due to electrostatic attraction between the oppositely charged tracer and nanoparticles. This

contrasts with the case of rhodamine 6G, where a repulsive interaction between the like charged tracer and nanoparticles would be expected. But the scenario is more complex because the relative strength of individual interactions among all three of the suspension's principle components (nanoparticle, surfactant, and tracer) act collectively. Consequently, matching the nanoparticle and tracer charges, as in the case of rhodamine 6G, is not sufficient to guarantee stability because both the alumina and tracer compete for complexation with the oppositely charged SDS. This competitive interaction is sensitive to the presence of compositional gradients in the microfluidic environment, thereby rendering an otherwise stable bulk suspension highly susceptible to localized aggregation. Conversely, localized aggregation is suppressed in Rose Bengal despite its electrostatic attraction to alumina because the matched tracer and surfactant charges leave more free SDS available to stabilize the suspended nanoparticles.

The Rheological Behavior of Alumina Suspensions

We next searched for signatures of localized aggregation in these bulk suspensions by obtaining steady shear viscosity measurements at several nanoparticle concentrations—one of the simplest conventional characterization methods. Addition of SDS to the Al_2O_3 suspension significantly increased its viscosity at low shear rates (Figure 35a), consistent with formation of nanoparticle-surfactant complexes. Introducing rhodamine 6G yielded a steeper increase in the low shear rate viscosity, implying an increased tendency toward nanoparticle-SDS complexation in the presence of the tracer (Figure 35b). In the case of Rose Bengal the magnitude of the viscosity enhancement was somewhat greater over the entire range of shear rates. The viscosity of

the 0.25 vol% suspension was also shifted upward close to values observed at 0.5 and 1 vol%, in contrast to the dye-free and rhodamine 6G cases where the trend at 0.25 vol% more closely mirrored the particle-free sample (Figure 35c). It is therefore difficult to draw definitive conclusions from these data because weak signatures of aggregation are evident upon addition of both dyes. The presence of colloidal complexes are most probable reason for shear thinning behavior of SDS added suspensions, and it is expected that they break up in high shear zone (from 100 to 500 s⁻¹), and unscattered data resulting in constant viscosity values are collected. Similar results were also reported by Wen and Ding for TiO₂ containing suspensions.³⁰

The suspensions also exhibit low shear rate viscosity increases significantly higher than would be expected based on either the Einstein⁹⁶ or Batchelor⁹⁹ models, both of which predict enhancements by a factor of only ~ 1.025 at 1 vol% alumina. Since these models are formulated considering a simplified case of non-interacting particles with uniform size, it appears that the observed viscosity enhancements at low shear rates may reflect weak association among the suspension's components.

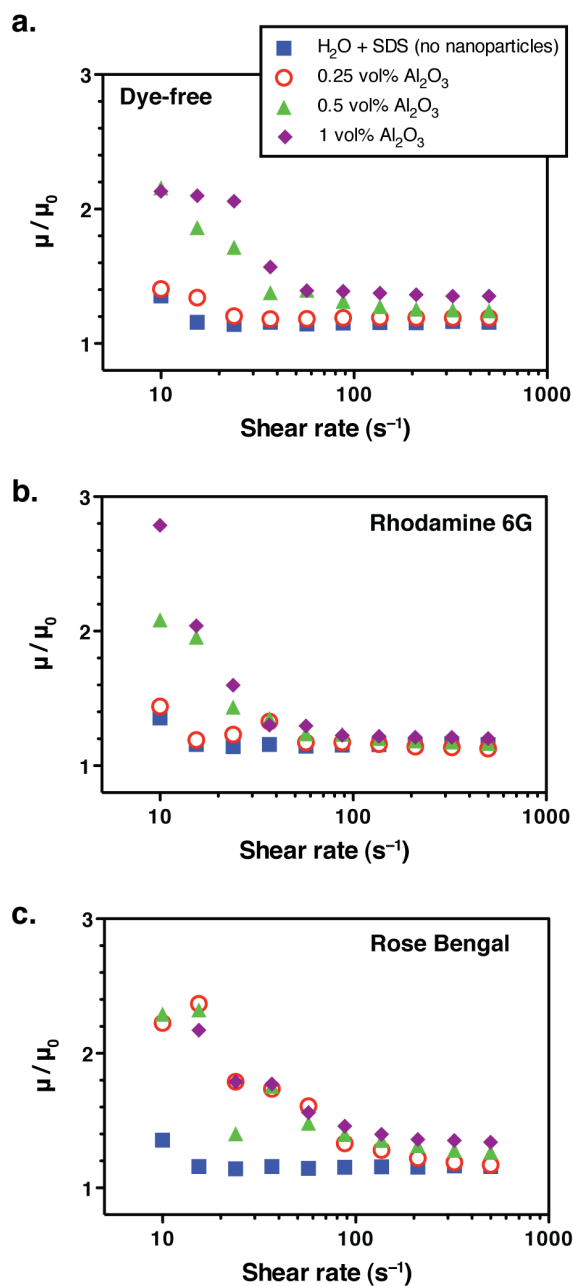


Figure 35. Steady shear viscosity measurements also indicate no strong signatures of bulk aggregation. Measurements were obtained over a shear rate sweep from 500 to 10 s⁻¹ after first ramping up from 10 to 500 s⁻¹ to generate a reproducible initial condition. Data are plotted in terms of the suspension viscosity relative to that of water (μ/μ_0). (a) In the absence of tracer, viscosity enhancement at low shear rates is observed, suggesting complexation between the nanoparticles and surfactant. (b) A somewhat sharper enhancement in low shear rate viscosity is evident upon addition of rhodamine 6G. (c) Viscosity values more closely mirror the dye-free data in (a) for suspensions containing Rose Bengal. The SDS concentration was 15 mg/ml in all cases. Rhodamine 6G and Rose Bengal concentrations were 0.5 and 5 mg/ml, respectively.

Finally, based on the analytical solution of the velocity profile for flow between parallel plates (a reasonable picture since we are interested in phenomena localized along the microchannel centerline), the maximum (wall) shear rate is estimated to be $\sim 4,000 \text{ s}^{-1}$ at the flow rate of 0.05 mL/min imposed in most of our experiments. Shear rates range from this value to zero at the center of the microchannel (the location where we hypothesize aggregation is triggered).

Thermal Conductivity Measurements

A further assessment of the tracer's effect on bulk suspension properties was obtained by performing transient hot wire measurements of thermal conductivity, a property of interest in heat transfer applications (Figure 36).

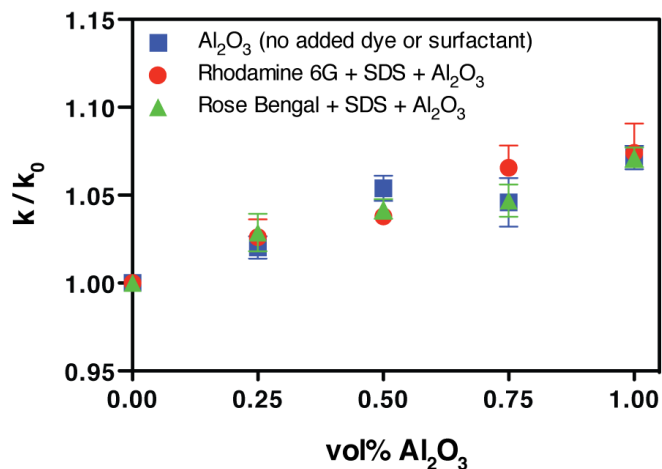


Figure 36. Thermal conductivity measurements also indicate high bulk stability. The SDS concentration was 15 mg/ml in both tracer laden suspensions. Rhodamine 6G and Rose Bengal concentrations were 0.5 and 5 mg/ml , respectively. Data are expressed relative to the particle-free case (k/k_0), and plotted with error bars representing the mean \pm s.d. of 3 independent measurements.

We used a handheld thermal property analyzer (KD2-Pro, Decagon Devices, Inc.) with the 60 mm long by 1.3 mm diameter probe. The plotted data are averages of three independent measurements (at least 20 min elapsed between each measurement, error bars represent the standard deviation). Thermal conductivity of suspensions display an increasing trend with nanoparticle concentration, in agreement with previous literature under comparable conditions.¹⁵⁶ But, these results suggest that the conductivity enhancements were not appreciably altered by addition of either rhodamine 6G or Rose Bengal. The effect nanoparticle-surfactant and/or dye complexation on the suspension's thermal conductivity is not fully understood, with conflicting results reported even in the simplest case where nanoparticle clustering interactions are considered in the absence of other additives.¹⁵⁷⁻¹⁶⁰ Although these details are beyond our focus here, the fact that we obtained virtually identical data in all cases suggests that all formulations display similar bulk stability.

5.4 Final Remarks

These aforementioned complexities also highlight additional challenges associated with working with non-ideal multicomponent colloidal systems encountered in many practical settings where individual interactions often cannot be fully isolated in the same way that is possible in fundamental studies of simple ideal colloids. For example, it could be anticipated that the lateral position of the interfacial aggregation zone in the microchannel experiment may provide information about the conditions necessary for aggregation owing to the locally varying particle, surfactant, and tracer concentration profiles. We attempted to apply this idea by injecting nanoparticle

suspensions containing progressively increasing surfactant concentrations into the microchannel, expecting to observe a corresponding lateral shift in the location of the aggregation zone coinciding with the shift in the stabilizing surfactant's concentration profile. Experimentally, however, we found that this measurement was not as straightforward to perform as we anticipated due to the significant enhancement in suspension viscosity that occurred as more surfactant was added. This produced an increasingly severe mismatch between co-flowing streams in the microchannel that acted to displace the entire interface between them such that the lower viscosity tracer solution occupied a smaller fraction of the cross-section. Any influence of surfactant concentration on the position of the aggregation zone therefore became obscured since the interface between streams could not be consistently maintained at the centerline. The situation is further complicated by the fact that any attempts to match viscosities by altering the composition of the tracer-laden stream are likely to also alter the aggregation phenomena, making a systematic study challenging. It is also possible to exploit the interfacial shift to infer the viscosities of each stream, however we hesitate to extract quantitative information from these displacements because the position and shape of the interface become distorted (sometimes significantly) by the aggregation phenomena also taking place.

An additional difficulty emerges from the dependence on preparation method. The bulk nanoparticle suspensions shown in Figure 34 were prepared using a combination of mechanical stirring and ultrasonic agitation following well-established methods to ensure homogeneity and stability. To more closely correlate the bulk and

microchannel-based experiments, a titration experiment was performed by adding rhodamine 6G directly into nanoparticle suspensions at different surfactant concentration, with the expectation of observing a threshold aggregation concentration that could be correlated with the lateral position of the aggregation zone in the microchannel experiment (Figure 37). But instead, we found that preparing the suspensions in this way always produced visible sedimentation in only a few minutes after addition of the tracer. We did not apply stirring or ultrasonication in these titration experiments in an effort to mimic phenomena in the microchannel environment. This effect made it difficult to distinguish any clear differences in aggregation phenomena across a broad range of surfactant concentrations.

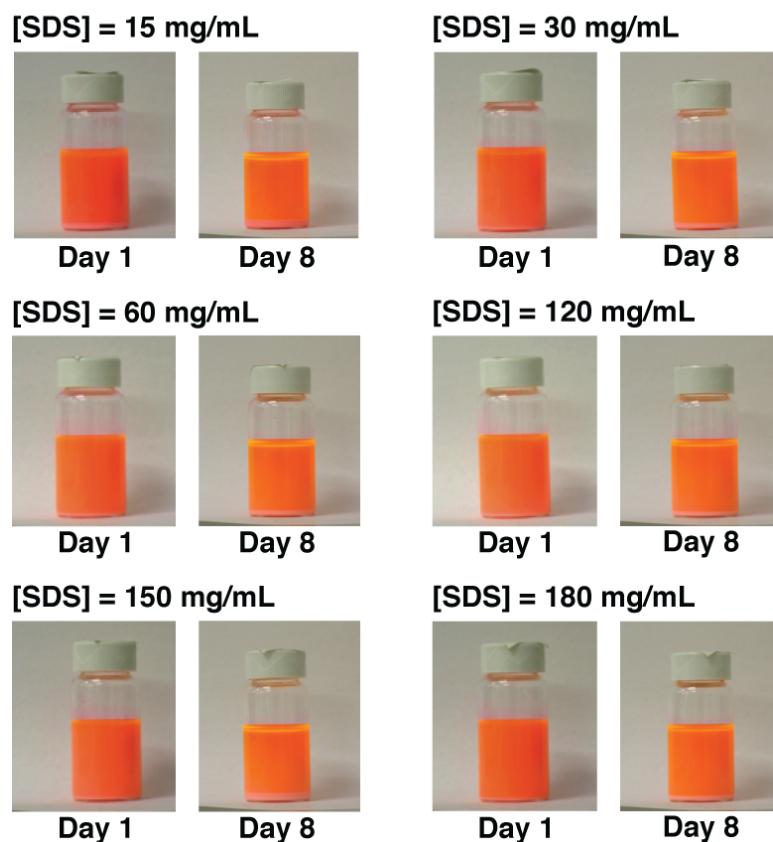


Figure 37. Photographs showing results of a titration experiment whereby a 7 mL aliquot of aqueous rhodamine 6G (0.5 mg/ml) solution was added to 7 mL of a series of 1 vol% Al_2O_3 suspensions with increasing SDS concentration. In all cases, sedimentation at the bottom of the container became evident within a few minutes after adding the tracer.

In both scenarios considered here, the base state is a surfactant stabilized nanoparticle suspension. In the bulk case, dye is added into a large reservoir of the suspension. Gradients between dye and surfactant exist locally, but their effects can be counteracted by homogenization (stirring, sonication, etc.). In this way, potentially destabilizing interactions can be overcome (to an extent). In the microchannel case, we more closely examine the interfacial phenomena by challenging the suspension with a sharp chemical gradient between the dye and the suspension. This is a relevant scenario

in cases where a tracer dye is injected into a carrier fluid.^{31, 38, 45-51, 161} Since bulk homogenization is not possible, suspension stability evolves differently. We therefore suggest that the microfluidic environment provides a useful tool to evaluate these destabilizing interactions and guide rational selection of formulations suitable for these kinds of applications. Without this approach, one may instinctively attempt to prepare apply the standard suite of bulk characterization methods to evaluate whether the dye would destabilize a nanoparticle suspension, potentially leading to erroneous conclusions.

From a practical standpoint, the ability to distinguish differences in stability that appear relatively subtle even when examined using conventional bulk characterization techniques (zeta potential, DLS) makes a compelling case in favor of the simplicity of the microfluidic method. We also note that the dilution required to accurately employ DLS inherently excludes direct analysis of suspensions at the same concentrations employed in our other experiments. Furthermore, our attempts to acquire zeta potential measurements at relevant concentrations (0.25 vol%) were hampered by electrode fouling caused by the high surfactant, tracer dye, and nanoparticle concentrations that, if left uncorrected, introduced fluctuations and variability in the data. We explored measuring zeta potential at the 0.02 vol% dilution used in the DLS experiments but found that the values (including all dye laden suspensions) became highly negative (-70 to -90 mV) indicating strong stability for all formulations. We therefore chose to conduct these measurements at 0.25 vol% to attain a more realistic representation of the state of the surface in our suspensions. These challenges show how the microfluidic

approach offers a useful tool to enable rapid assessment of quality and variability among suspensions under application-specific conditions, in both laboratory-based and large-scale manufacturing settings.

6. GRAPHENE-ENHANCED NANOREFRIGERANTS

6.1 Introduction

There is a critical need for advanced cooling and thermal dissipation systems capable of operating with greater energy efficiency while simultaneously meeting the increasing demands of new applications. Even modest enhancements in thermal efficiency can produce huge energy savings when implemented on a global commodity scale. Since heat transfer fluids are primary contributors to thermal performance, there is naturally intense interest in developing advanced formulations that display superior thermal properties. In view of this importance, considerable excitement has recently been directed toward a particular class of colloidal suspensions (so-called *nanofluids*) composed of ultrafine metal or nonmetallic nanoparticles owing to reports of potential to improve thermal transport by orders of magnitude.^{10-12, 15-25, 38, 162-164}

Remarkable thermal properties of nanoparticle suspensions have led researchers to employ them in refrigeration and refrigerant employed systems.^{54, 104, 106} Most of the studies focused on the effect on nanorefrigerant (in which refrigerant is the host fluid) boiling transfer enhancements.^{55, 107, 165} But despite these promising results, lingering uncertainties remain because of a lack of follow-up studies that conclusively support these findings.^{53, 92}

In this study, we fulfill the ongoing need for systematic studies of bulk thermal conductivity in nanofluid formulations by investigating a commercial host refrigerant

containing dispersed graphene nanosheets (GNS), multi-wall carbon nanotubes (MWCNTs) and nanoparticles (TiO₂). We introduce a new surfactant-based dispersal approach that enables stable suspensions containing a wide range of nanomaterials to be straightforwardly prepared as additives to ordinary commercial refrigerants. We selected the hydrofluoroether (HFE) refrigerant Novec 7500 (3M) as the host fluid for our studies owing to its wide appeal in applications ranging from microelectronics to chemical process equipment, combined with the desirable property that it remains in the liquid phase under ambient conditions.¹¹² We disperse nanomaterials obtained from commercial vendors in the refrigerant at concentrations ranging from 0.25 to 1 vol% with the aid of the fluorocarbon stabilizer Krytox 157 FSL (DuPont), a low molecular weight ($\sim 2,500 \text{ g mol}^{-1}$) monofunctional carboxylic acid-terminated perfluoropolyether. Our formulations are distinguished by the use of a realistic fluorocarbon-based stabilizer, in contrast to previous studies employing viscous oil-based lubricants.^{54, 105} By exploiting this new capability, we find that graphene nanosheet additives uniquely match the superior thermal conductivity enhancements attained in carbon nanotube suspensions, but unlike nanotubes the suspension viscosity is only minimally increased. Our focus in this paper is on formulations relevant for real-world applications that can be readily prepared using commercially available components. We therefore consider only low particle loadings (below 1 vol%) that minimize viscosity and enhance long-term stability. Although our ability to match the most extreme thermal conductivity enhancements reported at much higher loadings is limited, this is far outweighed by the greater practical utility of the formulations studied here which can be directly introduced

into existing refrigeration systems. We conclude by proposing an accessible experimental approach to standardize property analysis of refrigerant-based nanosuspensions.

6.2 Colloidal Stability of Nanorefrigerant

The suspensions of graphene nanosheets (GNS), multi-wall carbon nanotubes (MWCNTs) and nanoparticles were prepared at concentrations of (0.25, 0.5 and 1 vol%) using two-step nanofluid production method. The surfactant concentration was chosen to be as low as possible to maintain suspension stability without appreciably altering the suspension viscosity (the refrigerant viscosity only increased by 3 – 4% upon addition of surfactant, Table 6).

Table 6. Effect of added surfactant on refrigerant steady-shear viscosity. Data are shown as a function of shear rate (averaged over an ensemble of 5-10 experiments at each temperature), and as an average over all shear rates at each temperature.

T (°C)	Shear rate (s ⁻¹)	Viscosity (Pa s)		Percent Change	Average
		HFE 7500	HFE 7500 & Krytox 157		
2	500	0.001798	0.001848	2.78%	3.90%
	324	0.001796	0.001846	2.78%	
	210	0.001796	0.001844	2.67%	
	136	0.001798	0.001846	2.67%	
	87.9	0.001798	0.001854	3.11%	
	56.9	0.001808	0.001848	2.21%	
	36.8	0.001832	0.001852	1.09%	
	23.9	0.001712	0.001914	11.80%	
	15.4	0.001904	0.001948	2.31%	
	10	0.001796	0.001932	7.57%	
12	500	0.001496	0.001549	3.52%	3.25%
	324	0.001495	0.001551	3.71%	
	210	0.001491	0.001538	3.17%	
	136	0.001488	0.001535	3.18%	
	87.9	0.001487	0.001537	3.36%	
	56.9	0.001495	0.001540	3.04%	
	36.8	0.001503	0.001558	3.69%	
	23.9	0.001464	0.001532	4.66%	
	15.4	0.001464	0.001514	3.39%	
	10	0.001477	0.001489	0.80%	
22	500	0.001290	0.001330	3.10%	2.91%
	324	0.001290	0.001330	3.10%	
	210	0.001284	0.001324	3.12%	
	136	0.001282	0.001322	3.12%	
	87.9	0.001280	0.001326	3.59%	
	56.9	0.001304	0.001336	2.45%	
	36.8	0.001302	0.001348	3.53%	
	23.9	0.001312	0.001304	-0.61%	
	15.4	0.001354	0.001442	6.50%	
	10	0.001296	0.001312	1.23%	

The use of a fluorocarbon stabilizer merits some discussion as it is a distinguishing feature of our approach. Ionic surfactants (e.g., sodium dodecyl sulfate (SDS), cetyltrimethylammonium bromide (CTAB)) are conventionally employed to enhance suspension stability through their ability to tune interactions associated with ionic repulsion.^{58, 75, 166} But these additives are ineffective in preparation of stable refrigerant-based suspensions. Krytox 157 FSL enhances stability in a different way, owing to chemical compatibility between its monofunctional carboxylic acid-terminated perfluoropolyether moiety and the fluorinated refrigerant.¹⁶⁷ The perfluoropolyethers (PFPE) are soluble in freon or other fluoruous solvents due to chain flexibility provided by the ether oxygen of surfactant.^{168, 169} The functionality of our surfactant come from a carboxylic acid group located on the terminal fluoromethylene group. This class of surfactant acts to increase miscibility through adsorption to the nanomaterial surface after which compatible chemical groups are presented to the surrounding refrigerant (Figure 38a). Our stabilization approach can be broadly applied to disperse other nanomaterials in refrigerant host fluids.

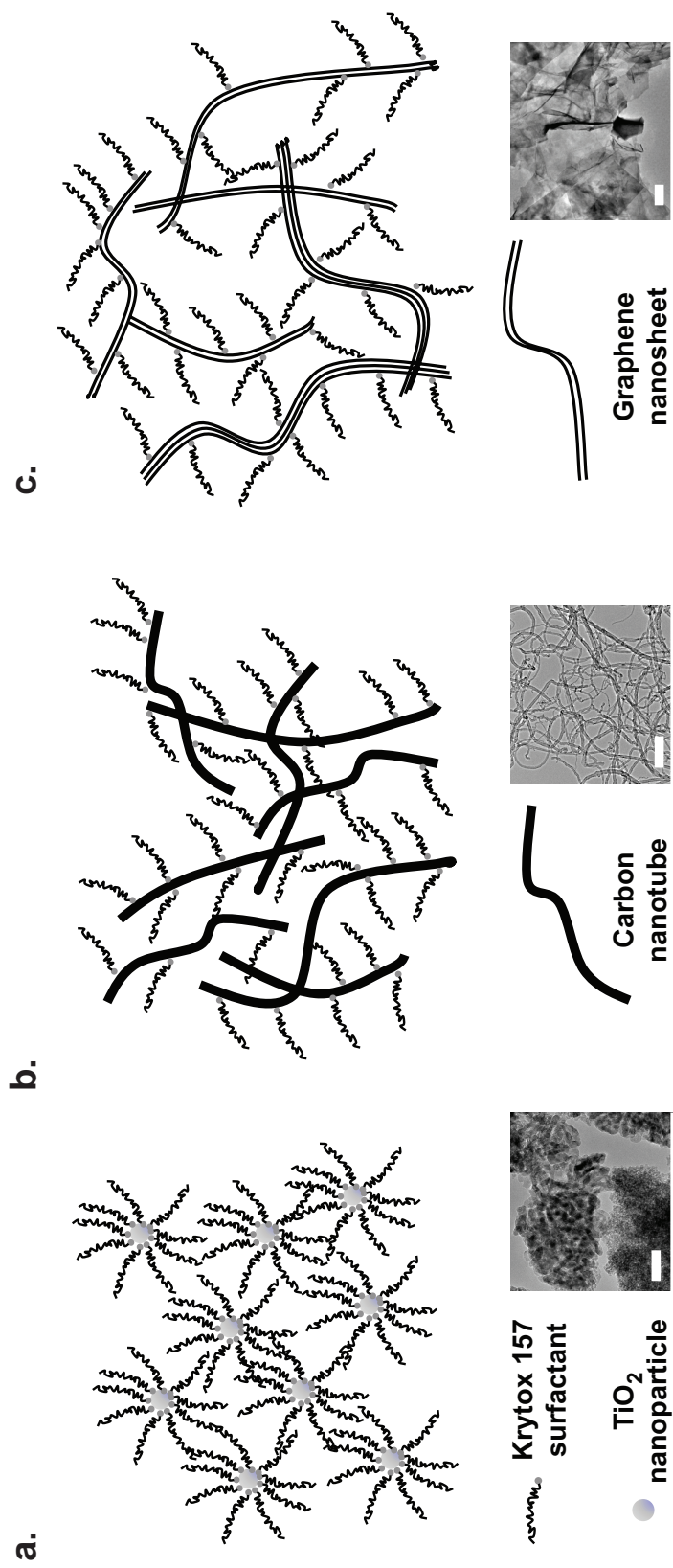


Figure 38. Surfactant-mediated stabilization of nanomaterials in a fluorinated refrigerant host liquid. Compatible chemical groups are presented to the surrounding fluid upon adsorption to (a) TiO₂ nanoparticles, as well as bundles containing (b) carbon nanotubes and (c) graphene nanosheets. Insets show TEM images of nanomaterials employed in our studies (scale bars are 50 nm, 400 nm, and 500 nm in (a), (b), and (c), respectively).

Steric effects also play an important role in the case of carbon nanotubes and graphene nanosheets, where the adsorbed surfactant counterbalances van der Waals interactions between neighboring nanotube/sheet bundles (Figure 38b and c).¹⁷⁰ These modes of stabilization are distinct from those associated with oil-based lubricants employed in previous studies, whereby the nanomaterials primarily remain confined within the dispersed oil phase and experience only limited contact with the refrigerant.

6.3 Measurements of Thermal Conductivity in Nanorefrigerants

A series of transient hot wire measurements of suspension thermal conductivity were performed to ascertain the extent to which the refrigerant's thermophysical properties are influenced by the nanomaterial additives. We first focus on multi-wall carbon nanotubes (MWCNTs) and graphene nanosheets (GNS), of particular interest because they are expected to display the strongest conductivity enhancements as a consequence of their superior material properties and greater interfacial contact with the host fluid as compared with isotropic nanoparticles.^{113, 171-173} Our experiments confirm this expectation, where we observe substantially increased thermal conductivities in MWCNT suspensions acquired from two different vendors (more than 15% in the 1 vol% suspension), with the most substantial conductivity enhancements occurring at the highest nanotube loadings (Figure 39a). It is generally accepted that these enhancements at least partially reflect emergence of conductivity percolation paths whereby the suspended nanotubes begin to adopt 3-D network arrangements, thereby providing avenues for ballistic phonon transport. But this basic picture is complicated by local agglomeration that can create insulating voids, the inherently strong thermal anisotropy

of carbon nanotubes, and other local concentration fluctuations associated with the suspension's components.^{174, 175} The observed magnitude of the enhancements are in agreement with those of Wen and Ding involving aqueous carbon nanotube suspensions in a similar concentration range,⁸⁹ but are much lower than those reported by Choi et. al. in poly (α -olefin) oil-based dispersions.¹¹³ A relatively weak trend of increasing conductivity with decreasing temperature was evident (Figure 39b), and the refrigerant thermal conductivity changed by less than 1% upon addition of surfactant (Table 7). The decreasing trend of typical thermal conductivity data of refrigerant could be accounted as a most probable reason for this result.

Table 7. Effect of added surfactant on refrigerant thermal conductivity. Data shown are average values over the entire ensemble of experiments reported (see main text for details).

T (°C)	Thermal Conductivity (W m ⁻¹ K ⁻¹)		Percent Change
	HFE 7500	HFE 7500 & Krytox 157	
2	0.09233	0.09233	No change
12	0.09383	0.09317	-0.71%
22	0.09300	0.09267	-0.36%

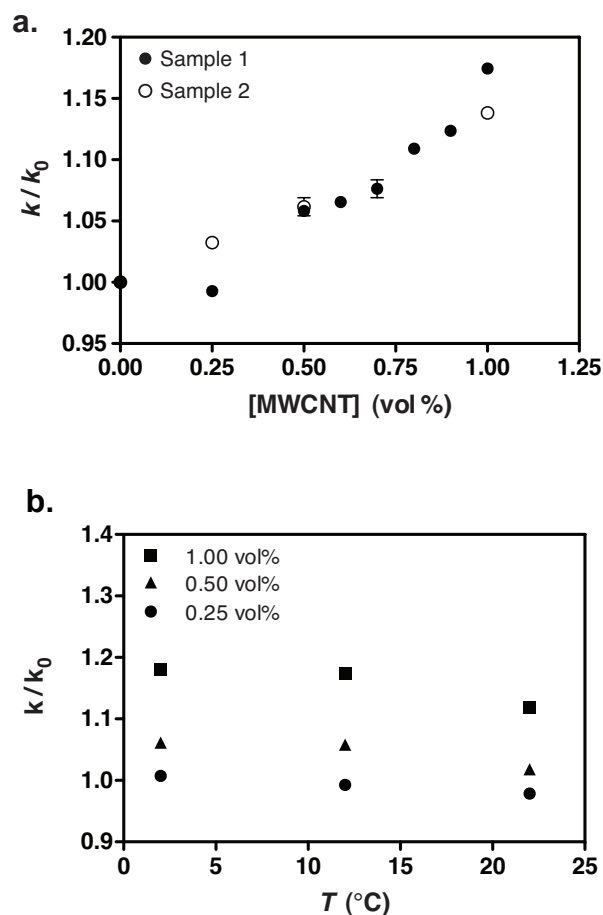


Figure 39. MWCNT-based nanorefrigerants display enhanced thermal conductivity. (a) Thermal conductivity measurements of suspensions containing MWCNTs obtained from two different commercial vendors indicate a $\sim 15\%$ enhancement at a loading of 1 vol % at 12°C (Sample 1: Cheap Tubes, Inc.; Sample 2: Helix Material Solutions, Inc.). (b) Temperature dependence of thermal conductivity in refrigerant suspensions containing MWCNTs (Sample 2: Cheap Tubes, Inc.) Data are expressed relative to the particle-free case k/k_0 . All refrigerant solutions contained 1 vol% Krytox 157 FSL.

GNS suspensions display similar thermal behavior as the MWCNTs, albeit the magnitude of the conductivity enhancement is slightly lower ($\sim 10\%$ at 1 vol%; Figure 40). Although somewhat counterintuitive given that the in-plane thermal conductivity of single-layer graphene ($\sim 5,200 \text{ W m}^{-1} \text{ K}^{-1}$) is higher than carbon nanotubes ($\sim 3,000 \text{ W m}^{-1} \text{ K}^{-1}$),^{56, 171} this discrepancy may reflect inhomogeneities in the commercially

obtained materials we employed (e.g., variations in nanosheet size and concentration of defects). But remarkable differences emerge between the GNS and MWCNT suspensions when their steady shear viscosity behavior is compared as we see in the following section (see the figures on Page 113 and 115).

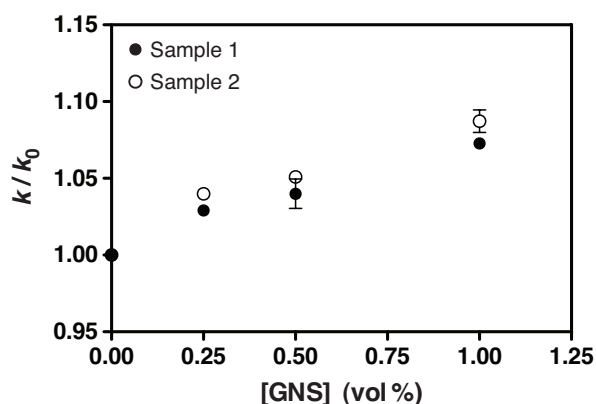


Figure 40. Graphene-based nanorefrigerants display enhanced thermal conductivity. Thermal conductivity measurements of suspensions containing GNSs obtained from two different commercial vendors (Sample 1: Skyspring Nanomaterials, Inc.; Sample 2: Cheap Tubes, Inc.; data are expressed relative to the pure refrigerant (particle- and surfactant-free) k/k_0) at 12°C. All refrigerant solutions contained 1 vol% Krytox 157 FSL.

Our surfactant-mediated approach can be broadly applied to disperse other nanomaterials in refrigerant host fluids. We demonstrated this by producing stable suspensions containing TiO₂ nanoparticles (anatase, spherical morphology), however the refrigerant's thermal conductivity is virtually unchanged at loadings comparable to the GNS and MWCNT dispersions (Figure 41).

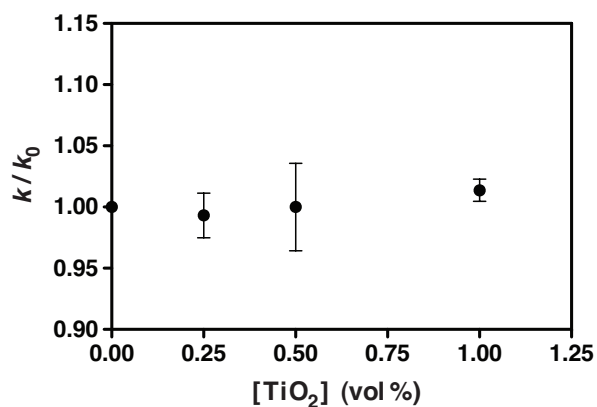


Figure 41. Minimal thermal conductivity enhancements are observed in nanoparticle-based refrigerant suspensions. Thermal conductivity measurements of dispersions containing TiO₂ nanoparticles display little change from those of the particle-free host refrigerant. Data are expressed relative to the pure refrigerant (particle- and surfactant-free) k/k_0 , all measurements were performed at 12 °C.

Although there are no comparable data in the literature regarding TiO₂-based refrigerant suspensions, our observations are consistent with the small conductivity enhancements observed in aqueous suspensions (up to 3% at 1 vol% loading).¹⁷⁶⁻¹⁷⁸ We therefore conclude that GNS additives offer a considerably more attractive avenue than conventional nanoparticles to augment the thermal performance of commercial refrigerants.

6.4 Rheological Characteristics of MWCNT and GNS Suspensions

We performed steady-shear viscosity measurements over shear rates decreasing from 500 to 10 s⁻¹ (the shear rate was first ramped from 10 to 500 s⁻¹ to ensure attainment of a reproducible initial condition). Significantly enhanced low shear rate viscosities are evident with increasing MWCNT concentration, and all suspensions display shear thinning behavior—both characteristics associated with the presence of an

underlying loosely entangled morphology (Figure 42a). The viscosity increase is also visually evident by a substantial loss of fluidity, with suspensions acquiring a thick mud-like consistency at concentrations above 0.5 vol%. In fact, this simple visual inspection is sufficient to conclude that it would be extremely challenging to obtain suspensions suitable for realistic cooling applications. Shear thinning⁸⁹ has been previously reported in aqueous nanotube suspensions, however the viscosity values we observe are higher than those reported in comparable literature,¹⁷⁹ likely reflecting variations in fluid composition and preparation. The magnitude of the viscosity enhancements we observe may be a manifestation of increased surface area presented by a dispersed suspension and its effect on interparticle interactions¹⁸⁰ consistent with predictions of Tseng and Lin based on studies of aqueous anatase TiO₂ suspensions where the effects of strengthened interparticle interactions at increasing concentration were considered.¹⁰¹ We also observed a moderate temperature dependence (Figure 42b). Since the pure refrigerant viscosity decreases by ~ 40% over the temperature range of our tests, it seems reasonable to suggest that interactions between the CNTs and the Krytox dispersant may display a relatively strong temperature dependence.

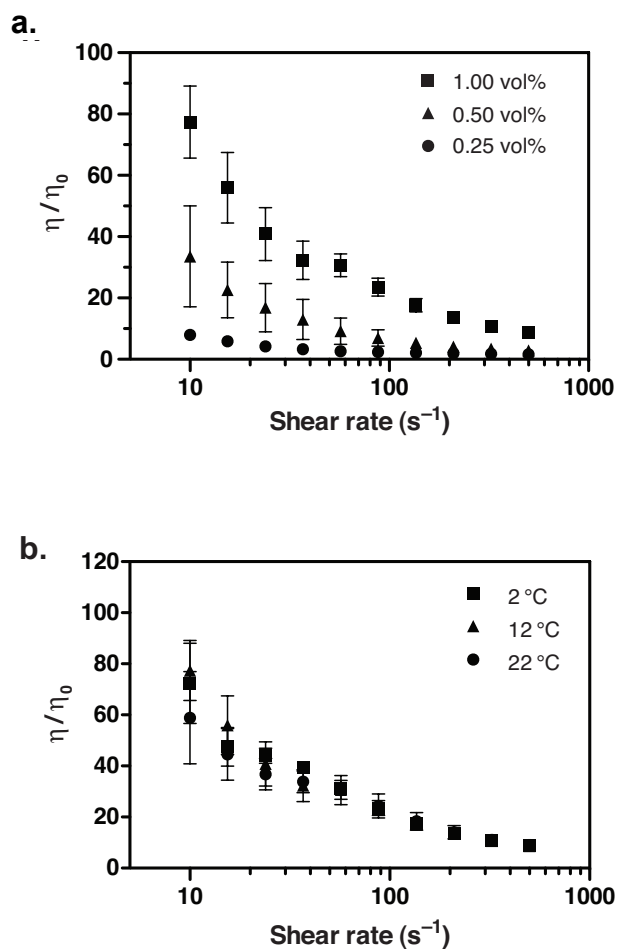


Figure 42. (a) Steady shear viscosity measurements show a dramatic increase at low shear rates (results are plotted relative to the pure refrigerant (particle- and surfactant-free) η/η_0 ; Table 5). All the experiments were carried out at a constant temperature of 12°C. (b) Temperature dependence of steady shear viscosity in a 1 vol% MWCNT dispersion. Data shown are for nanotubes obtained from Cheap Tubes, Inc. and expressed relative to the pure refrigerant (particle- and surfactant-free) (η/η_0) over a shear rate sweep from 500 to 10 s^{-1} after first ramping up from 10 to 500 s^{-1} to generate a reproducible initial condition. All refrigerant solutions contained 1 vol% Krytox 157 FSL.

Even at the highest particle loadings, the magnitude of the low shear rate viscosity enhancement displayed by the GNS suspensions (10 – 20%) is overwhelmingly lower than the > 1,000% increase in comparable nanotube laden formulations (Figure 43). It is reasonable to interpret at least part of this discrepancy to morphological

differences between the two materials. Although both are highly anisotropic, the rod-like shape of nanotubes is more amenable to formation of a long range entangled network than the planar disk-like graphene nanosheets.

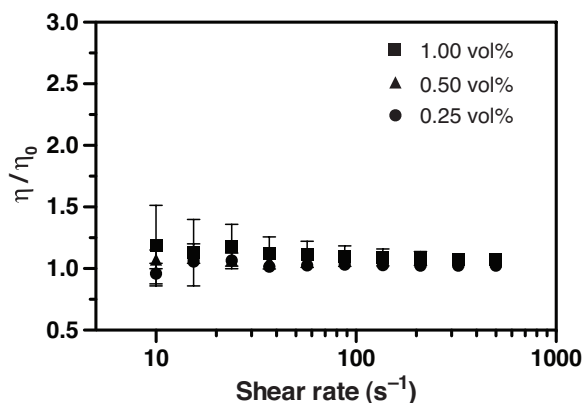


Figure 43. Only a minimal increase in steady shear viscosity is observed (data shown are for Sample 2 obtained over a shear rate sweep from 500 to 10 s⁻¹ after first ramping up from 10 to 500 s⁻¹ to generate a reproducible initial condition, results are plotted relative to the pure refrigerant (particle- and surfactant-free) η/η_0 ; Table 5). All measurements were performed at 12 °C.

Our observations are in agreement with those of Samuel, et al. who reported a ~5% increase in kinematic viscosity of Castrol Clearedge 6519 at graphene nanoplate loadings of 0.5 wt%—an enhancement much more pronounced with addition of MWCNTs.¹⁸¹ It is notable that there is currently a lack of extensive experimental studies related to the rheology of GNS-laden nanofluids,¹⁰² suggesting that our viscosity measurements can provide a useful reference for future investigations. These observations show how graphene nanosheets confer the advantage of superior thermal properties without the viscosity penalty associated with formation of an extended network arrangement.

It is also found that the magnitude of observed viscosity increase is significantly higher than the predictions by Brinkman and Maiga et al.^{98, 182} Tseng and Lin found an exponential relation between μ_{eff}/μ_{H_2O} and volume fraction of anatase titanium dioxide (TiO₂) nanoparticles in water (Equation 10) and laid emphasis on particle aggregation due to strong attraction as ϕ increased.¹⁰¹ The relative viscosity values estimated from this model are much closer to the experimental values we obtained.

While GNS suspensions can in principle be prepared at particle loadings beyond 1 vol%, a tradeoff begins to emerge between the desirable effects of enhanced thermal properties and deleterious effects of increased viscosity and reduced stability. As expected, the suspension viscosity continues to rise at higher particle concentrations (Figure 44a). The factor of two increase in the low shear rate value at 4 vol%, though still modest compared with the dramatic viscosity increases observed in MWCNT, is still an important consideration in real-world applications (the pressure drop required to pump fluid through a conduit is proportional to its viscosity). The long term stability of these suspensions, however, is more dramatically affected as evident by noticeable sedimentation after only 48 h at concentrations above 1 vol% (Figure 44b).

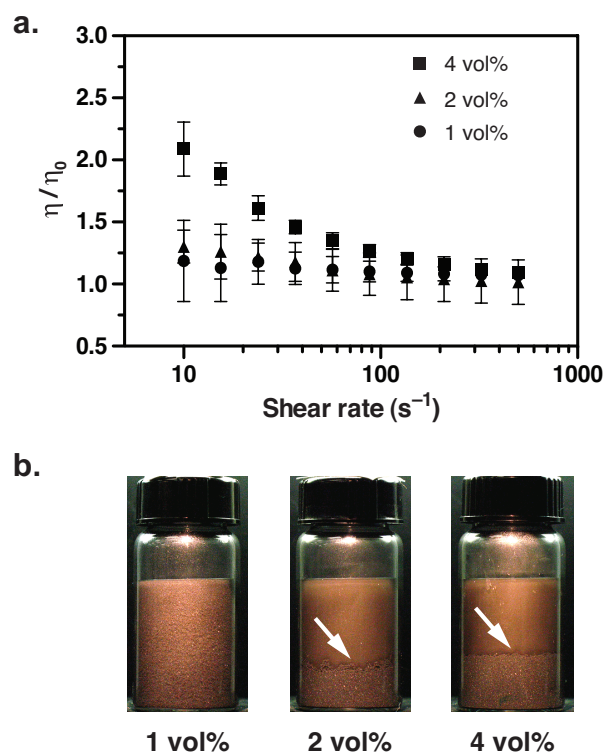


Figure 44. Nanosuspension viscosity and long term stability at GNS loadings above 1 vol%. (a) Steady shear viscosity continues to increase at higher GNS loadings, but the enhancements are much more modest than in MWCNT dispersions (experiment conditions are identical to those in Figure 43). (b) Photographs showing GNS suspension stability as a function of particle loading after 7 days of incubation at room temperature. Loadings of 1 vol% and below (left) display excellent long term stability while significant sedimentation occurs at higher concentrations (arrows), becoming evident after as little as 48 h. Materials were obtained from Cheap Tubes, Inc.

Consequently, we did not attempt to collect thermal conductivity data at these higher loadings. Although the measurements could be performed immediately after suspension preparation, we believe this would not present a meaningful assessment of performance in realistic settings where long term stability is important. Thus, we suggest that 1 vol% represents a practical upper limit to the GNS loading in refrigerant-based systems where it is desirable to achieve significantly augmented thermal properties

without an appreciable viscosity increase. These suspensions can therefore be directly substituted for conventional refrigerants in many applications.

6.5 Final Remarks

In Table 8, we briefly summarize our results and compare them with previous related findings involving refrigerant-based suspensions. One notable observation is that the thermal conductivity enhancements in MWCNT dispersions ($\sim 15\%$) are more modest than the $\sim 100\%$ increases reported by Jiang, et. al.¹⁰⁴ Not only is this discrepancy unusually large, it is also virtually impossible to identify specific factors to which the disparity can be attributed due to differences in the suspension components, preparation protocols, experimental methodologies, and instrumentation employed for property measurement. To address this, we propose a standardized approach based on commercially available instrumentation that can help to alleviate some of the difficulties encountered when attempting to draw meaningful comparisons among data reported in literature. This strategy is described in detail in thermal conductivity measurements section of Experimental Methods, but we highlight some of the key considerations below.

First, refrigerant host fluids pose unique challenges not encountered in conventional aqueous-based suspensions. The ability to acquire reliable thermal property data is often compromised by the high volatility of many refrigerant formulations that makes them difficult (or even impossible) to work with under ambient conditions. We address this through the use of a commercially available HFE refrigerant displaying a high boiling point, making suspension preparation and experimental handling much

easier than would otherwise be possible. Suspension stability is also greatly enhanced through our use of a fluorocarbon-based dispersant that promotes chemical compatibility between the particles and surrounding host fluid environment as compared with viscous lubricant oils often employed in other studies.

Next, our suspension preparation protocol involves a combination of ultrasonic agitation and magnetic stirring to ensure consistent homogeneous dispersal of the nanomaterials. We first mix the surfactant and refrigerant (the most chemically miscible components), after which the nanomaterials are added. Ultrasonication time is especially critical in carbon nanotube-based formulations, and care should be taken to ensure that it is clearly reported. Previous studies of aqueous carbon nanotube dispersions have suggested that long ultrasonication times act to break down the size of nanotube aggregates and even decrease the nanotubes' aspect ratio, resulting in a decreased suspension viscosity.¹⁷⁹ Surprisingly, we observed the opposite effect in the refrigerant-based system, whereby suspensions became more viscous upon increasing exposure to ultrasonication. To ensure suspension homogeneity, we prepared all samples in transparent glass beakers so that they could be continuously observed during all stages of study, specifically focusing on telltale signs of precipitation occurring at the edge and/or bottom of the container.

Table 8. Summary of thermal characterization studies involving refrigerant-based nanofluids.

Nanomaterial	Loading	Host Fluid	Dispersant	Measurement Method	Key Observations	Ref.
Carbon nanotubes, graphene, TiO ₂	0.25 – 1 vol%	HFE-7500	Krytox 157-FSL	Transient hot wire (KD2)	~ 10 – 15% increase in thermal conductivity (MWCNT and GNS)	This work
Carbon nanotubes	0.2 – 1 vol%	R113	–	Transient plane source	> 100% increase in thermal conductivity	104
Carbon nanotubes	1 vol%	R123 and R134a	–	Stainless steel boiling vessel	~30% enhancement in flow boiling heat transfer coefficient	107
TiO ₂ , Al ₂ O ₃	6 – 10 wt%	HFC134a/ SUNISO 3GS	–	Refrigeration efficiency	26 % energy saving	54
TiO ₂	0.01 – 0.05 vol%	R141b	–	Surface of a horizontal cylindrical copper tube	Decrease in nucleate pool boiling heat transfer	92
Al ₂ O ₃	1 – 2 wt%	Lubricant of R134a	–	Transient hot wire (KD2)	~5% increase in thermal conductivity	105
SiO ₂	0.05 – 0.5 vol%	R134a	Hexamethyl disilazane	Concentric counter flow heat exchanger	~55% decrease in flow boiling heat transfer coefficient	53

Finally, the thermal conductivity measurement protocol is another critical factor in obtaining consistent results (Figure 19). We find that it is important to prepare relatively large quantities (~ 300 ml) of the refrigerant-based suspensions in order to permit sufficient fluid volume between the sensor and sidewall of the glass beaker (at least 1.5 cm in all directions). Thermal conductivity measurements were performed using a commercially available thermal property analyzer (KD2-Pro, Decagon Devices, Inc.) to provide a standard platform that can be readily adopted by different research groups, as opposed to many previous studies that employ custom built measurement devices. The minimum allowable read time (1 min) was used owing to the relatively low viscosity of most refrigerant-based suspensions, and measurements were performed using the stainless steel KS-1 probe (60 mm long by 1.3 mm diameter) in order to avoid excessive heating which can introduce errors due to local free convection. Evaporation during measurements was prevented by using open-top polypropylene screw caps bonded with Teflon/silicone septa through which the thermal probe was inserted. All measurements were performed on an optical table, and the isothermal bath was switched off during all measurements to eliminate vibration effects. Adherence to this protocol enabled us to obtain reproducible thermal conductivity measurements in refrigerant-based nanofluids. We hope that these studies can help alleviate uncertainties surrounding the extent of achievable thermal enhancement so that nanofluids can ultimately fulfill their potential as advanced heat transfer fluids.

7. PHYSICAL AND THERMAL CHARACTERIZATION OF COMMERCIAL REFRIGERANTS WITH NANOFILLERS

7.1 Introduction

Nanorefrigerants prepared by suspending nanoparticles in the refrigerants is a new interest to the scientific community. Their thermal performances in cooling and refrigeration systems, including boiling heat transfer, have been recently investigated although a solid consensus on the conclusions has not been reached yet.^{53-55, 92, 106, 107, 165} On the other hand, experimental studies on the fundamental properties of nanorefrigerants, such as thermal conductivity, viscosity and stability performance are very limited.^{104, 105} Therefore there is a great potential on these research topics in order to determine the effects of nanorefrigerants on heat transfer.

In the previous chapter, we compared the thermal conductivity and rheological behavior of carbon nanotubes and graphene nanosheets. Here, we present a complementary study based on refrigerant suspensions of metal oxide and nitride nanoparticles by considering bulk characterization techniques. We systematically prepare suspensions of nanoparticles including TiO₂, Al₂O₃, ZnO, CuO and AlN with our host refrigerant, HFE 7500 (3MTM NovecTM 7500 Engineered Fluid) using the same surfactant mediated approach introduced before. Good stability of a suspension is closely related to the surface charge density of particles that generates strong repulsive forces. Therefore, we evaluate the colloidal stability and electrophoretic behavior of our

suspensions by analyzing the zeta potential values and particle size (DLS). Then, we examine the effects of particle type and concentration on the thermal conductivity of nanorefrigerants with an accessible experimental approach in order to robustly assess the variation. We also measure the steady shear viscosity of these nanorefrigerants in order to get some clues about their flow behavior in the cooling systems.

7.2 Surfactant-mediated Particle Dispersion Approach

Our suspensions of nanoparticles were prepared at concentrations of 0.25, 0.5 and 1 vol% with the aid of the fluorocarbon stabilizer, Krytox 157 FSL (DuPont Chemicals). We again used the hydrofluoroether (HFE) refrigerant (3M™ Novec™ 7500 Engineered Fluid) as a host fluid for our studies.¹¹² As we described before, HFE 7500 dissolves Krytox 157 FSL easily due to chemical compatibility between its perfluoropolyether moiety and the fluorocarbon fluid (Figure 45).

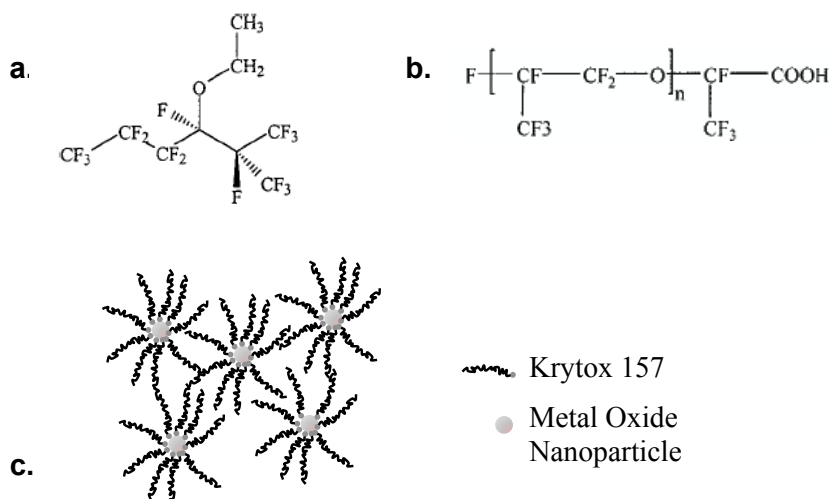


Figure 45. Chemical structures of (a) HFE 7500, (b) Krytox 157 FSL ($n \sim 14-17$), (c) Stabilization process of nanoparticles.

The stabilization mechanism in our nanorefrigerants is expected to be a combination of electrostatic and steric stabilization. The electrostatic stability is maintained through the surface attachment of surfactant with its functional group, and after which its fluoroalkylether tail is presented to the surrounding refrigerant. On the other hand, the steric layer formed by surface-adsorbed molecules with long chains also amplifies the stabilization process.

Transmission Electron Microscopy

We characterized our dry nanoparticles obtained from commercial vendors by getting Transmission Electron Microscopy (TEM) images and diffraction patterns (DP) of each nanomaterial (see the figures on Page 127-131). These micrographs reveal that nanoparticles are highly agglomerated in dry form. For example, Al₂O₃ nanoparticles have a disk-shaped morphology with characteristic particle sizes in the range of 5–50 nm. The electron diffraction pattern of the selected area with crystallographic planes conforms to the structure of γ -Al₂O₃. The morphology and particle size range of all other nanoparticles with corresponding crystal structures are given in Table C-1, APPENDIX C.

Particle Size Measurements

To connect these observations with the structure in the fluid samples, we measured the sizes of the particles in our suspensions using the Dynamic Light Scattering (DLS) technique. It is a widely used characterization method to determine the size distribution of particles in a solution. The DLS studies done with nanoparticle

suspensions show polydisperse systems, and alumina has the largest particle size with 390 nm (Table 9).

Table 9. Bulk characterization of nanoparticle suspensions (complete datasets are provided in APPENDIX D).

Suspension Composition*	Zeta potential** (mV)	Particle size*** (nm)
Al ₂ O ₃	-35.69 ± 1.78	390.45 ± 28.04
AlN	-42.72 ± 1.43	281.27 ± 18.99
ZnO	-54.37 ± 2.04	212.30 ± 11.77
CuO	-43.22 ± 4.51	143.47 ± 8.33
TiO ₂	-36.63 ± 3.44	77.75 ± 15.16

* All suspensions contain nanoparticles at 0.02 vol% solution except CuO and TiO₂ (0.004 vol%). The K157 concentration was 0.09 vol%.

** Mean ± sd (*n* = 10)

*** Mean ± sd (*n* = 6)

The apparent increase in diameter of particles, determined by DLS as compared to TEM results and primary particle size data provided by the manufacturers, reflects the agglomeration of the particles although ultrasonication and vigorous stirring were applied. Moreover, the presence of polymeric stabilizer around the particles increases the hydrodynamic size of nanoparticles, even as it behaves like a bridge to connect particles.

Zeta Potential Measurements

We employed zeta potential measurements to study the stability characteristics of our refrigerant suspensions. High surface charge density produces strong repulsive forces which help to formulate well-dispersed suspensions. To the best of our

knowledge, this paper is the first attempt to estimate the dispersion characteristics of surfactant-mediated refrigerant suspensions. In order to assess the surface charge on the selected nanoparticles, we performed zeta potential measurements using a ZetaPALS analyzer (Brookhaven Instruments Corp.). This instrument calculates the zeta potential from measured electrophoretic mobility using the Smoluchowski or Huckel equation. The measurements revealed that nanorefrigerant prepared from ZnO has the highest zeta potential value and displays the best stability. The absolute values of the zeta potentials can be arranged in the order of $\text{ZnO} > \text{CuO} \sim \text{AlN} > \text{Al}_2\text{O}_3 \sim \text{TiO}_2$. All zeta potential values of our suspensions are less than -35 mV , thereby suggesting good dispersion systems (Table 9). The interaction of nanoparticle surfaces with the polar head groups of Krytox 157 FSL may cause the formation of negatively charged complexes. The electrostatic repulsion force in such a system is sufficient to prevent attraction among the particles. On the other hand, the relatively low zeta potential of alumina and titania suspensions does not lead to a particle agglomeration problem due to existing steric effects.

7.3 Nanoparticle Effects on Thermal Conductivity of Refrigerant

The surfactant dispersal method allowed us to reliably produce stable suspensions containing TiO_2 , Al_2O_3 , ZnO , CuO , and AlN nanoparticles. We performed a series of transient hot wire measurements at temperatures of $2 \text{ }^\circ\text{C}$, $12 \text{ }^\circ\text{C}$ and $22 \text{ }^\circ\text{C}$ in order to assess the influence of nanoparticles on the thermal conductivity properties of the chosen refrigerant. Figure 46 compares thermal conductivity values of all nanoparticles with respect to particle concentration at each temperature.

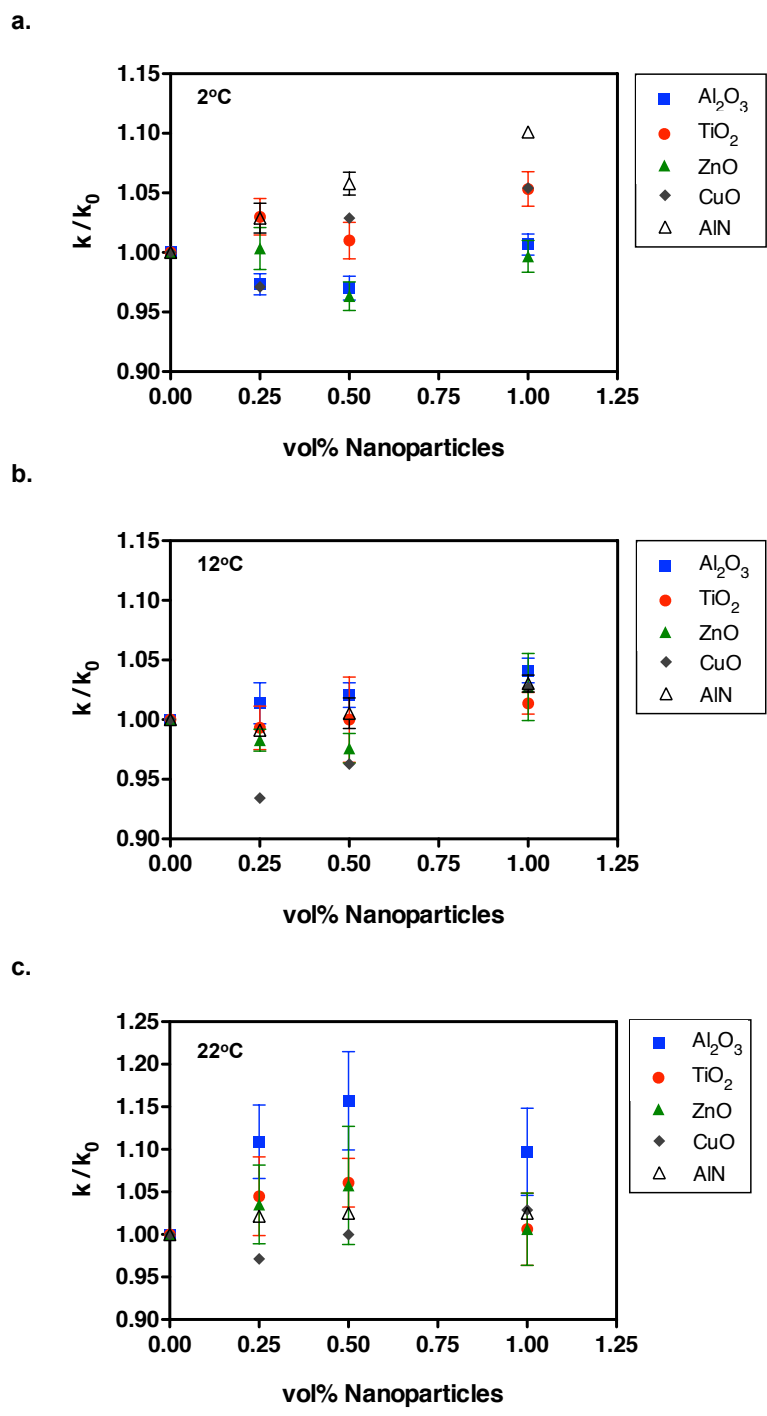


Figure 46. Concentration dependence of thermal conductivity enhancements in refrigerant suspensions containing various nanoparticles (data are expressed relative to the pure refrigerant (particle- and surfactant-free) k/k_0). The Krytox 157 FSL concentration was 1 vol % in all refrigerant suspensions.

Moreover, Figure 47b-51b provides thermal conductivity data specific to the corresponding nanoparticle as a function of temperature. All these graphs indicate that the conductivity changes in these refrigerant suspensions were particle specific and temperature dependent. For example, minimal thermal conductivity enhancements were observed in TiO₂ and CuO-based refrigerant suspensions, although CuO has the highest bulk thermal conductivity after AlN.⁵⁸ On the other hand, Al₂O₃, AlN, and ZnO nanoparticles appreciably altered the conductivity. TiO₂ and CuO particles have much lower average diameter in comparison to other particles according to DLS measurements, therefore there could be a direct relation between particle size, and thermal conductivity other than just particle type.¹⁸³ The effect of Brownian motion is expected to decrease with particle size increase; so severe clustering of nanoparticles in the associated samples would be the responsible mechanism for enhanced conductivity. Moreover, TEM results demonstrate that nanoparticles used in refrigerant suspensions have diverse particle shapes, displaying potential to influence the results (Table C-1, APPENDIX C). Definitive conclusions are difficult to draw here since we lack the material and data of one type of particle with different sizes.

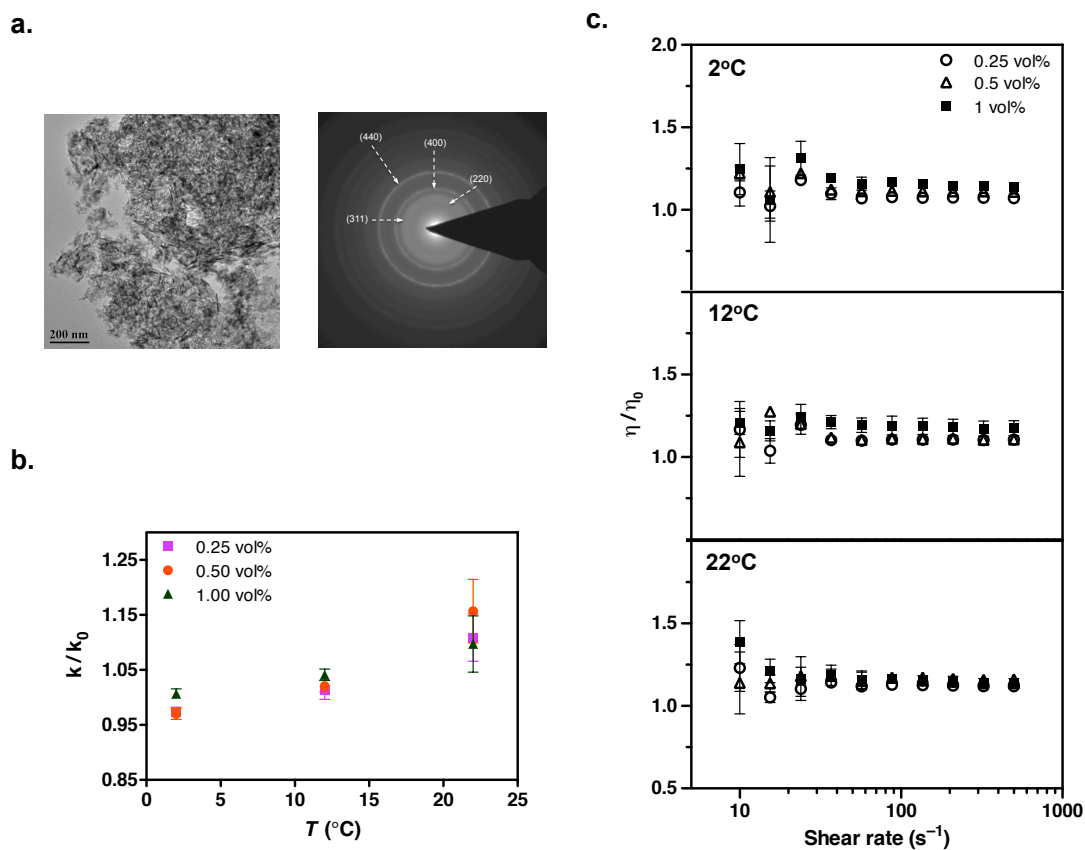


Figure 47. (a) TEM image and the corresponding electron diffraction pattern of Al_2O_3 nanoparticles used to formulate the suspensions. (b) Temperature dependence of thermal conductivity enhancements in refrigerant suspensions containing Al_2O_3 nanoparticles (data are expressed relative to the particle-free case k/k_0). (c) Steady shear viscosity measurements show a little increase at low shear rates (data shown are obtained over a shear rate sweep from 500 to $10 s^{-1}$ after first ramping up from 10 to $500 s^{-1}$ to generate a reproducible initial condition, results are plotted relative to the particle-free case (η/η_0)). Experiments were carried out at constant temperatures ($2^\circ C$, $12^\circ C$ and $22^\circ C$). All refrigerant solutions contained 1 vol% Krytox 157 FSL.

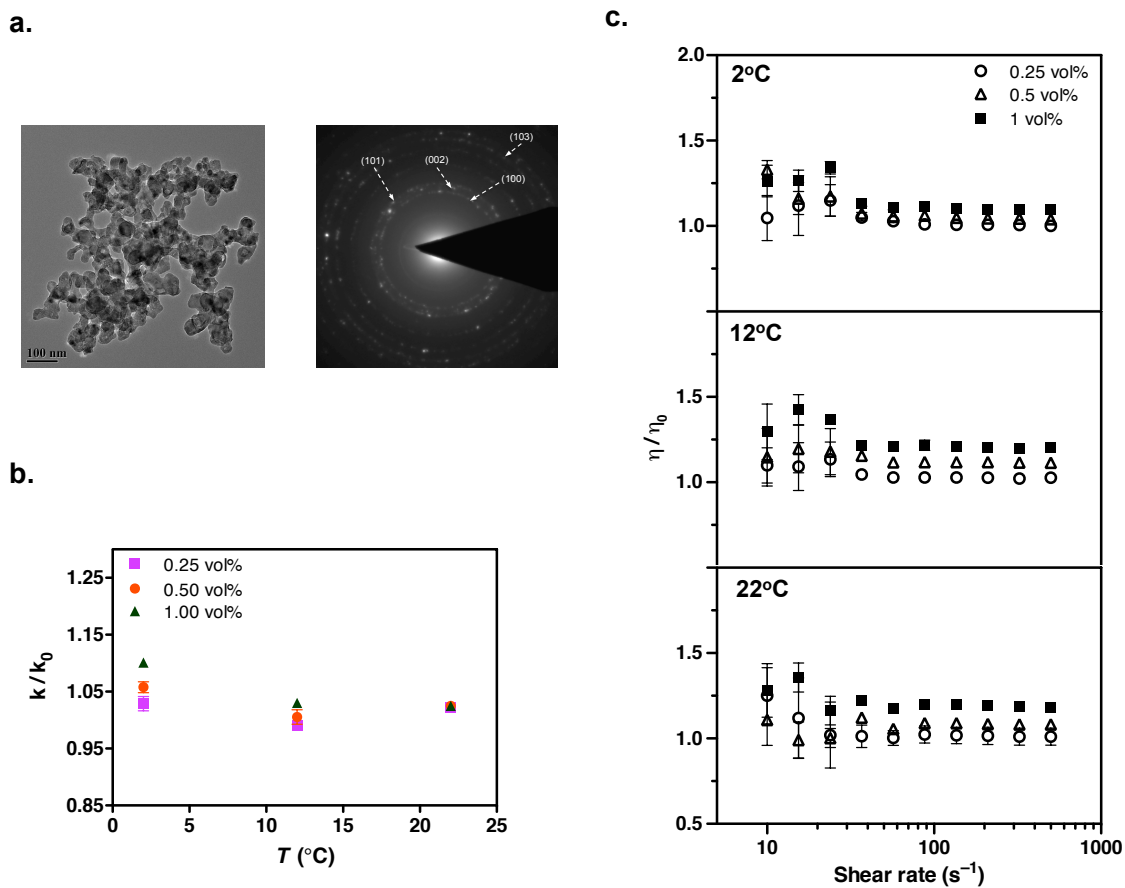


Figure 48. (a) TEM image and the corresponding electron diffraction pattern of dry AlN nanoparticles. (b) Small change in thermal conductivity enhancements at high temperatures. (c) Steady shear viscosity measurements of refrigerant suspensions containing AlN nanoparticles (data are expressed relative to the particle-free case, (η/η_0)). The experiment conditions are the same as that in Al_2O_3 measurements.

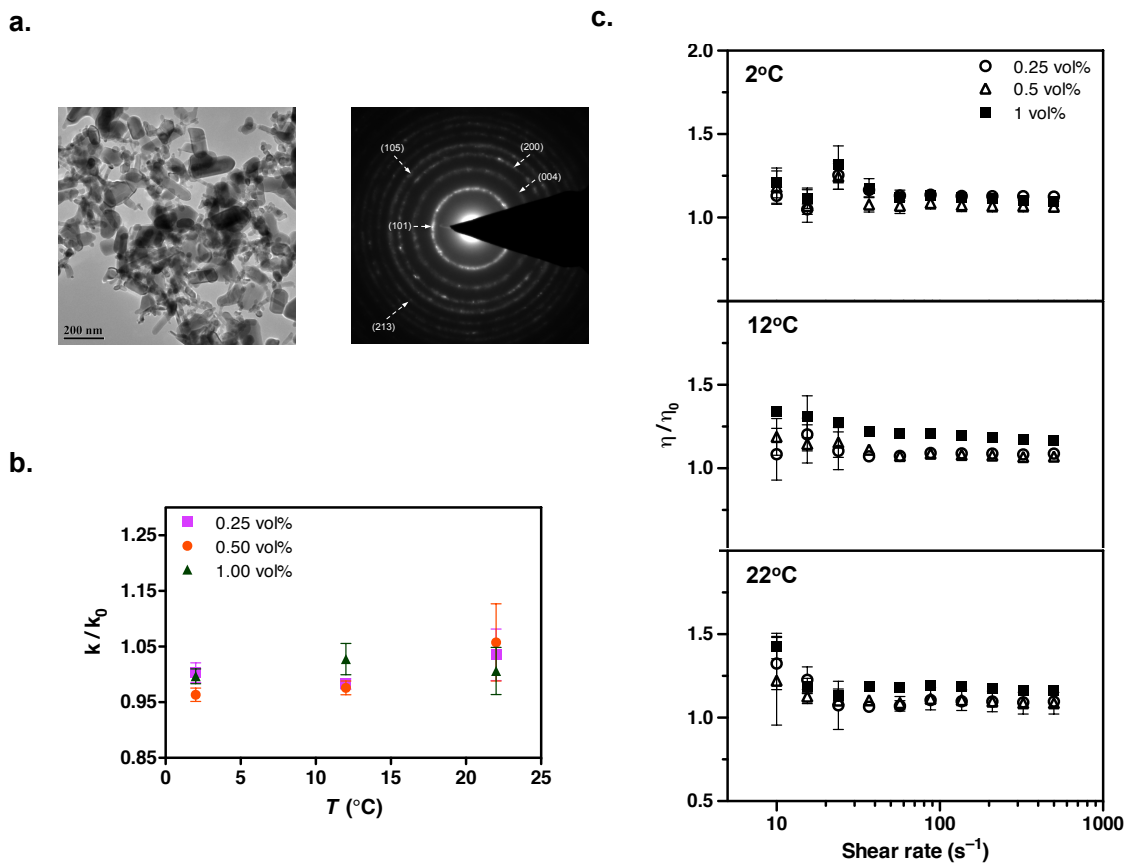


Figure 49. (a) TEM image and the corresponding electron diffraction pattern of dry ZnO nanoparticles. (b) Thermal conductivity of suspensions only show appreciable enhancement at high temperatures. (c) The similar viscosity enhancement trend is observed in steady shear measurements. The experiment conditions are the same as that in Al_2O_3 measurements.

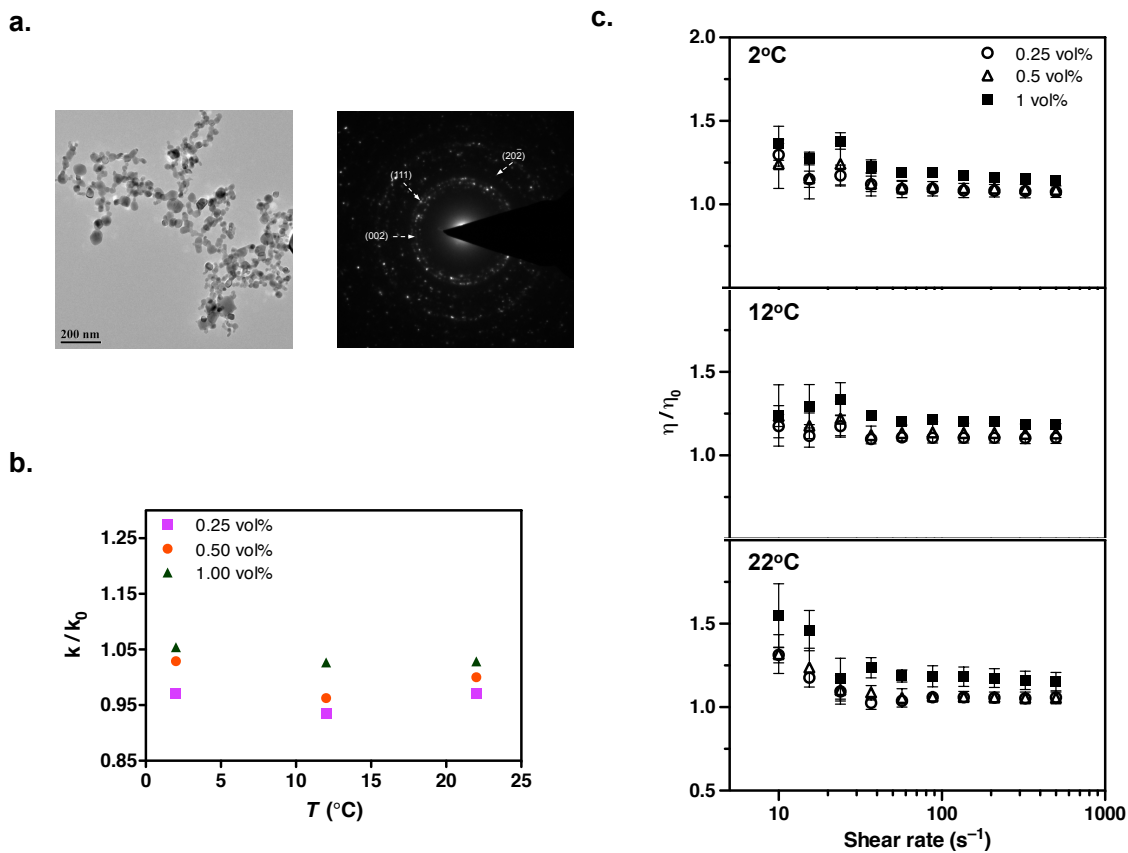


Figure 50. (a) TEM image and the corresponding electron diffraction pattern of dry CuO nanoparticle. (b) Thermal conductivity enhancements in CuO refrigerant suspensions are low as well. (c) The increase in steady shear viscosity measurements at low shear rates is still observed. The experiment conditions are the same as that in Al_2O_3 measurements.

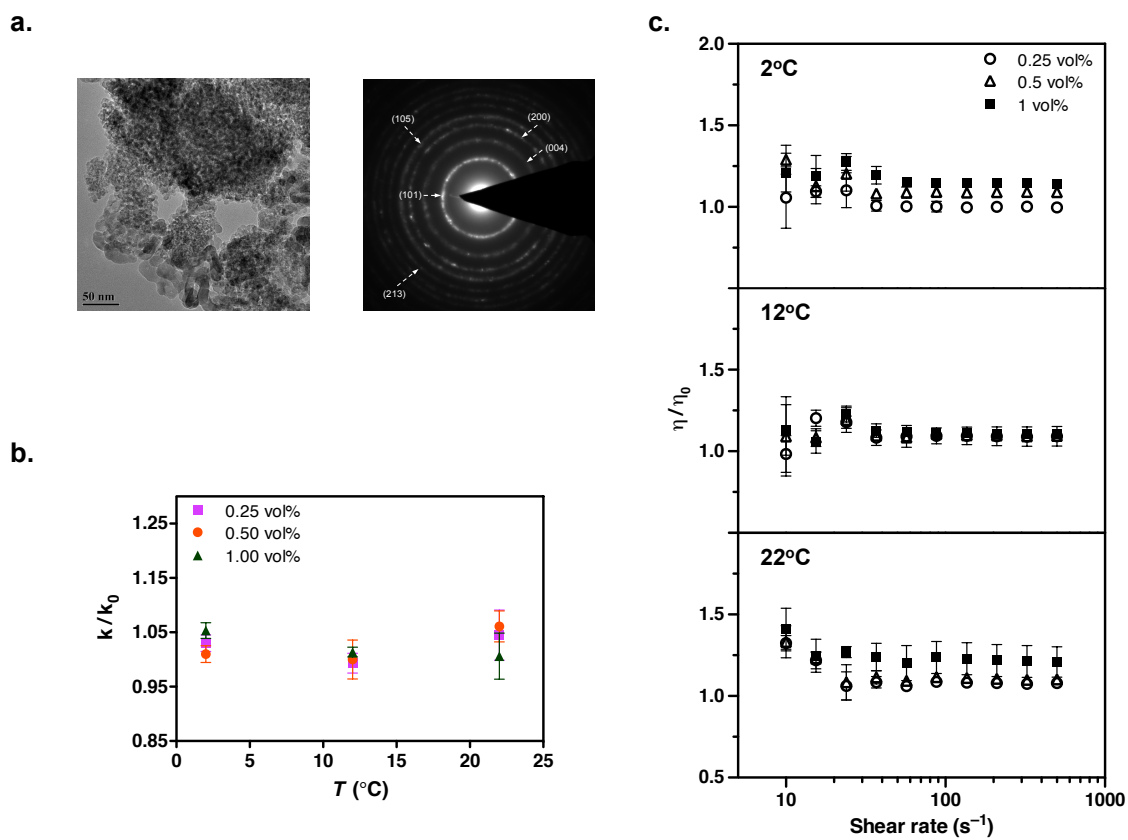


Figure 51. (a) TEM image and the corresponding electron diffraction pattern of dry TiO_2 nanoparticles. (b) The refrigerant suspensions of TiO_2 displayed less than 5% enhancements in thermal conductivity. (c) The remarkable viscosity increase in steady shear viscosity is easily noticed again at low shear rates. The experiment conditions are the same as that in Al_2O_3 measurements.

As we mentioned before, some conductivity enhancement was temperature dependent and observed at low temperatures (2 °C) upon addition of AlN and CuO (the particles with high bulk thermal conductivities). On the other hand, only Al₂O₃ and ZnO suspensions displayed significantly enhanced thermal conductivity at room temperature (~10-15% increase). The effect of surfactant on the measurements was minimal (less than 1%) as seen in Table 7. We briefly summarize our results in Table 10 and compare them with previous related findings involving the same type of nanoparticle suspensions. Although there are no comparable data in the literature regarding nanoparticle-refrigerant suspension systems, our observations are consistent with some of the conductivity enhancements observed in aqueous suspensions. Due to the low thermal conductivity of base fluid (HFE 7500), thermal conductivity ratio is expected to be higher than the aqueous suspensions in keeping with Maxwell model predictions.¹³

Table 10. Summary of thermal characterization studies involving nanoparticles.

Particle Type	Loading	Host Fluid	Temperature	Dispersant	Measurement Method	Key Observations	Ref.
Al ₂ O ₃ , AlN, ZnO, CuO, TiO ₂ ,	0.25-1 vol%	HFE 7500	2 °C, 12 °C, 22 °C	Krytox 157-FSL	Transient hot wire (KD2)	Up to ~ 10 – 15% increase at 22 °C, ~ 10 % increase at 2 °C, ~ 10 % increase at 22 °C, ~ 5% increase at 2 °C ~ 5% increase at 2°C and 22 °C, in thermal conductivity	This work
Al ₂ O ₃	1 vol%	Water	27 °C	Tween 80	–	Up to ~ 7% increase at 27 °C in thermal conductivity	31
Al ₂ O ₃	1 vol%	Water	25 °C	CTAB	Transient hot wire	Up to ~ 12% increase at 25 °C in thermal conductivity	184
AlN	1 vol%	Ethanol	0 °C and 24 °C	Castor oil	Transient plane source	Up to ~ 3% increase at 0 °C, ~ 8% increase at 24 °C in thermal conductivity	181
ZnO	1 vol%	Ethylene Glycol	From 20 °C to 60 °C in 10° increments	–	Transient hot wire	Up to ~ 8-9% increase at 20 °C in thermal conductivity	103
ZnO, TiO ₂	1 vol%	Ethylene Glycol	20 °C	SDS	Transient hot wire	Up to ~ 6% increase at 20 °C, ~ 4 – 5% increase at 20 °C in thermal conductivity	116

Table 10 Continued

Particle Type	Loading	Host Fluid	Temperature	Dispersant	Measurement Method	Key Observations	Ref.
CuO	1 vol%	Ethylene Glycol	25 °C	–	Transient hot wire	Up to ~ 5% increase at 25 °C in thermal conductivity	71
CuO	1 vol%	Water	21 °C, 36 °C, 51 °C	–	Temperature oscillation	Up to ~ 6% increase at 21 °C in thermal conductivity	18
TiO ₂	1 vol%	Water	15 °C, 25 °C, 35 °C	–	Transient hot wire	Up to ~ 4-5% increase at 15°C and 25 °C in thermal conductivity	185
TiO ₂	1 vol%	Water	13 °C, 23 °C, 40 °C, 55 °C	–	3 _w wire	Up to ~ 3% increase at 13 °C and 23 °C in thermal conductivity	186

Our experimental thermal conductivity data was higher than the calculations of existing theoretical models suggested for predicting thermal conductivity enhancements of solid-liquid systems. Maxwell's equation,⁷⁷ which considers only the volume fraction of particles, and the Hamilton and Crosser model⁷⁸ with empirical shape factor underestimate the enhancements seen in our experiments. Koo and Kleinstreuer model^{80, 81}, containing physical properties of components, also predicts the conductivity with less than 5% enhancements (Table 11). The empirical expression proposed by Li and Peterson for k_{eff}/k_f even gave values less than 1.²⁵

Table 11. Theoretical models used for predicting thermal conductivity of nanorefrigerants.

Model	Suggested Formulas	Description
Maxwell ⁷⁷	$\frac{k_{eff}}{k_f} = \frac{k_p + 2k_f + 2(k_p - k_f)\phi}{k_p + 2k_f - 2(k_p - k_f)\phi} *$	For large, spherical and non interacting particles, dilute systems
Hamilton and Crosser ⁷⁸	$\frac{k_{eff}}{k_f} = \frac{k_p + k_f(n-1) + (k_p - k_f)(n-1)\phi}{k_p + k_f(n-1) - (k_p - k_f)\phi} **$	Applicable to cylindrical particles with empirical shape factor
Koo and Kleinstreuer ^{80, 81}	$\frac{k_{eff}}{k_f} = \frac{k_p + 2k_f + 2(k_p - k_f)\phi}{k_p + 2k_f - 2(k_p - k_f)\phi} + 5 \times 10^4 \beta \rho_f C_f \phi \sqrt{\frac{k_B T}{\rho_p D} \frac{f(T, \phi)}{k_f}} ***$	Inclusion of physical properties
Li and Peterson ²⁵	$\frac{k_{eff}}{k_f} = 0.764481464\phi + 0.018688867T + 0.537852825$	Empirical equation with temperature variable

* where k_{eff} , k_p and k_f are the thermal conductivities of the suspension, nanoparticle, and base fluid respectively, ϕ is the suspension volume percentage,

** n is the empirical shape factor, defined as $n = 3/\varphi$. The particle sphericity, φ , is the ratio of the surface area of a sphere to the surface area of the particle and its value for sphere and cylinder is equal to 1 and 0.5 respectively.

*** T is the temperature, ρ_f and C_f are the density and heat capacity of the fluid, ρ_p is the particle density, k_B is the Boltzmann constant (1.381×10^{-23} J/K), D is the particle diameter, T is the temperature, f as a function of volume fraction and temperature can be defined as $f(T, \phi) = (0.4705 - 6.04\phi)T + 1722.3\phi - 134.63$ and β is empirically determined parameter and $\beta = [0.0137(100\phi)^{0.8229}, \phi < 0.01$ and $0.0011(100\phi)^{-0.7272}, \phi > 0.01]$.

Therefore the predictions of these models were found to be approximate estimations of the thermal conductivity enhancements in TiO₂ and CuO suspensions, but not the higher conductivities obtained with ZnO, Al₂O₃, and AlN nanoparticles. There is still a need for satisfactory theoretical models to predict anomalous thermal

conductivities of nanorefrigerants. A more comprehensive model with combined effects of other mechanisms can give better match with experimental results.

7.4 Rheological Behavior of Refrigerant Based Nanoparticle Suspensions

After we observed thermal conductivity changes with nanoparticle addition, we measured steady shear viscosities of the suspensions over the rates from 500 to 10 s⁻¹. The addition of surfactant did not increase the refrigerant viscosity appreciably although it has a polymeric chemical structure (Table 6). We only focused on the low percentage loadings of nanoparticles to refrigerant because the excessive viscosity enhancement may adversely affect fluid properties and not favor for practical implementations.^{94, 187, 188} Our results showed that the relative viscosity of all the nanorefrigerants, defined as the ratio of the nanofluid viscosity (μ) to the viscosity of the particle free pure refrigerant ($\mu_{\text{HFE 7500}}$), gradually increased with the volume fraction of nanoparticles (Figure 47c-51c). This enhancing trend is most clear when observed at high shear rates. The fluctuating viscosity values at low shear rates might be due to the effects of strengthened interparticle interactions at increasing concentrations. Surprisingly, we observed similar behavior at low shear rates for pure refrigerant as well. Therefore we believe that these effects are diminished when ratios are considered, but there still could be an unavoidable impact on the measurements.

Moreover, the suspensions had similar viscosity behavior as a function of temperature, but we could not observe any decreasing trend in viscosity values at elevated temperatures. The shear thinning behavior of nanorefrigerants became

prominent with particle loading at high temperatures. The non-newtonian characteristics of nanofluids containing Al_2O_3 , TiO_2 , AlN , ZnO and CuO have been previously reported when nanoparticle concentrations were above 1 vol%.^{71, 103, 189-191} We could not differentiate the effect of particle shape on viscosity of nanofluids from other factors, although elongate particles like platelets and cylinders were reported to be having higher viscosity values at the same volume fractions.¹⁹² For example, ZnO with rod-like shape do not show significant difference as a viscosity behavior. Although there is no available literature data on nanorefrigerants for direct comparison of rheological behaviors, we prepared a table from previous research results obtained with these nanoparticles (Table 12).

Table 12. Summary of rheological studies involving nanoparticle suspensions.

Particle Type	Loading	Host Fluid	Temperature	Dispersant	Measurement Method	Key Observations	Ref.
Al ₂ O ₃ , AlN, ZnO, CuO, TiO ₂	0.25-1 vol%	HFE-7500	2 °C, 12 °C, 22 °C	Krytox 157-FSL	Parallel plate CP 50-1	Up to ~ 10 - 15% increase, ~ 10 - 18 % increase, ~ 10 - 16 % increase, ~ 15 -18% increase, ~ 15 - 20% increase in viscosity Enhancement as a function of concentration, shear thinning behavior at elevated temperatures and high loadings	This work
Al ₂ O ₃	1 vol%	Decane Polyalphaolefin	22 °C	Sorbitan monolaurate	-	Up to ~ 10% increase	193
Al ₂ O ₃	1 vol%	Engine Coolant (HP KOOLGARD)	10 °C, 20 °C, 30 °C	Oleic acid	Rotational type Spindle	Up to ~ 65-70% increase Shear thinning behavior	189
AlN	5 vol%	Ethylene glycol Propylene Glycol	20 °C	-	Rotational type Spindle SC-18	Up to ~ 76% increase, Up to ~ 72% increase, Shear thinning behavior when $\phi_v > 0.05$	190

Table 12 Continued

Particle Type	Loading	Host Fluid	Temperature	Dispersant	Measurement Method	Key Observations	Ref.
ZnO	2 vol%	Ethylene Glycol	From 20 °C to 60 °C in 10° increments	-	Rotational type Spindle SC-18	Up to ~ 22% increase in viscosity Shear thinning behavior when $\phi_v > 0.02$	103
ZnO	0.6 vol%	Ethylene Glycol	25 °C	Ammonium citrate	Ostwald Viscometer	Up to ~ 26% increase in viscosity	194
CuO	1 vol%	Ethylene Glycol	25 °C	-	Rotational type Couette fixture	Up to ~ 90% increase in viscosity Shear thinning behavior	71
CuO	1 vol%	Ethylene Glycol & Water Mixture	From -35 °C to 50 °C in 10° increments	-	Rotational type Spindle SC-18	Up to ~ 20-25% increase in viscosity Newtonian behavior	195
TiO ₂	1 vol%	Water	15 °C, 25 °C, 35 °C	-	Parallel plate	Up to ~ 17% increase in viscosity	185
TiO ₂	1 vol%	Water	13 °C	-	Vibration Viscometer SV-10	Up to ~ 19% increase in viscosity	186
TiO ₂	1.2 vol%	Water	22 °C	-	Rotational type Couette fixture (Mooney cell)	Up to ~ 11% increase in viscosity Shear thinning behavior	191

We also noticed that the magnitude of viscosity enhancements are significantly higher than the predictions by Einstein⁹⁶, Brinkman⁹⁸ and Batchelor⁹⁹ models because these models are formulated for dilute suspension systems with uniform particle size and shape (Table 13). The relative viscosity values estimated from the modified Krieger and Dougherty model¹⁸⁸ considering the aggregates and particle size are consistent with our experimental values if the related parameters were adjusted for each nanoparticle.

Table 13. Theoretical models used for predicting viscosity variation.

Model	Suggested Formulas*	Description
Einstein ⁹⁶	$\frac{\mu_{eff}}{\mu_f} = 1 + 2.5\phi$	Spherical and non interacting particles, ($\phi < 0.02$)
Brinkman ⁹⁸	$\frac{\mu_{eff}}{\mu_f} = \frac{1}{(1-\phi)^{2.5}}$	Extension of Einstein equation for ($\phi < 0.04$)
Batchelor ⁹⁹	$\frac{\mu_{eff}}{\mu_f} = 1 + 2.5\phi + 6.2\phi^2$	Spherical particles with interaction of pair-particles considering Brownian motion, ($\phi < 0.1$)
Modified Krieger and Dougherty ¹⁸⁸	$\frac{\mu_{eff}}{\mu_f} = \left(1 - \frac{\phi_a}{\phi_m}\right)^{-2.5\phi_m}$ $\phi_a = \phi \left(\frac{a_a}{a}\right)^{3-D}$	Aggregation of particles, full range of ϕ

* where μ_{eff} and μ_f are the viscosities of the suspension and base fluid, ϕ is the suspension volume percentage, a and a_m are the radii of aggregates and primary particles. ϕ_m is the maximum particle packing fraction, which varies from 0.495 to 0.54 under quiescent conditions, and is approximately 0.605 at high shear rates. D is the fractal index having a typical value of 1.8 for nanofluids.

7.5 Final Remarks

Our study represents systematic analyses of physical and thermal properties of nanofluids containing nanoparticles dispersed in a commercial refrigerant host fluid. We hypothesize that the electrosteric stabilization mechanism existing in colloidal systems could enable the formation of well-dispersed nanorefrigerants. We present an accessible standardized experiment methodology that addresses the unique challenges posed by the study of nanofluids' thermal conductivity. Our findings indicate that thermal conductivity values of nanoparticle suspensions depend on the particle type, concentration and temperature of the base fluid. This unified approach can be readily adopted in any research lab, and may help enable improved reproducibility so that more meaningful comparisons can be made among data in published literature. The steady shear viscosity measurements also show significant enhancements due to the presence of particle in the system especially at low shear rates. This perceived increase in viscosity may limit the potential applications of these nanorefrigerants in related heat transfer systems. All of the conducted measurements are instrumental in assessing the potential for nanorefrigerants prepared from commercially available constituents to function as advanced heat transfer fluids.

8. CONCLUSIONS AND FUTURE WORK

8.1 Conclusions

In this research, we address the mass transport properties of low volume fraction colloidal nanoparticle suspensions (nanofluids) by employing a microfluidic approach that allows us to directly monitor diffusion of tracer dyes between nanofluid streams as they flow through a microchannel network. The diffusion coefficients of tracer dyes are precisely measured due to the existing laminar flow field in the microchannel, and the interactions among the constituents of the suspension including the dye, suspended nanoparticles, and surfactant are readily studied. In our experiments, we unexpectedly observe the spontaneous formation of highly focused and intensely fluorescent plumes at the interface between fluid streams suggesting strong interactions between fluorescein and alumina nanoparticles under the conditions matching previously reported study done by KBPP. The extraction of meaningful diffusivity measurements from our lateral fluorescein concentration profile becomes impossible as well. These adsorption-complexation phenomena existing among dye and Tween 80 stabilized alumina particle was incorrectly interpreted as an anomalous diffusion enhancement in KBPP results because anomalous dye diffusion in their study with irregularly shaped pattern was also characterized by intensely fluorescent thread-like regions superimposed over a nebulous background cloud of much lower intensity. When this interplay is minimized matching dye-surfactant charge with an alternative dye-surfactant couple (sds-rose bengal) system,

no significant variance in diffusivity of rose bengal in the presence of alumina nanofluid is noted. This research work has demonstrated that any failure to properly consider the multiplicity of interactions at play among the species comprising colloidal nanomaterials can lead to incorrect conclusions about their effects on mass and heat transfer.

In Chapter 5, these aforementioned interactions between the tracer dye and other components comprising the suspension are deeply focused on. We compare the alumina nanofluids' stability over an ensemble of two fluorescent dyes (Rhodamine 6G and Rose Bengal) with different ionic characteristics and a surfactant in conjunction with coordinated measurements of zeta potential, particle size, steady shear viscosity and bulk thermal conductivity. We describe a simple microfluidic test tool that enables stability of alumina nanoparticle suspensions to be readily assessed by establishing a confinement-imposed chemical discontinuity at the interface between co-flowing laminar streams in a microchannel. The colloidal suspensions are extremely susceptible to aggregation and sedimentation in response to small compositional perturbations due to their metastable nature. This method readily reveals these undesired compositions, even when conventional bulk measurements suggest only subtle differences between formulations. Our results also show what properties of tracer dyes (solubility and relative charge) need to be checked in order to yield stable suspensions. Although the microchannel-based experiment may not provide information at a level suitable for detailed fundamental study, it nevertheless offers a simple and powerful method to quickly characterize a complex suspension's susceptibility to aggregation under specific conditions relevant to many practical applications including tracer-based studies.

In Chapter 6 and 7, the dispersion characteristics of some nanomaterials (graphene nanosheets, multi-wall carbon nanotubes, and metal oxide and nitride nanoparticles) into a commercial hydrofluoroether (HFE 7500) host refrigerant is investigated by applying a Krytox 157-mediated dispersal method. From zeta potential measurements, we surmise that the electrosteric stabilization mechanism existing in colloidal systems could enable the formation of well-dispersed nanorefrigerants. Then the effects of material properties and temperature on the refrigerant thermal conductivity are examined by using a reliable standard protocol based on transient hot wire technique. This unified approach can be readily adopted in any research lab, and may help enable improved reproducibility so that more meaningful comparisons can be made among data in published literature.

Our findings indicate a 10-15% increase in thermal conductivity, which strongly depends on the particle type, concentration, and temperature of the base fluid. Graphene nanosheets uniquely match the superior thermal conductivity enhancements attained in carbon nanotube suspensions without the accompanying penalty of a large viscosity increase and lay a foundation to easily achieve increased efficiency in many thermal management applications. On the other hand, only Al_2O_3 nanoparticles among the other nanoparticles displayed appreciable thermal conductivity enhancement due to the greater particle size, but significant increase in viscosity may limit the applications of these nanoparticle laden refrigerants. The rise in thermal conductivity and viscosity could be accounted for nanoclustering effects. All of the conducted measurements are

instrumental in assessing the potential for nanorefrigerants prepared from commercially available constituents to function as advanced heat transfer fluids.

8.2 Future Work

The Nanoparticle Detection Using The Microfluidic System

Based on the results of this research, it has been confirmed that the microfluidic format offers a unique approach to locally isolate and probe the interactions among dye, surfactant and nanoparticle. While we know that a distinct fluorescence signal is generated instantaneously in the presence of nanoparticles, we have not yet explored the range of particle concentrations that can be detected or how the signal changes with particle size and composition. Having established the sensitivity and detection limits of the microfluidic-based method, the refinements that enable the ability to distinguish different nanoparticle compositions can be explored.

These interactions can potentially be harnessed to enable entirely new capabilities (e.g., for chromatography and other adsorption-based analysis). We have recently discovered that interfacial fluorescence quenching can also occur when the nanoparticles are of different composition. The quenching effect of semiconductor TiO_2 in a microchannel set-up in contrast to the fluorescence enhancement effect of Al_2O_3 is also observed (Figure E-1, APPENDIX E). This is an exciting result because it introduces the possibility to selectively detect different nanoparticle species depending on a fluorescence intensity signal. The fluorometer data obtained with a Spectrofluorometer for characterizing spectral response with and without addition of

fluorescein dye also consolidated this phenomena displaying perceptible fluorescence behavior (Figure E-2, APPENDIX E).

It would be also a wise idea to utilize these interactions as a tool in a microfluidic system to detect the unknown nanoparticle component in the composition of a stream. I and other colleagues are now building on this foundation by performing studies that will help us to understand how to couple nanoparticle suspension and fluorescent dye to produce a new platform for automated continuous real time environmental sampling and detection of airborne engineered nanomaterials (Figure F-1, APPENDIX F). Incoming experiment results can give much more important clues for understanding the phenomena in this system and identifying the opportunities in the field of chemosensors and fluorescent labels for future research.

The Various Approaches and Directions on The Nanorefrigerant Studies

The experimental investigations on nanorefrigerants can be extended to the next level by exploring on the nanomaterial synthesis. In our studies, commercially obtained nanomaterial powders are used. On the other hand, being able to consistently control the material properties from synthesis to application make it possible to establish important connections between the manufacturing process and the thermal performance of the resulting suspension. This new knowledge is critical to rationally engineer nanomaterials (e.g., of controlled size and morphology (sphere, tube, rod, wire, plate, complex-shaped, etc.)) that optimally enhance nanorefrigerant properties. The full structural characterization of nanomaterials before dispersion is a good starting point. The facile in

situ synthesis of surfactant free nanorefrigerants could be an evolution in this scope by precluding the unfavorable effects of surfactant (thermal resistance at nanoparticle-fluid interface) on thermal conductivity and heat transfer coefficient measurements.

There may be some other surfactant-involved recipes for nanorefrigerant formulation. The first formulation approach involves establishing a weak micro/nano structure by mixing alumina or any metal oxide nanoparticles with boron nitride, graphene nanosheets or carbon nanotubes. This colloidal system could produce a transient network that continually breaks and reforms during flow to keep the viscosity low. At any instant in time there would be a dynamic heat conduction path through the structures that would enable enhanced heat transport without a substantial viscosity increase. Another variation of these aforementioned structures could be to engineer a stronger chemical functionalization between the nanomaterials and surfactant. A wormy micelle network can be produced by surfactant incorporating nanosheets and nanoparticles at the same time.

The next logical step in the progression is to employ these fluids in boiling heat transfer applications at various experiment conditions and analyze how presence and migration behavior of the nanomaterials affect the transport process. The interactions and influence of surfactant additives and refrigerant oil on the colloidal suspension characteristics and refrigeration system can be examined as well.

Nanorefrigerant efficacy can only be considered through physical and thermal property evaluations. The viscosity and density should be maintained as low as possible by an accurate selection of material type, shape, and size in order to avoid the penalty in

pressure drop. The lowered production cost of nanorefrigerants is also crucial at this stage. The agglomeration state of nanorefrigerants and the sedimentation need to be carefully characterized in direct correlation with any property measurement. In order to commercialize nanorefrigerants, erosion and settling issues over the long term should be solved.

REFERENCES

1. Kumar, A.; Vemula, P. K.; Ajayan, P. M.; John, G. *Nature Materials* **2008**, 7, (3), 236-241.
2. Lewis, J. *Journal of the American Ceramic Society* **2004**, 83, (10), 2341-2359.
3. Davis, M. *Nature Reviews Drug Discovery* **2008**, 7, (9), 771-782.
4. Yabe, S.; Sato, T. *Journal of Solid State Chemistry* **2003**, 171, (1-2), 7-11.
5. Mezzenga, R.; Schurtenberger, P.; Burbidge, A.; Michel, M. *Nature Materials* **2005**, 4, (10), 729-740.
6. Ahuja, A. S. *J Appl Phys* **1975**, 46, (8), 3408-3416.
7. Ahuja, A. S. *J Appl Phys* **1975**, 46, (8), 3417-3425.
8. Liu, K.; Choi, U.; Kasza, K. *Measurements of Pressure Drop and Heat Transfer in Turbulent Pipe Flows of Particulate Slurries*; Argonne National Lab., IL (USA): 1988.
9. Das, S. K.; Choi, S. U. S.; Yu, W.; Pradeep, T., *Nanofluids: Science and Technology*. John Wiley & Sons, Inc.: Hoboken, NJ, 2008.
10. Eastman, J. A.; Choi, S. U. S.; Li, S.; Yu, W.; Thompson, L. J. *Appl Phys Lett* **2001**, 78, (6), 718-720.
11. Jang, S. P.; Choi, S. U. S. *Applied Thermal Engineering* **2006**, 26, (17-18), 2457-2463.
12. Das, S.; Putra, N.; Roetzel, W. *International Journal of Heat and Mass Transfer* **2003**, 46, (5), 851-862.
13. Wang, X.; Xu, X.; Choi, S. *Journal of Thermophysics and Heat Transfer* **1999**, 13, (4), 474-480.
14. Wasan, D. T.; Nikolov, A. D. *Nature* **2003**, 423, 156-159.
15. Tzeng, S.; Lin, C.; Huang, K. *Acta Mechanica* **2005**, 179, (1), 11-23.

16. Tsai, C. Y.; Chien, H. T.; Ding, P. P.; Chan, B.; Luh, T. Y.; Chen, P. H. *Materials Letters* **2004**, 58, (9), 1461-1465.
17. Eastman, J. A.; Phillpot, S. R.; Choi, S. U. S.; Keblinski, P. *Annual Review of Materials Research* **2004**, 34, (1), 219-246.
18. Das, S. K.; Putra, N.; Thiesen, P.; Roetzel, W. *Journal of Heat Transfer* **2003**, 125, (4), 567-574.
19. Xie, H.; Wang, J.; Xi, T.; Liu, Y.; Ai, F.; Wu, Q. *J Appl Phys* **2002**, 91, (7), 4568-4572.
20. Patel, H.; Das, S.; Sundararajan, T.; Nair, A.; George, B.; Pradeep, T. *Appl Phys Lett* **2003**, 83, 2931.
21. Chon, C.; Kihm, K.; Lee, S.; Choi, S. *Appl Phys Lett* **2005**, 87, 153107.
22. Murshed, S. M. S.; Leong, K. C.; Yang, C. *Int J Therm Sci* **2005**, 44, (4), 367-373.
23. Xuan, Y.; Li, Q. *International Journal of Heat and Fluid Flow* **2000**, 21, (1), 58-64.
24. Assael, M.; Chen, C.; Metaxa, I.; Wakeham, W. *Int J Thermophys* **2004**, 25, (4), 971-985.
25. Li, C.; Peterson, G. *J Appl Phys* **2006**, 99, 084314.
26. Murshed, S.; Leong, K.; Yang, C. *Applied Thermal Engineering* **2008**, 28, (17-18), 2109-2125.
27. Lee, S.; Choi, S.; Li, S.; Eastman, J. *Journal of Heat Transfer* **1999**, 121, 280-289.
28. Pak, B.; Cho, Y. *Experimental Heat Transfer* **1998**, 11, (2), 151-170.
29. Wen, D.; Ding, Y. *Journal of Nanoparticle Research* **2005**, 7, (2), 265-274.
30. Wen, D. S.; Ding, W. *Ieee T Nanotechnol* **2006**, 5, (3), 220-227.
31. Krishnamurthy, S.; Bhattacharya, P.; Phelan, P. E.; Prasher, R. S. *Nano Letters* **2006**, 6, (3), 419-423.
32. Dooley, B.; Warncke, A.; Gharib, M.; Tryggvason, G. *Experiments in Fluids* **1997**, 22, (5), 369-374.

33. Shankar, P.; Kumar, M. *Physics of Fluids* **1995**, 7, 737.
34. Fang, X.; Xuan, Y.; Li, Q. *Appl Phys Lett* **2009**, 95, (20), 203108.
35. Veilleux, J.; Coulombe, S. *J Appl Phys* **2010**, 108, (10), 104316.
36. Samouhos, S. V. Nano-materials for Novel Magneto-Rheological Liquids and Nano-fluids. M.S. Thesis, Massachusetts Institute of Technology, Cambridge, MA, 2007.
37. Gerardi, C.; Cory, D.; Buongiorno, J.; Hu, L. *Transactions of the American Nuclear Society* **2007**, 96, 485-486.
38. Ozturk, S.; Hassan, Y. A.; Ugaz, V. M. *Nano Letters* **2010**, 10, (2), 665-671.
39. Atencia, J.; Beebe, D. *Nature* **2004**, 437, (7059), 648-655.
40. Dominguez-Ontiveros, E.; Fortenberry, S.; Hassan, Y. A. *Nuclear Engineering and Design* **2010**, 240, (2), 299-304.
41. Zhu, D.; Li, X.; Wang, N.; Wang, X.; Gao, J.; Li, H. *Current Applied Physics* **2009**, 9, (1), 131-139.
42. Sato, Y.; Irisawa, G.; Ishizuka, M.; Hishida, K.; Maeda, M. *Measurement Science and Technology* **2003**, 14, 114-121.
43. Meinhart, C.; Wereley, S.; Santiago, J. *Experiments in Fluids* **1999**, 27, (5), 414-419.
44. Devasenathipathy, S.; Santiago, J. G.; Takehara, K. *Analytical Chemistry* **2002**, 74, (15), 3704-3713.
45. Bohl, D.; Koochesfahani, M.; Olson, B. *Experiments in Fluids* **2001**, 30, (3), 302-308.
46. Sakakibara, J.; Adrian, R. *Experiments in Fluids* **1999**, 26, (1), 7-15.
47. Hu, H.; Koochesfahani, M.; Lum, C. *Experiments in Fluids* **2006**, 40, (5), 753-763.
48. Genina, E.; Bashkatov, A.; Sinichkin, Y.; Kochubey, V.; Lakodina, N.; Altshuler, G.; Tuchin, V. *Journal of Biomedical Optics* **2002**, 7, 471.
49. Sudarsan, A.; Ugaz, V. *Proceedings of the National Academy of Sciences of the United States of America* **2006**, 103, (19), 7228-7233.

50. Stroock, A. D.; Dertinger, S. K. W.; Ajdari, A.; Mezic, I.; Stone, H. A.; Whitesides, G. M. *Science* **2002**, 295, (5555), 647-651.
51. Wunsch, C.; Ferrari, R. *Annual Review of Fluid Mechanics* **2004**, 36, (1), 281-314.
52. Sabatini, D. A.; Alaustin, T. *Ground Water* **1991**, 29, (3), 341-345.
53. Henderson, K.; Park, Y.-G.; Liu, L.; Jacobi, A. M. *International Journal of Heat and Mass Transfer* **2010**, 53, (5-6), 944-951.
54. Bi, S.; Shi, L.; Zhang, L. *Applied Thermal Engineering* **2008**, 28, (14-15), 1834-1843.
55. Peng, H.; Ding, G.; Jiang, W.; Hu, H.; Gao, Y. *International Journal of Refrigeration* **2009**, 32, (6), 1259-1270.
56. Kim, P.; Shi, L.; Majumdar, A.; McEuen, P. L. *Phys Rev Lett* **2001**, 87, (21).
57. Choi, S. U. S.; Eastman, J. A., Enhancing Thermal Conductivity of Fluids with Nanoparticles. In *ASME International Mechanical Congress and Exhibition*, San Francisco, CA, 1995.
58. Hwang, Y.; Lee, J. K.; Lee, C. H.; Jung, Y. M.; Cheong, S. I.; Lee, C. G.; Ku, B. C.; Jang, S. P. *Thermochimica Acta* **2007**, 455, (1-2), 70-74.
59. Lee, J.; Mudawar, I. *International Journal of Heat and Mass Transfer* **2007**, 50, (3-4), 452-463.
60. Chein, R.; Chuang, J. *Int J Therm Sci* **2007**, 46, (1), 57-66.
61. Xuan, Y. M. *Heat Mass Transfer* **2009**, 46, (2), 277-279.
62. Turanov, A.; Tolmachev, Y. *Heat Mass Transfer* **2009**, 45, (12), 1583-1588.
63. Olle, B.; Bucak, S.; Holmes, T.; Bromberg, L.; Hatton, T.; Wang, D. *Industrial and Engineering Chemistry Research* **2006**, 45, (12), 4355-4363.
64. Zhu, H.; Shanks, B.; Heindel, T. *Industrial and Engineering Chemistry Research* **2008**, 47, (20), 7881-7887.
65. Kim, J.; Jung, J.; Kang, Y. *International Journal of Refrigeration* **2006**, 29, (1), 22-29.
66. Kim, J.; Jung, J.; Kang, Y. *International Journal of Refrigeration* **2007**, 30, (1), 50-57.

67. Lee, J.; Kim, H.; Kim, M.; Koo, J.; Kang, Y. *Journal of Nanoscience and Nanotechnology* **2009**, 9, (12), 7456-7460.
68. Kang, Y. T.; Kim, H. J.; Lee, K. I. *International Journal of Refrigeration* **2008**, 31, (5), 850-856.
69. Lee, J. K.; Koo, J.; Hong, H.; Kang, Y. T. *International Journal of Refrigeration* **2010**, 33, (2), 269-275.
70. Yang, B.; Han, Z. H. *Appl Phys Lett* **2006**, 89, (8).
71. Kwak, K.; Kim, C. *Korea-Australia Rheology Journal* **2005**, 17, (2), 35-40.
72. Murshed, S.; Leong, K.; Yang, C. *Int J Therm Sci* **2008**, 47, (5), 560-568.
73. Haynes, W. M., *CRC Handbook of Chemistry and Physics*. 91st ed.; Taylor & Francis, Inc.: Boca Raton, FL, 2010.
74. Lee, D.; Kim, J.; Kim, B. *Journal of Physical Chemistry B* **2006**, 110, (9), 4323-4328.
75. Assael, M.; Metaxa, I.; Arvanitidis, J.; Christofilos, D.; Lioutas, C. *Int J Thermophys* **2005**, 26, (3), 647-664.
76. Buongiorno, J.; Venerus, D. C.; Prabhat, N.; McKrell, T.; Townsend, J.; Christianson, R.; Tolmachev, Y. V.; Keblinski, P.; Hu, L.-w.; Alvarado, J. L.; Bang, I. C.; Bishnoi, S. W.; Bonetti, M.; Botz, F.; Cecere, A.; Chang, Y.; Chen, G.; Chen, H.; Chung, S. J.; Chyu, M. K.; Das, S. K.; Paola, R. D.; Ding, Y.; Dubois, F.; Dzido, G.; Eapen, J.; Escher, W.; Funfschilling, D.; Galand, Q.; Gao, J.; Gharagozloo, P. E.; Goodson, K. E.; Gutierrez, J. G.; Hong, H.; Horton, M.; Hwang, K. S.; Iorio, C. S.; Jang, S. P.; Jarzebski, A. B.; Jiang, Y.; Jin, L.; Kabelac, S.; Kamath, A.; Kedzierski, M. A.; Kieng, L. G.; Kim, C.; Kim, J.-H.; Kim, S.; Lee, S. H.; Leong, K. C.; Manna, I.; Michel, B.; Ni, R.; Patel, H. E.; Philip, J.; Poulikakos, D.; Reynaud, C.; Savino, R.; Singh, P. K.; Song, P.; Sundararajan, T.; Timofeeva, E.; Tritcak, T.; Turanov, A. N.; Vaerenbergh, S. V.; Wen, D.; Witharana, S.; Yang, C.; Yeh, W.-H.; Zhao, X.-Z.; Zhou, S.-Q. *J Appl Phys* **2009**, 106, (9), 094312.
77. Maxwell, J. C., *A Treatise on Electricity and Magnetism*. 2nd ed.; Clarendon Press: Oxford, UK, 1881.
78. Hamilton, R.; Crosser, O. *Industrial & Engineering Chemistry Fundamentals* **1962**, 1, (3), 187-191.

79. Nan, C.; Birringer, R.; Clarke, D.; Gleiter, H. *J Appl Phys* **1997**, 81, (10), 6692-6699.
80. Koo, J.; Kleinstreuer, C. *Journal of Nanoparticle Research* **2004**, 6, (6), 577-588.
81. Koo, J.; Kleinstreuer, C. *International Journal of Heat and Mass Transfer* **2005**, 48, (13), 2652-2661.
82. Prasher, R.; Bhattacharya, P.; Phelan, P. *Journal of Heat Transfer* **2006**, 128, 588.
83. Prasher, R.; Phelan, P.; Bhattacharya, P. *Nano Letters* **2006**, 6, (7), 1529.
84. Wang, B.-X.; Zhou, L.-P.; Peng, X.-F. *International Journal of Heat and Mass Transfer* **2003**, 46, (14), 2665-2672.
85. Hong, K.; Hong, T.; Yang, H. *Appl Phys Lett* **2006**, 88, 031901.
86. Yu, W.; Choi, S. *Journal of Nanoparticle Research* **2004**, 6, (4), 355-361.
87. Xue, Q. *Physics Letters A* **2003**, 307, (5-6), 313-317.
88. Xuan, Y.; Li, Q.; Hu, W. *AIChE Journal* **2003**, 49, (4), 1038-1043.
89. Ding, Y.; Alias, H.; Wen, D.; Williams, R. A. *International Journal of Heat and Mass Transfer* **2006**, 49, (1-2), 240-250.
90. Xuan, Y. M.; Li, Q. *Journal of Heat Transfer-Transactions of the Asme* **2003**, 125, (1), 151-155.
91. Putra, N.; Roetzel, W.; Das, S. K. *Heat Mass Transfer* **2003**, 39, (8-9), 775-784.
92. Trisaksri, V.; Wongwises, S. *International Journal of Heat and Mass Transfer* **2009**, 52, (5-6), 1582-1588.
93. Zeinali Heris, S.; Etemad, S. G.; Nasr Esfahany, M. *International Communications in Heat and Mass Transfer* **2006**, 33, (4), 529-535.
94. Chen, H.; Yang, W.; He, Y.; Ding, Y.; Zhang, L.; Tan, C.; Lapkin, A.; Bavykin, D. *Powder Technology* **2008**, 183, (1), 63-72.
95. Davis, V.; Ericson, L.; Parra-Vasquez, A.; Fan, H.; Wang, Y.; Prieto, V.; Longoria, J.; Ramesh, S.; Saini, R.; Kittrell, C. *Macromolecules* **2004**, 37, (1), 154-160.
96. Einstein, A. *Annalen Der Physik* **1906**, 19, 289-306.

97. Prasher, R.; Song, D.; Wang, J.; Phelan, P. *Appl Phys Lett* **2006**, 89, (13), 133108.
98. Brinkman, H. *The Journal of Chemical Physics* **1952**, 20, 571.
99. Batchelor, G. *Journal of Fluid Mechanics* **1977**, 83, 97-117.
100. Maiga, S.; Nguyen, C.; Galanis, N.; Roy, G. *Superlattices and Microstructures* **2004**, 35, (3-6), 543-557.
101. Tseng, W.; Lin, K. *Materials Science and Engineering A* **2003**, 355, (1-2), 186-192.
102. Savithiri, S.; Pattamatta, A.; Das, S. K. *Nanoscale Research Letters* **2011**, 6.
103. Yu, W.; Xie, H. Q.; Chen, L. F.; Li, Y. *Thermochimica Acta* **2009**, 491, (1-2), 92-96.
104. Jiang, W.; Ding, G.; Peng, H. *Int J Therm Sci* **2009**, 48, (6), 1108-1115.
105. Jwo, C. S.; Jeng, L. Y.; Chang, H.; Teng, T. P. *Rev Adv Mater Sci* **2008**, 18, 660-666.
106. Naphon, P.; Thongkum, D.; Assadamongkol, P. *Energ Convers Manage* **2009**, 50, (3), 772-776.
107. Park, K. J.; Jung, D. *Energy and Buildings* **2007**, 39, (9), 1061-1064.
108. Vargaftik N. B.; Filippov L. P.; Tarzimanov A. A.; Totiskii E. E., *Handbook of Thermal Conductivity of Liquids and Gases*. CRC Press: Boca Raton, FL, 1994.
109. Raghu, G.; Hongwei, S.; Pengtao, W.; Majid, C.; Fan, G.; Zhiyong, G.; Bridgette, B. *Advances in Mechanical Engineering* **2010**, 2010.
110. Rosen, M. J., *Surfactants and Interfacial Phenomena*. 3rd ed.; John Wiley & Sons, Inc.: Hoboken, NJ, 2004.
111. Tantra, R.; Schulze, P.; Quincey, P. *Particuology* **2010**, 8, (3), 279-285.
112. 3M Novec 7500 Engineered Fluid. Division, E. M. M., Ed. 3M: St Paul, MN, 2010.
113. Choi, S.; Zhang, Z.; Yu, W.; Lockwood, F.; Grulke, E. *Appl Phys Lett* **2001**, 79, (14), 2252-2254.

114. Sudarsan, A. P.; Wang, J.; Ugaz, V. M. *Analytical Chemistry* **2005**, 77, (16), 5167-5173.
115. Munro, M. *Journal of the American Ceramic Society* **1997**, 80, (8), 1919-1928.
116. Kim, S. H.; Choi, S. R.; Kim, D. *Journal of Heat Transfer* **2007**, 129, (3), 298-307.
117. Slack, G. *Physical Review B* **1972**, 6, (10), 3791-3800.
118. Slack, R.; Glen, A.; Vandersande, J. *Journal of Physics and Chemistry of Solids* **1987**, 48, (7), 641-647.
119. Tang, A.-M.; Cui, Y.-J.; Le, T.-T. *Applied Clay Science* **2008**, 41, (3-4), 181-189.
120. Ge, R.; Hardacre, C.; Nancarrow, P.; Rooney, D. W. *Journal of Chemical & Engineering Data* **2007**, 52, (5), 1819-1823.
121. Taha-Tijerina, J.; Narayanan, T. N.; Gao, G.; Rohde, M.; Tsentalovich, D. A.; Pasquali, M.; Ajayan, P. M. *ACS Nano* **2012**, 6, (2), 1214-1220.
122. Carslaw, H. S.; Jaeger, J. C., *Conduction of Heat in Solids*. 2nd ed.; Clarendon Press, Oxford: London, 1959.
123. Kluitenberg, G. J.; Ham, J. M.; Bristow, K. L. *Soil Science Society of America Journal* **1993**, 57, (6), 1444-1451.
124. Tuma, P. E. *Chem Process* **2001**, 64, (2), 47-50.
125. Gibbs, B. F.; Kermasha, S.; Alli, I.; Mulligan, C. N. *International Journal of Food Sciences and Nutrition* **1999**, 50, (3), 213 - 224.
126. Nel, A. E.; Madler, L.; Velegol, D.; Xia, T.; Hoek, E. M. V.; Somasundaran, P.; Klaessig, F.; Castranova, V.; Thompson, M. *Nature Materials* **2009**, 8, (7), 543-557.
127. Lewis, J. A. *Journal of the American Ceramic Society* **2000**, 83, (10), 2341-2359.
128. Davis, M. E.; Chen, Z.; Shin, D. M. *Nature Reviews Drug Discovery* **2008**, 7, 771-782.
129. Eastman, J. A.; Phillpot, S. R.; Choi, S. U. S.; Keblinski, P. *Annual Review of Materials Research* **2004**, 34, 219-246.
130. Donzelli, G.; Cerbino, R.; Vailati, A. *Physical Review Letters* **2009**, 102, 104503.

131. Choi, S. U. S. *Journal of Heat Transfer* **2009**, 131, 033106.
132. Keblinski, P.; Eastman, J. A.; Cahill, D. G. *Materials Today* **2005**, 8, (6), 36-44.
133. Wang, X.-Q.; Mujumdar, A. S. *International Journal of Thermal Sciences* **2007**, 46, 1-19.
134. Xie, H.; Lee, H.; Youn, W.; Choi, M. *Journal of Applied Physics* **2003**, 94, (8), 4967-4971.
135. Buongiorno, J. *Journal of Heat Transfer* **2006**, 128, 240-250.
136. Moreau, P.; van Effenterre, D.; Navailles, L.; Nallet, F.; Roux, D. *The European Physical Journal E* **2008**, 26, (3), 225-234.
137. Hatch, A.; Kamholz, A.; Hawkins, K.; Munson, M.; Schilling, E.; Weigl, B.; Yager, P. *Nature Biotechnology* **2001**, 19, (5), 461-465.
138. Kasnavia, T.; Vu, D.; Sabatini, D. A. *Ground Water* **1999**, 37, (3), 376-381.
139. Green, F. J., *The Sigma-Aldrich Handbook of Stains, Dyes, and Indicators*. Aldrich Chemical Co.: Milwaukee, WI, 1990.
140. Nishi, N.; Izawa, K.; Yamamoto, M.; Kakiuchi, T. *J Phys Chem B* **2001**, 105, (34), 8162-8169.
141. Ismagilov, R. F.; Stroock, A. D.; Kenis, P. J. A.; Whitesides, G.; Stone, H. A. *Appl Phys Lett* **2000**, 76, (17), 2376-2378.
142. Kamholz, A.; Weigl, B.; Finlayson, B.; Yager, P. *Anal Chem* **1999**, 71, (23), 5340-5347.
143. Kamholz, A.; Yager, P. *Biophysical Journal* **2001**, 80, (1), 155-160.
144. Kamholz, A.; Yager, P. *Sensors and Actuators B: Chemical* **2002**, 82, (1), 117-121.
145. Devasenathipathy, S.; Santiago, J.; Takehara, K. *Anal Chem* **2002**, 74, (15), 3704-3713.
146. Badal, M. Y.; Wong, M.; Chiem, N.; Salimi-Moosavi, H.; Harrison, D. J. *Journal of Chromatography A* **2002**, 947, (2), 277-286.
147. Kirby, B.; Hasselbrink, E. *Electrophoresis* **2004**, 25, (2), 203-213.

148. Ocvirk, G.; Munroe, M.; Tang, T.; Oleschuk, R.; Westra, K.; Harrison, D. *Electrophoresis* **2000**, 21, (1), 107-115.
149. Walsh, P. A.; Egan, V. M.; Walsh, E. J. *Microfluidics and Nanofluidics* **2010**, 8, (6), 837-842.
150. Sato, Y.; Irisawa, G.; Ishizuka, M.; Hishida, K.; Maeda, M. *Measurement Science & Technology* **2003**, 14, (1), 114-121.
151. Larson, R. G., *The Structure and Rheology of Complex Fluids*. Oxford University Press, Inc.: New York, NY, 1999.
152. Fuerstenau, D.; Wakamatsu, T. *Faraday Discuss Chem Soc* **1975**, 59, 157-168.
153. Zhang, R.; Somasundaran, P. *Adv Colloid Interfac* **2006**, 123, 213-229.
154. Somasundaran, P.; Krishnakumar, S. *Colloids and Surfaces A: Physicochemical and Engineering Aspects* **1997**, 123, 491-513.
155. Yeskie, M. A.; Harwell, J. H. *The Journal of Physical Chemistry* **1988**, 92, (8), 2346-2352.
156. Wen, D.; Ding, Y. *International Journal of Heat and Mass Transfer* **2004**, 47, (24), 5181-5188.
157. Prasher, R.; Phelan, P. E.; Bhattacharya, P. *Nano Letters* **2006**, 6, (7), 1529-1534.
158. Özerinç, S.; Kakaç, S.; Yazıcıoğlu, A. G. *Microfluidics and Nanofluidics* **2010**, 8, (2), 145-170.
159. Hong, K.; Hong, T. K.; Yang, H. S. *Applied Physics Letters* **2006**, 88, 031901.
160. Philip, J.; Shima, P.; Raj, B. *Nanotechnology* **2008**, 19, 305706.
161. Sabatini, D.; Austin, T. *Ground Water* **1991**, 29, (3), 341-349.
162. Wasan, D.; Nikolov, A. *Nature* **2003**, 423, (6936), 156-159.
163. Arita, T.; Yoo, J.; Ueda, Y.; Adschiri, T. *Nanoscale* **2010**, 2, (5), 689-693.
164. Baby, T. T.; Ramaprabhu, S. *Nanoscale* **2011**, 3, (5), 2208-2214.
165. Peng, H.; Ding, G. L.; Hu, H. T.; Jiang, W. T.; Zhuang, D. W.; Wang, K. J. *Int J Refrig* **2010**, 33, (2), 347-358.

166. Vadukumpully, S.; Gupta, J.; Zhang, Y.; Xu, G. Q.; Valiyaveetil, S. *Nanoscale* **2011**, 3, (1), 303-308.
167. Rosell, A.; Storti, G.; Morbidelli, M.; Bratton, D.; Howdle, S. M. *Macromolecules* **2004**, 37, (8), 2996-3004.
168. Doan, V.; Koppe, R.; Kasai, P. H. *J Am Chem Soc* **1997**, 119, (41), 9810-9815.
169. Yang, Y. Fluorous membrane-based separations and reactions. Ph.D., University of Pittsburgh, Pittsburgh, PA, 2011.
170. Moore, V. C.; Strano, M. S.; Haroz, E. H.; Hauge, R. H.; Smalley, R. E.; Schmidt, J.; Talmon, Y. *Nano Letters* **2003**, 3, (10), 1379-1382.
171. Balandin, A. A.; Ghosh, S.; Bao, W. Z.; Calizo, I.; Teweldebrhan, D.; Miao, F.; Lau, C. N. *Nano Letters* **2008**, 8, (3), 902-907.
172. Yu, W.; Xie, H. Q.; Bao, D. *Nanotechnology* **2010**, 21, (5).
173. Xie, H. Q.; Lee, H.; Youn, W.; Choi, M. *J Appl Phys* **2003**, 94, (8), 4967-4971.
174. Che, J.; Cagin, T.; Goddard III, W. A. *Nanotechnology* **2000**, 11, (2), 65-69.
175. Huxtable, S. T.; Cahill, D. G.; Shenogin, S.; Xue, L.; Ozisik, R.; Barone, P.; Usrey, M.; Strano, M. S.; Siddons, G.; Shim, M. *Nature Materials* **2003**, 2, (11), 731-734.
176. Turgut, A.; Tavman, I.; Chirtoc, M.; Schuchmann, H. P.; Sauter, C.; Tavman, S. *Int J Thermophys* **2009**, 30, (4), 1213-1226.
177. Wang, Z. L.; Tang, D. W.; Liu, S.; Zheng, X. H.; Araki, N. *Int J Thermophys* **2007**, 28, (4), 1255-1268.
178. Zhang, X.; Gu, H.; Fujii, M. *Int J Thermophys* **2006**, 27, (2), 569-580.
179. Garg, P.; Alvarado, J.; Marsh, C.; Carlson, T.; Kessler, D.; Annamalai, K. *International Journal of Heat and Mass Transfer* **2009**, 52, (21-22), 5090-5101.
180. Starr, F. W.; Douglas, J. F.; Glotzer, S. C. *The Journal of Chemical Physics* **2003**, 119, 1777-1788.
181. Hu, P.; Shan, W. L.; Yu, F.; Chen, Z. S. *International Journal of Thermophysics* **2008**, 29, (6), 1968-1973.
182. Maiga, S. E. B.; Nguyen, C. T.; Galanis, N.; Roy, G. *Superlattices and Microstructures* **2004**, 35, (3), 543-557.

183. Xie, H. Q.; Wang, J. C.; Xi, T. G.; Liu, Y.; Ai, F.; Wu, Q. R. *Journal of Applied Physics* **2002**, 91, (7), 4568-4572.
184. Murshed, S. M. S.; Leong, K. C.; Yang, C. *2006 IEEE Conference on Emerging Technologies - Nanoelectronics* **2006**, 155-158.
185. Duangthongsuk, W.; Wongwises, S. *Exp Therm Fluid Sci* **2009**, 33, (4), 706-714.
186. Turgut, A.; Tavman, I.; Chirtoc, M.; Schuchmann, H. P.; Sauter, C.; Tavman, S. *International Journal of Thermophysics* **2009**, 30, (4), 1213-1226.
187. Zhi, C. Y.; Xu, Y. B.; Bando, Y.; Golberg, D. *ACS Nano* **2011**, 5, (8), 6571-6577.
188. Chen, H. S.; Ding, Y. L.; Tan, C. Q. *New J Phys* **2007**, 9.
189. Kole, M.; Dey, T. *Journal of Physics D: Applied Physics* **2010**, 43, 315501.
190. Yu, W.; Xie, H. Q.; Li, Y.; Chen, L. F. *Particuology* **2011**, 9, (2), 187-191.
191. He, Y.; Jin, Y.; Chen, H.; Ding, Y.; Cang, D.; Lu, H. *International Journal of Heat and Mass Transfer* **2007**, 50, (11-12), 2272-2281.
192. Timofeeva, E. V.; Routbort, J. L.; Singh, D. *Journal of Applied Physics* **2009**, 106, (1), 014304.
193. Schmidt, A. J.; Chiesa, M.; Torchinsky, D. H.; Johnson, J. A.; Boustani, A.; McKinley, G. H.; Nelson, K. A.; Chen, G. *Appl Phys Lett* **2008**, 92, (24), 244107.
194. Moosavi, M.; Goharshadi, E. K.; Youssefi, A. *Int J Heat Fluid Fl* **2010**, 31, (4), 599-605.
195. Namburu, P. K.; Kulkarni, D. P.; Misra, D.; Das, D. K. *Exp Therm Fluid Sci* **2007**, 32, (2), 397-402.
196. Hu, Y.; Dai, J. *Miner Eng* **2003**, 16, (11), 1167-1172.
197. Anoop, K.; Kabelac, S.; Sundararajan, T.; Das, S. K. *Journal of Applied Physics* **2009**, 106, (3), 034909-034909-7.
198. Gopal, T.; Talbot, J. B. *J Electrochem Soc* **2006**, 153, (7), G622-G625.
199. Sakagami, K.; Yoshimura, T.; Esumi, K. *Langmuir* **2002**, 18, (16), 6049-6053.

200. Chandar, P.; Somasundaran, P.; Turro, N. J. *J Colloid Interf Sci* **1987**, 117, (1), 31-46.
201. Grzadka, E. *Mater Chem Phys* **2011**, 126, (3), 488-493.
202. Singh, B. P.; Menchavez, R.; Takai, C.; Fuji, M.; Takahashi, M. *J Colloid Interf Sci* **2005**, 291, (1), 181-186.
203. Rubio-Hernandez, F. J.; Ayucar-Rubio, M. F.; Velazquez-Navarro, J. F.; Galindo-Rosales, F. J. *J Colloid Interf Sci* **2006**, 298, (2), 967-972.
204. Wang, D.; Xiang, J.; Jiang, H.; Xu, G.; Gong, Q. *Journal of Optics A: Pure and Applied Optics* **2003**, 5, 123-127.

APPENDIX A

Investigation of Nanoparticle Adsorption PDMS Using a X-ray Photoelectron Spectrometer

The trace of the nanoparticle adsorption on PDMS was also searched using the X-ray Photo Electron Spectroscopy (XPS). The PDMS samples prepared according to the recipe in Experimental Methods (Section 3) were first immersed into the solutions containing 1 vol% Al₂O₃ given in the Table 1 and then in deionized water for an hour. After drying in the oven at room temperature, under vacuum, the samples were subjected to XPS measurements in order to detect any change in surface composition. XPS is a quantitative spectroscopic technique for the elemental surface detection of variations in chemical composition and oxidation state.

XPS measurements were performed using Kratos Analytical Axis His 165 Ultra Imaging X Ray Photoelectron Spectrometer equipped with a 165 mm hemispherical electron energy analyzer at high vacuum (10^{-8} to 10^{-9} Torr) using monochromatic Al K α line (1486.7 eV). The analysis area was 300×400 μm at an angle of 90° relative to the substrate surface. The results are given in Table A-1. Here, atomic concentration can be defined as a percentage of the total atomic concentration of all the regions. The atomic concentration is calculated by dividing the Raw Area (this is the area of the peak) by the RSF (the relative sensitivity factor -the sensitivity of the region for each element).

Atomic percentage values normalized to 100% refer to the concentration of each element present in the thin information layer (<10 nm).

Table A-1. The atomic concentration results obtained from XPS measurements.

Solution Composition	Atomic Concentration (%)				
	O	C	S	Si	Al
H ₂ O	31.85	50.46	-	17.69	-
1 vol% Al ₂ O ₃	31.40	50.57	-	14.63	3.4
SDS	31.68	50.98	0.69	16.65	-
TW80	35.32	46.69	-	17.99	-
1 vol% Al ₂ O ₃ + SDS	33.0	51.52	-	14.63	0.85
1 vol% Al ₂ O ₃ + TW80	29.97	53.50	-	15.79	0.73

The elemental analysis displays that there is a tiny amount of alumina present in the sample surface immersed in 1 vol% Al₂O₃. The addition of surfactant substantially decreases the atomic concentration of Al on the PDMS surface which is in the range of instrumental error. It can be concluded that Al presence on the surface does not affect the results of diffusion measurements taken in the microchannel.

APPENDIX B

First it is useful to review relevant results from literature. Alumina has an amphoteric pH dependent surface charge. When alumina nanoparticles are suspended in water, electric charges develop on the particle surface due to the initial hydration of broken aluminum-oxygen bonds and later the dissociation of the hydroxide. The potential-determining ions are hydrogen and hydroxyl ions in this system.¹⁵² Table B-1 displays some of the early zeta potential measurements of alumina particle suspensions. Note that the reported values are dependent on the surfactant and ion concentration present in the system.^{196, 197}

The suspensions were diluted to the desired volume concentrations in deionized water by mixing and ultrasonication as described in Experimental Methods. The solutions were then re-ultrasonicated for 20 min prior to zeta-potential measurements to break up any remaining agglomerates. Since the zeta potential strongly depends on pH and ionic strength, we first measured pH values of (1) the aqueous dye solutions, (2) the alumina suspensions (with and without stabilizing surfactant), and (3) the mixtures containing nanoparticles, dye, and surfactant (Table B-2). DLS particle size measurements were also acquired for each freshly prepared solution.

Table B-1. Summary of previous zeta potential measurements in aqueous alumina suspensions.

pH	Loading/particle size (nm)	Zeta Potential (mV)	Dispersant	Salt or Ionic Compound	Key Observations	Ref.
3 – 10	- / 120	-50 to -30	SDS	0.001 M KNO ₃	Due to adsorption of anionic SDS onto alumina, negative Zeta potential was measured and remained fairly stable (-7mV)	198
2 – 11	0.02 wt% / < 1000	-40 to 40	SDS Dodecylamine chloride (DDA)	0.001 M KCl	SDS addition made zeta potential positive to negative and DDA has almost no effect on the zeta potential of alumina at pH < 9	196
5.2	10 mg/ml / 2500	-30 to 30	SDS PVcA (Poly(1-vinylpyrrolidone-co-acrylic acid))	-	The positive zeta potentials decreased to zero and reached some negative zeta potentials with the SDS concentration	199
6.5	5 g / 300	-70 to 40	SDS	0.1 M NaCl	The decrease in Zeta potential of alumina as a function of SDS concentration. When SDS concentration is higher than 0.001 M, complete surface coverage	200
3 – 11	0.05 g / 72	-80 to 40	TX-100 SDS	0.001 M NaCl	Carboxymethylcellulose-alumina system Presence of surfactants decreases zeta potential and shift pHiep from 7.6 to 6 or 5	201
2 – 12	0.01 wt% / 600	-50 to 50	Anionic Ammonium polycarboxylate	-	Presence of surfactants decreases zeta potential and shift pHiep from 9.1 to 6.3 and 3.4	202
4 – 11	- / 100	-30 to 60	-	-	pHiep is basic for alumina (~ 9.1)	203

(pH_{iep} indicates the pH value where surface concentration of H⁺ and OH⁻ are equal)

The pHs of the aqueous dye solutions are clustered within the same range (4.8 – 5.5), and the particle/surfactant suspensions are also grouped together (7.3 – 7.7). These formulations represent the initial and final states of the suspensions (i.e., before adding the dye to the nanoparticle suspensions). After adding dye, the suspension pH is not appreciably changed, remaining in the 7 – 8 range. A slight increase is evident with rhodamine 6G, as opposed to Rose Bengal whose pH remains close to the nanoparticle-surfactant case. In this system at least, conventional bulk experiments provide only limited definitive insights about the underlying phenomena in the context of the envisioned application scenarios.

Table B-2. Measured pH of aqueous dye solutions and suspensions.

Solution Composition (concentrations in units of mg/ml)	Measured pH						Mean	Std. Dev.
	1	2	3	4	5	6		
Rh 6G (0.1)	4.77	4.75	5.08	4.73	4.74	4.78	4.81	0.13
Rh 6G (0.5)	5.00	5.09	5.12	5.18	5.13	5.14	5.11	0.06
Rose Bengal (5)	5.51	5.50	5.58	5.49	5.53	5.55	5.53	0.03
Al₂O₃	4.89	4.60	5.08	4.71	4.78	4.74	4.80	0.17
Al₂O₃-SDS (15)	7.19	7.35	7.56	7.08	6.99	7.44	7.27	0.22
Al₂O₃-SDS (120)	7.71	7.83	7.37	7.80	7.45	7.79	7.66	0.20
Al₂O₃-SDS (15) -Rh 6G (0.1)	8.17	7.78	8.12	7.74	8.17	7.77	7.96	0.21
Al₂O₃-SDS (15) -Rh 6G (0.5)	7.56	8.08	8.18	7.53	8.08	8.21	7.94	0.31
Al₂O₃-SDS (15)-Rose Bengal (5)	7.39	7.26	7.30	7.31	7.12	7.14	7.25	0.10

All suspensions contain Al₂O₃ nanoparticles at 0.25 vol% solution. Rhodamine 6G and Rose Bengal concentrations were 0.1, 0.5 and 5 mg/ml, respectively. The SDS concentration was 15 and 120 mg/ml. These concentrations are specified in parentheses beside each compound.

A new series of DLS measurements were performed to cover a broader compositional range and ensure consistent results. These data (Table B-3) suggest a slight but perceptible increase in particle size upon addition of rhodamine 6G, echoing the general trends identified in the pH and zeta potential measurements that point to an increased tendency toward aggregate formation with rhodamine 6G than with Rose Bengal. This expanded dataset is now incorporated. From a practical standpoint, the challenges we encountered to overcome the learning curve associated with both the DLS and zeta potential measurements actually make a compelling case in favor of the simplicity of the microfluidic method to obtain a similar characterization of the fluid. It is also noted that the dilution required by this method inherently excludes direct analysis of our suspensions at the same concentrations employed in our other experiments.

Table B-3. Particle sizes obtained using DLS.

Solution Composition (concentrations in units of mg/ml)	Particle Size (nm)						Mean	Std. Dev.
	1	2	3	4	5	6		
Al₂O₃	176.3	160.6	183	171.4	148.8	141.5	163.60	16.22
Al₂O₃-SDS (15)	162.2	150.7	165.8	157.4	169.9	160.1	161.02	6.69
Al₂O₃-SDS (120)	193	152	149.9	172.9	155.3	149.7	162.13	17.45
Al₂O₃-SDS (15) -Rh 6G (0.1)	181.8	172.4	200.3	168.4	174.1	160.8	176.30	13.63
Al₂O₃-SDS (15) -Rh 6G (0.5)	184.1	157.9	169	170.7	168.7	184.5	172.48	10.21
Al₂O₃-SDS (15)-Rose Bengal (5)	168.4	153.9	148.1	176.9	168.1	152.7	161.35	11.34

All suspensions contain Al₂O₃ nanoparticles at 0.02 vol% solution. At this dilution, rhodamine 6G and Rose Bengal concentrations were ~ 0.0087, 0.043 and 0.43 mg/ml, respectively. The SDS concentrations were ~1.3 and 10.4 mg/ml, respectively at the 15 and 120 mg/ml bulk conditions specified in parentheses beside each compound.

Zeta potential measurements were performed using a Brookhaven ZetaPALS instrument. The measured values of a standard 10 wt% colloidal silica suspension (Ludox TM-50; Cat. No. 420778, Sigma Aldrich) were in good agreement with literature (Table B-4).¹¹¹ The zeta potential measurements in 0.25 vol% nanoparticle suspensions were next performed (Table B-5).

Table B-4. Two independent series of zeta potential measurements performed in a standard 10 wt% Ludox TM-50 colloidal silica suspension in 0.01 M KCl.

Measurement series	Zeta Potential (mV)										Mean	Std. Dev.
	1	2	3	4	5	6	7	8	9	10		
1	-52.31	-51.68	-47.17	-54.43	-47.68	-48.99	-49.85	-50.20	-45.21	-49.49	-49.70	2.68
2	-51.93	-54.76	-46.27	-52.78	-51.74	-50.60	-55.88	-51.70	-50.57	-51.69	-51.79	2.58

Average pH of suspensions was 9.30.

Table B-5. Zeta potential measurements of the nanoparticle suspensions.

Suspension Composition	Zeta Potential (mV)										Mean	Std. Dev.
	1	2	3	4	5	6	7	8	9	10		
Al₂O₃	45.6	51.13	44.82	46.5	46.88	52.33	48.41	47.75	40.11	50.55	47.41	3.55
Al₂O₃-SDS (15)	-43.66	-44.92	-40	-46.78	-47.75	-51.10	-48.76	-42.95	-44.37	-39.49	-44.98	3.71
Al₂O₃-SDS (120)	-49.78	-46.28	-51.73	-38.04	-41.97	-56.65	-50.51	-47.68	-42.55	-63.58	-48.88	7.47
Al₂O₃-SDS (15)-Rh 6G (0.1)	-19.20	-17.19	-15.76	-18.77	-20.50	-18.21	-13.98	-15.97	-20.02	-17.19	-17.68	2.05
Al₂O₃-SDS (15)-Rh 6G (0.5)	-15.71	-13.72	-19.22	-11.80	-18.34	-10.01	-10.03	-12.70	-15.60	-16.22	-14.34	3.23
Al₂O₃-SDS (15)-Rose Bengal (5)	-42.78	-39.26	-40.21	-42.48	-47.80	-37.24	-44.31	-35.1	-37.37	-33.47	-40.00	4.41

All suspensions contain 0.25 vol% Al₂O₃ nanoparticles. Rhodamine 6G and Rose Bengal concentrations were 0.1, 0.5 and 5 mg/ml, respectively. The SDS concentration was 15 and 120 mg/ml. These concentrations are specified in parentheses beside each compound.

APPENDIX C

Our nanomaterials were also characterized by Transmission Electron Microscopy (TEM). Table C-1 presents the TEM images and diffraction patterns (DP) of each nanomaterial with corresponding crystal structure. The morphology and particle size range of the nanomaterials were also given. These micrographs reveal that nanoparticles are highly agglomerated in dry form. The thickness or diameter of graphene nanosheets (GNS) could not be measured from these 2-D images. The size of the smallest graphene seen in the image of (GNS-2) is only included. Another graphene (GNS-1) cannot be measured since even at the smallest magnification they cover the entire CCD. We only analyzed one multi wall carbon nanotube (CNT-1) and one graphene nanosheet's (GNS-1) DPs since they are supposed to be the same.

Table C-1. TEM images and diffraction patterns (DP) of used nanomaterials.

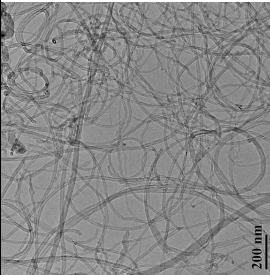
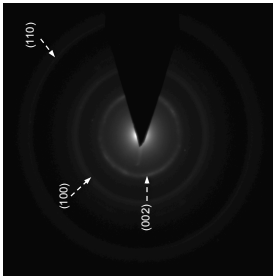
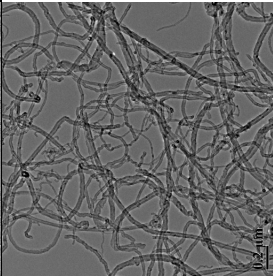
Transmission Electron Microscopy (TEM) Image	Nanomaterial	Diffraction Patterns	Particle Size Range (nm)	Morphology	Crystal Structure
	MWCNT-1 (Cheap Tubes, Inc.)		10-40	Long tubes (~ μm)	Graphitic
	MWCNT-2 (Helix Material Solutions, Inc.)		20-100	Long tubes (~ μm) with some impurities	Graphitic

Table C-1 Continued

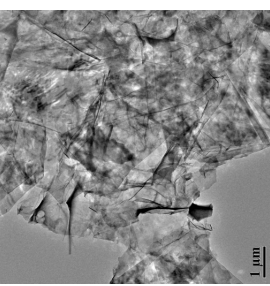
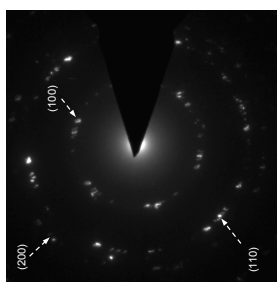
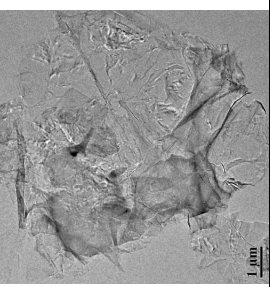
Transmission Electron Microscopy (TEM) Image	Nanomaterial	Diffraction Patterns	Particle Size Range (nm)	Morphology	Crystal Structure
	<p>GNS-1 (Cheap Tubes, Inc.)</p>		-	Nanoplate	Graphitic
	<p>GNS-2 (Skyspring Nanomaterials, Inc.)</p>		8x8 μm	Nanoplate	Graphitic

Table C-1 Continued

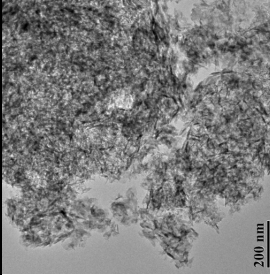
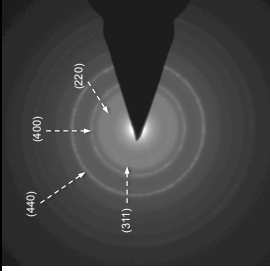
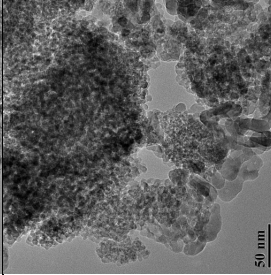
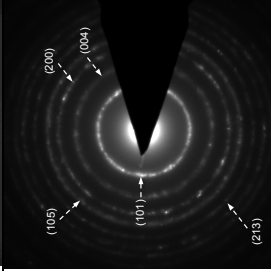
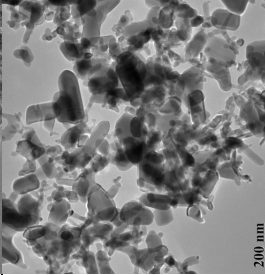
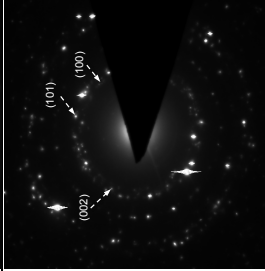
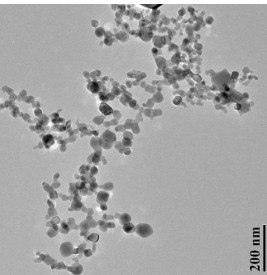
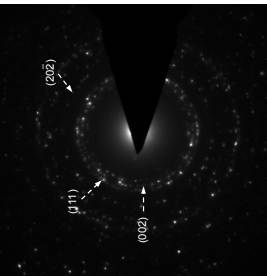
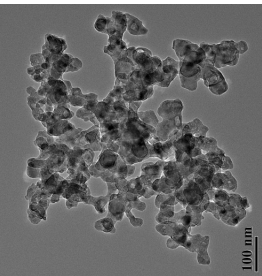
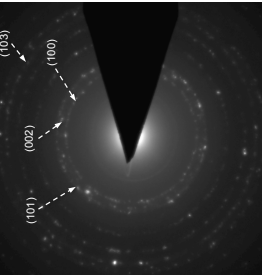
Transmission Electron Microscopy (TEM) Image	Nanomaterial	Diffraction Patterns	Particle Size Range (nm)	Morphology	Crystal Structure
	Al_2O_3		5-50	Disk-shaped	Gamma
	TiO_2		5-25	Spherical	Anatase
	ZnO		50-200	Rod-like shape	Wurtzite

Table C-1 Continued

Transmission Electron Microscopy (TEM) Image	Nanomaterial	Diffraction Patterns	Particle Size Range (nm)	Morphology	Crystal Structure
	CuO		25-50	Spherical and irregular shape, merged particles	Monoclinic (more structure seen)
	AlN		50-100	Spherical and irregular shape with holes	Wurtzite

APPENDIX D

Table D-1. Particle sizes obtained using DLS.

Suspension Composition	Particle Size (nm)						Mean	Std. Dev.
	1	2	3	4	5	6		
Al₂O₃	420.6	413.2	392.6	386.7	389.0	340.6	390.45	28.04
ZnO	202.0	199.7	223.8	207.9	211.5	228.9	212.30	11.77
AlN	270.4	273.7	315.2	291.1	274.0	263.2	281.27	18.99
CuO	130.3	148.8	145.8	137.1	145.6	153.2	143.47	8.33
TiO₂	88.0	56.7	71.2	101.0	74.8	74.8	77.75	15.16

All suspensions contain nanoparticles at 0.02 vol% solution except CuO and TiO₂ (0.004 vol%). The K157 concentration was 0.09 vol%.

Table D-2. Zeta potential measurements of the nanoparticle suspensions.

Suspension Composition	Zeta Potential (mV)										Mean	Std. Dev.
	1	2	3	4	5	6	7	8	9	10		
Al ₂ O ₃	-35.48	-37.94	-33.3	-38.37	-34.11	-34.26	-34.4	-36.36	-36.13	-36.55	-35.69	1.78
	-35.61	-36.24	-37.97	-37.43	-37.63	-34.29	-33.39	-34.55	-33.94	-37.94		
	-34.54	-34.73	-34.77	-38.46	-33.25	-33.79	-33.66	-39.17	-36.23	-36.16		
ZnO	-53.64	-56.95	-54.65	-57.18	-52.32	-54.45	-52.35	-53.76	-54.69	-52.12	-54.37	2.04
	-56.3	-52.36	-52.35	-56.51	-56.7	-52.45	-51.9	-54.8	-55.64	-52.26		
	-57.35	-54.56	-55.07	-56.79	-52.45	-58.91	-53.3	-55.31	-51.98	-51.93		
AlN	-41.31	-42.41	-44.03	-43.81	-41.23	-42.11	-44.64	-43.58	-41.11	-41.23	-42.72	1.43
	-43.03	-41.84	-43.57	-40.84	-40.94	-43.85	-41.38	-42.14	-41.25	-41.91		
	-43.87	-44.59	-43.11	-41.32	-41.91	-42.55	-42.72	-46.45	-44.49	-44.51		
CuO	-46.27	-42.13	-40.74	-44.51	-49.2	-39.53	-42.14	-45.13	-39.36	-53.43	-43.22	4.51
	-41.38	-41.56	-43.59	-37.89	-43.65	-50.12	-46.73	-36.24	-40.1	-50.09		
	-43.98	-37.85	-43.5	-37.82	-51.26	-41.44	-41.95	-39.58	-37.34	-47.96		
TiO ₂	-31.89	-37.85	-39.38	-34.12	-38.24	-39.18	-32.52	-39.92	-42.31	-36.42	-36.63	3.44
	-34.61	-36.28	-38.48	-35.73	-38.62	-35.57	-30.67	-35.04	-36.72	-33.31		
	-35.69	-42.96	-44.5	-31.75	-40.91	-37.22	-31.82	-36.21	-34.64	-36.32		

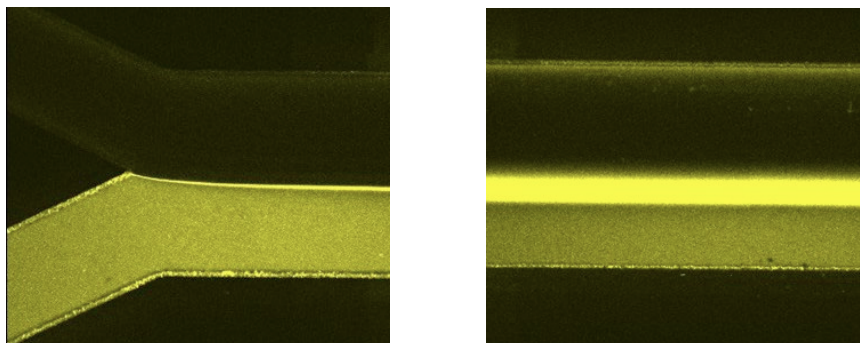
All suspensions contain nanoparticles at 0.02 vol% solution except CuO and TiO₂ (0.004 vol%). The KI57 concentration was 0.09 vol%. SDS concentration was 15 and 120 mg/ml. These concentrations are specified in parentheses beside each compound.

APPENDIX E

Selectivity to Nanoparticle Composition (TiO₂ Nanoparticles in The Microchannel)

The selectivity for nanoparticle suspensions is possible due to the inherent nature of the dye-nanoparticle complexation interactions, which can result in either fluorescence enhancement or quenching. This is illustrated by comparing the fluorescence behavior observed in Al₂O₃ and TiO₂ nanoparticle suspensions. In the case of Al₂O₃, the complexation interactions produce fluorescence enhancement at the interface with the dye stream (Figure E-1a). But, much different behavior is observed in the case of TiO₂, where a strong quenching of interfacial fluorescence occurs (Figure E-1b). This behavior arises as a consequence of electron transfer interactions between the excited adsorbed dye and the nanoparticle's conduction band.²⁰⁴ The size of this energy gap in the case of TiO₂ is such that this transfer results in fluorescence quenching. This behavior is exciting because it introduces the possibility to achieve selectivity with respect to the nanoparticle species (e.g., to distinguish nanoparticles with different compositional characteristics).

a.



b.

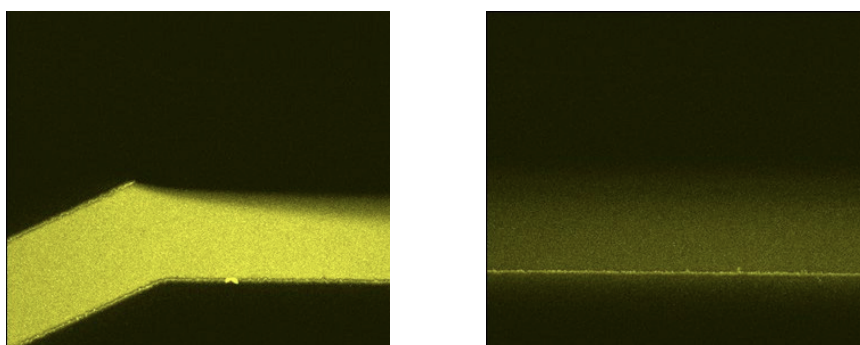
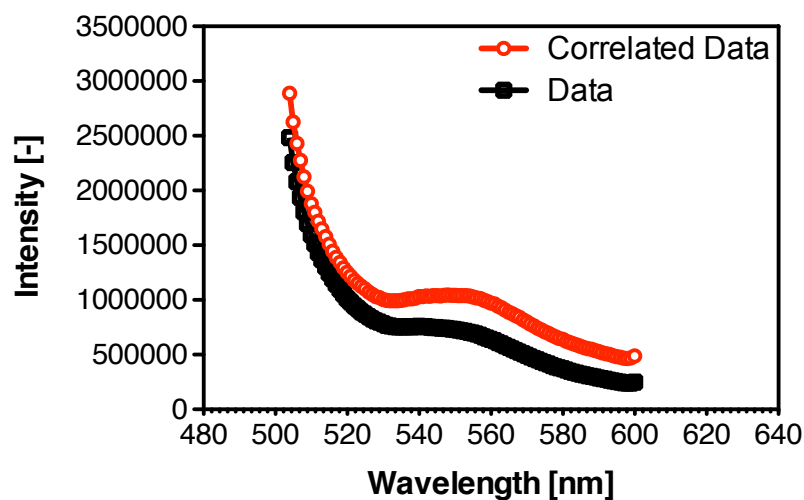


Figure E-1. Compositional selectivity based on interfacial fluorescence (images shown at inlet and 24 mm downstream). (a) Al₂O₃ nano-particles (upper stream) exhibit intense interfacial fluorescence upon complexation with fluorescein (lower stream). (b) The opposite effect occurs with TiO₂ nanoparticles (upper stream), resulting in fluorescence quenching.

Investigation of Dye-Nanoparticle Interaction Using a Spectrofluorometer

The influence of composition on the fluorescence characteristics associated with the dye-nanoparticle complex suggests that probing spectral features of the emitted fluorescence can provide a more detailed picture than the intensity alone. This hypothesis was tested by examining the emission spectra of mixtures containing various dye-nanoparticle-surfactant combinations (Figure E-2). Steady-state fluorescence spectra of dye laden nanoparticle suspensions were recorded with PTI (Photon Technology International, Inc., Lawrenceville, NJ, USA) QuantaMaster series Spectrofluorometer equipped with a 75 W Xenon arc lamp. All measurements were carried out in 1 cm path length disposable cuvettes (VWR) at room temperature under ambient conditions. PTI Fluorescence Master System Felix32 software was used for fluorescence data collection and analysis over a wavelength range of 500-600 nm. The slit widths were adjusted to 1, 2 and 5 nm in order to maintain robust measurements. These data show clear differences between spectra of solutions containing only nanoparticles and a mixture of dye and nanoparticles. Moreover, the Al₂O₃ and TiO₂ spectra are noticeably different suggesting that the spectral characteristics of the interfacial fluorescence signal can provide a method to obtain a “fingerprint” of the nanoparticle suspension’s chemical composition (Figure E-2).

a.



b.

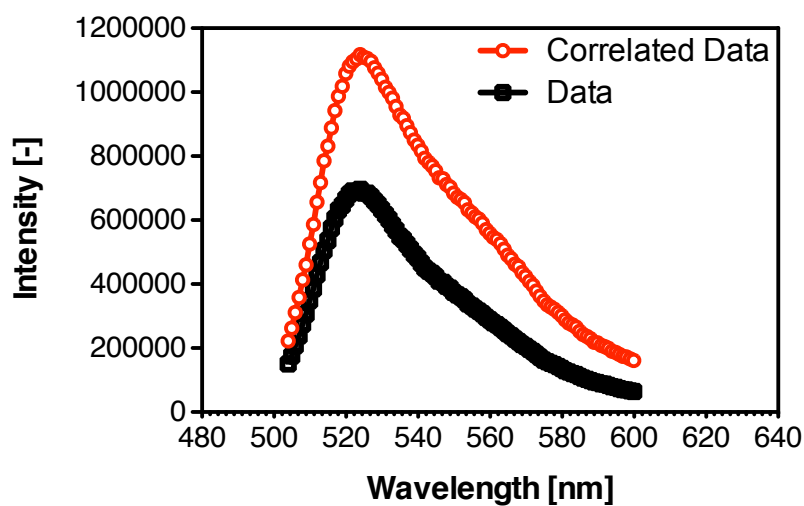
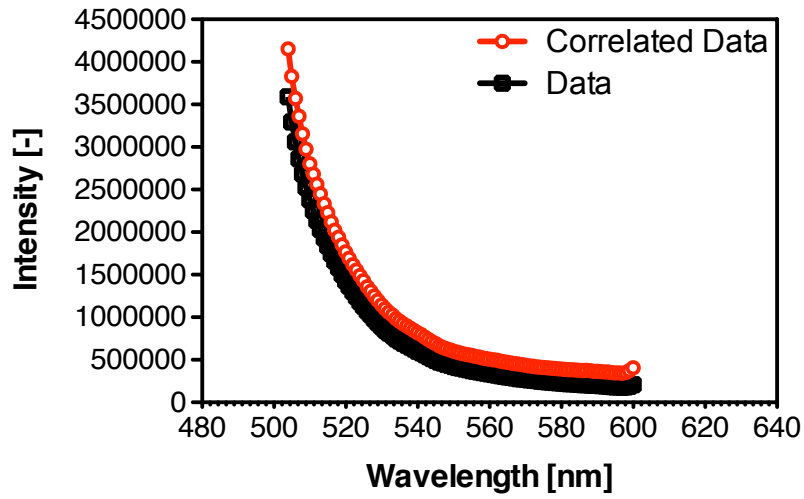


Figure E-2. Fluorometer data characterizing spectral response upon excitation at 490 nm with and without addition of fluorescein dye. (a-b) Al₂O₃ nanoparticles, (c-d) TiO₂ nanoparticles. The spectral response characteristics are noticeably different for each material, indicating the potential for compositional selectivity based on dye-nanoparticle complexation.

c.



d.

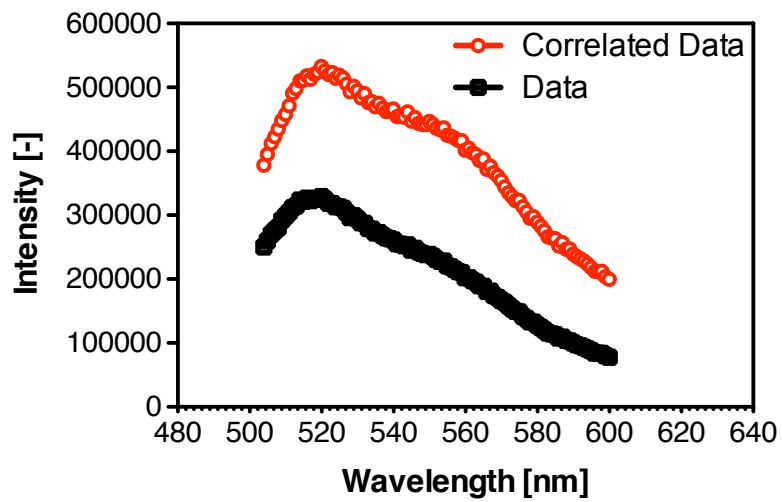


Figure E-2 Continued.

APPENDIX F

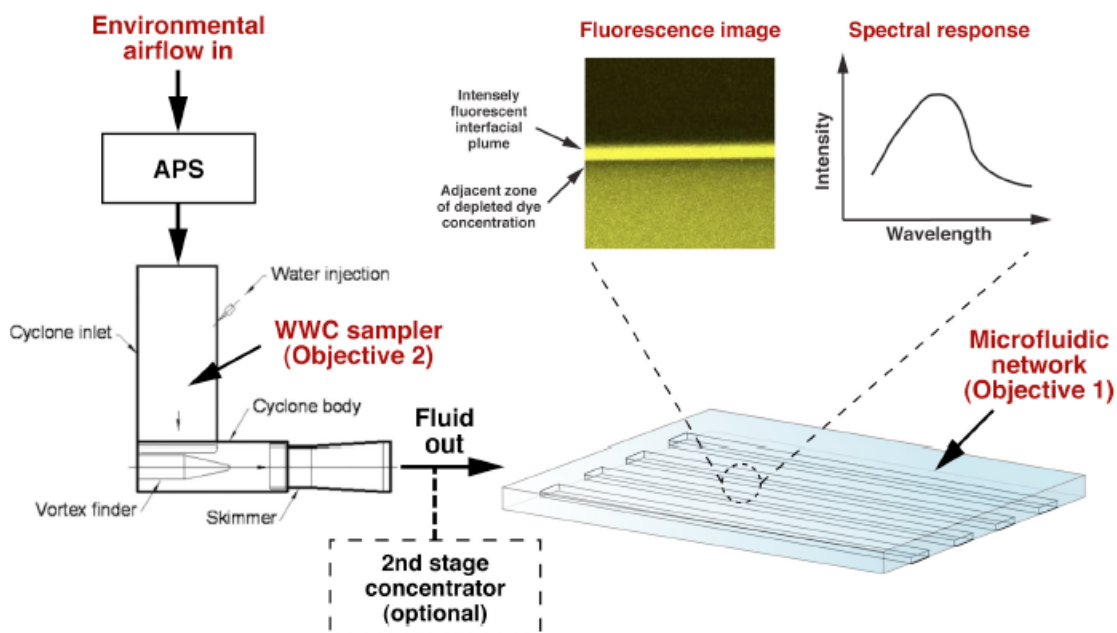


Figure F-1. Illustration of proposed environmental nanoparticle collection/detection approach. Nanoparticles are collected and characterized using an aerodynamic particle sizer (APS) after which they are collected and concentrated using a wetted wall cyclone (WWC) sampler. The concentrated nanoparticle laden fluid extracted from the WWC can be further concentrated (optional step), then fed into a microfluidic network in parallel with a trace dye so that interfacial fluorescence enhancement/ quenching can be monitored (both directly for instantaneous detection, and via emission spectra for characterization and identification). The system is capable of sampling hundreds of liters of air per min, making it possible to quickly analyze the entire air volume of a workspace.